$N \rightarrow \Delta$ transition and proton polarizabilities from measurements of $p(\vec{\gamma},\gamma)$, $p(\vec{\gamma},\pi^0)$, and $p(\vec{\gamma},\pi^+)$

G. Blanpied,[4] M. Blecher,[6] A. Caracappa,[1] R. Deininger,[7] C. Djalali,[4] G. Giordano,[2] K. Hicks,[7] S. Hoblit,[1,5] M. Khandaker,[6,1] O. C. Kistner,[1] A. Kuczewski,[1] F. Lincoln,[1] M. Lowry,[1] M. Lucas,[4] G. Matone,[2,†] L. Miceli,[1,4] B. M. Preedom,[4] D. Rebreyend,[4] A. M. Sandorfi,[1,*] C. Schaerf,[3] R. M. Sealock,[5] H. Ströher,[8] C. E. Thorn,[1] S. T. Thornton,[5] J. Tonnison,[6,1] C. S. Whisnant,[4] H. Zhang,[7] and X. Zhao[6]

(The LEGS Collaboration)

[1]*Physics Department, Brookhaven National Laboratory, Upton, New York 11973*
[2]*INFN-Laboratori Nazionali di Frascati, Frascati, Italy*
[3]*Università di Roma "Tor Vergata" and INFN-Sezione di Roma 2, Rome, Italy*
[4]*Department of Physics, University of South Carolina, Columbia, South Carolina 29208*
[5]*Department of Physics, University of Virginia, Charlottesville, Virginia 22901*
[6]*Physics Department, Virginia Polytechnic Institute & State University, Blacksburg, Virginia 24061*
[7]*Department of Physics, Ohio University, Athens, Ohio 45701*
[8]*Forschungszeutrum Jülich, Jülich, Germany*

(Received 5 July 2000; published 27 July 2001)

We report new high-precision measurements of $p(\vec{\gamma},\gamma)$, $p(\vec{\gamma},\pi^0)$ and $p(\vec{\gamma},\pi^+)$ cross section and beam asymmetry angular distributions for photon beam energies in the range from 213 MeV to 333 MeV. The cross sections for all three channels are locked together with a small common systematic scale uncertainty of 2%. A large overdetermination of kinematic parameters was used to achieve the first complete separation of the Compton scattering and π^0-production channels. This has also allowed all detector efficiencies for the $p(\vec{\gamma},\gamma)$ and $p(\vec{\gamma},\pi^0)$ channels to be measured directly from the data itself without resorting to simulations. The new Compton results are approximately 30% higher than previous Bonn data near the peak of the Δ resonance, resolving a long-standing *unitarity puzzle*. However, our $p(\vec{\gamma},\pi^0)$ and $p(\vec{\gamma},\pi^+)$ cross sections are also about 10% higher than both earlier Bonn data and recent Mainz measurements, while our $p(\vec{\gamma},\pi^+)$ cross sections are in good agreement with results from Tokyo. Our polarization asymmetry data are of the highest precision yet available and have considerable impact upon multipole analyses. These new data have been combined with other polarization ratios in a simultaneous analysis of both Compton scattering and π production, with Compton scattering providing two new constraints on the photopion amplitude. This analysis has improved the accuracy in the $E2/M1$ mixing ratio for the $N \rightarrow \Delta$ transition, $EMR = -[3.07 \pm 0.26(\text{stat+syst}) \pm 0.24(\text{model})](\%)$, and the corresponding $N \rightarrow \Delta$ transverse helicity amplitudes, $A_{1/2} = -[135.7 \pm 1.3(\text{stat+syst}) \pm 3.7(\text{model})](10^{-3}\ \text{GeV}^{-1/2})$ and $A_{3/2} = -[266.9 \pm 1.6(\text{stat+syst}) \pm 7.8(\text{model})](10^{-3}\ \text{GeV}^{-1/2})$. From these we deduce an oblate spectroscopic deformation for the Δ^+. The same simultaneous analysis has been used to extract the proton *dipole polarizabilities*, $\overline{\alpha} - \overline{\beta} = +[10.39 \pm 1.77(\text{stat+syst})^{+1.02}_{-1.87}(\text{model})](10^{-4}\ \text{fm}^3)$ in agreement with previous low energy measurements, and $\overline{\alpha} + \overline{\beta} = +[13.25 \pm 0.86(\text{stat+syst})^{+0.23}_{-0.58}(\text{model})](10^{-4}\ \text{fm}^3)$ in agreement with recent evaluations of the Baldin sum rule. Our simultaneous analysis has also provided the first determination of the proton *spin polarizabilities*, $\gamma_\pi = -[27.23 \pm 2.27(\text{stat+syst})^{+2.24}_{-2.10}(\text{model})](10^{-4}\ \text{fm}^4)$, $\gamma_0 = -[1.55 \pm 0.15(\text{stat+syst})^{+0.03}_{-0.03}(\text{model})](10^{-4}\ \text{fm}^4)$, $\gamma_{13} = +[3.94 \pm 0.53(\text{stat+syst})^{+0.20}_{-0.18}(\text{model})](10^{-4}\ \text{fm}^4)$, and $\gamma_{14} = -[2.20 \pm 0.27(\text{stat+syst})^{+0.05}_{-0.09}(\text{model})](10^{-4}\ \text{fm}^4)$. The extracted value of the *backward spin polarizability*, γ_π, is considerably different from other analyses and this has been instrumental in bringing the value of $\overline{\alpha} - \overline{\beta}$ extracted from high energy data into agreement with low energy experiments.

DOI: 10.1103/PhysRevC.64.025203 PACS number(s): 14.20.Gk, 13.60.Fz, 13.60.Le, 13.88.+e

I. INTRODUCTION

The properties of the proton and the Δ^+, its first excited state and the only well isolated nucleon resonance, serve as a bench mark for models of nucleon structure. The isospin $\tau = 3/2$ Δ decays with an 0.6% γN branch to the nucleon ground state and with a 99.4% branch to πN final states. Elastic (Compton) photon scattering and pion photoproduction in the energy region of the P_{33} $\Delta(1232)$ resonance are both rich sources of structure information.

The proton's first order scattering response is fixed by its static properties of mass, charge, magnetic moment and spin. The leading corrections to this *point* scattering come from the dynamic rearrangement of constituent charges and spins within the proton, and are expressed in terms of six *polarizability* parameters [1,2]. These fundamental properties of the proton can be compared to QCD through, for example, the calculational techniques of chiral perturbation theory (χPT) [3–7]. The two spin-independent *dipole* polarizabilities have been extensively studied and their experimental status has

*Corresponding author. Email address: sandorfi@bnl.gov
†Deceased.

been summarized in [8]. The first extraction of one of the four *spin* polarizabilities has come from an analysis of the present experiment and has been reported in [9]. Here we present the final data and analyses, including an extraction of all six proton polarizabilities.

Although the lifetime of the $\Delta(1232)$ precludes scattering measurements, the $N\rightarrow\Delta$ transition amplitudes carry important structure information. While this transition is dominantly $M1$ quark spin-flip, a small $E2$ component is expected from the interaction with pions (either in a cloud surrounding the proton [10–12], or as $q\bar{q}$ exchange currents between constituent quarks [13]). Since nucleon models differ greatly on the mechanisms used to generate these components, the $E2$ and $M1$ transition amplitudes provide another sensitive testing ground. Of particular interest is the ratio of the $E2$ to $M1$ $N\rightarrow\Delta$ transition strengths (EMR). Hadron models predict this mixing ratio to be quite small with values ranging between -0.5% and -6% [14], so the requirements of experiment are quite demanding. Extractions of the EMR from *pre-1990* experimental data (mostly unpolarized) favored values between -1.1% and -1.6% [15,16]. However, early in the last decade the first of a new class of precision polarization measurements became available from the LEGS facility. These proved to be inconsistent with previous extractions [17], and instead required an increase in the EMR of about a factor of two [18–20]. This factor of two is particularly crucial for models of hadron structure. In its absence there is essentially no room for a pion cloud around the nucleon [11,12]. The database has expanded considerably during the last ten years, chiefly from new experiments at LEGS and Mainz, and the larger EMR value has been borne out in sophisticated analyses [21,22]. Here we present the final LEGS data and analyses, including extraction of the EMR and the individual transverse $N\rightarrow\Delta$ amplitudes.

Compton scattering, pion photoproduction, and pion-nucleon scattering are related by unitarity through a common *S matrix*. Below 2π threshold, $E_\gamma=309$ MeV, Watson's theorem requires the (γ,π) and (π,π) channels to have a common phase [23], and *K-matrix* theory can be used to provide a consistent, albeit model dependent, extension of this unitarity relation to higher energies [16]. Once the (γ,π) multipoles are specified, the imaginary parts of the Compton amplitudes are completely determined by unitarity and a dispersion calculation involving integrals of the pion multipoles can be used to generate their real parts with the only unknowns being the nucleon polarizabilities [24,9].

At any given energy, a minimum of eight independent observables (for each pion charge state) are necessary to specify the photopion amplitude [25]. Such complete information has never been available and previous analyses have relied almost exclusively on only four, the cross section and the three single polarization asymmetries, Σ (linearly polarized beam), T (target), and P (recoil nucleon). In previous experiments, the π^0 and π^+ channels have generally been measured separately, each with independent systematic errors which complicates the situation even further. In such a case, specific multipoles such as the very interesting $\tau=3/2$ $M1$ and $E2$ components can still be extracted from a fit to a multipole expansion of the amplitude. But constraints from many observables are needed to avoid Donnachie's ambiguity of higher partial wave strength appearing in lower partial waves, and vice versa [26]. Compton scattering has the potential for providing both new constraints on the photo-pion multipoles as well as information on the proton polarizabilities. However, the effectiveness of such new constraints requires minimal uncertainties in the relative cross section scales between the (γ,γ), (γ,π^0) and (γ,π^+) channels. This can only be achieved through the measurement of both pion and Compton channels in a single experiment which, prior to this work, has not been available.

A number of measurements of proton Compton scattering have been performed between 1960 and 1976 [27–32], the most systematic of these being the 1976 Bonn experiment [32]. However, several authors of dispersion calculations have pointed out a significant inconsistency between the results of these experiments and (γ,π) data near the peak of the Δ [33–36]. With Bonn π-production as input, the dispersion calculations always overpredicted the Compton cross sections near the Δ peak. A lower *unitarity* bound on the Compton cross sections, which avoids questions regarding convergence of the dispersion integrals, can be constructed by using π production to evaluate the imaginary parts of the Compton amplitudes while setting their real parts to zero [34,33,36]. Beyond this, minimal real parts can be formed from the *s-* and *u-channel* Born and *t-channel* π^0-pole graphs [35]. These exercises lead to a common conclusion. Previously published data near the peak of the Δ resonance, and particularly at 90° center of mass (c.m.), appear to completely exhaust these bounds, if not violate them, and leave no room for the dispersive contributions [37].

The chief experimental background to Compton scattering comes from the $\gamma p\rightarrow\pi^0 p$ channel, where one high energy photon from π^0-decay is detected. The cross section for this process is $\sim$200 times that expected from Compton scattering. The earlier Compton experiments did not have sufficient resolution to unambiguously separate the Compton and (γ,π^0) channels, and relied heavily on simulations to identify regions in which the Compton process should dominate. In contrast, the present experiment was designed to eliminate potential problems with π^0 background subtraction by (a) constructing an observable in which the two competing channels are completely separated, and (b) directly measuring all detector efficiencies, thus eliminating the dependence upon simulations. Both of these goals were achieved in the present experiment with a large over-determination of kinematic parameters.

To minimize uncertainties in multipole determinations, the (γ,π^+) channel was also measured in the same experiment. Although Monte Carlo simulations were used here to correct for π^+ reactions in the material of the detectors, the high resolution of the detectors allowed a sensitive evaluation of these simulations (which several standard hadron reaction packages in fact failed). In the experiment described here, cross sections and linear polarization asymmetries have been determined for the $p(\vec{\gamma},\gamma)$, $p(\vec{\gamma},\pi^0)$, and $p(\vec{\gamma},\pi^+)$ reactions in such a way that the overall cross section scales

for the three channels are locked together with a small systematic scale uncertainty. At energies below the Δ (for E_γ less than about 270 MeV) our results for all three channels are in substantial agreement with the earlier Bonn data [32,38,39]. But near the Δ peak, our measured Compton cross sections are about 28% higher than the 1976 Bonn measurements of [32]. This has resolved the long standing *unitarity puzzle*. However, our π production cross sections are also somewhat higher than the Bonn data at the Δ peak in both the π^0 and π^+ channels. A rescaling of the Bonn data by a factor of 1.10 brings all of their π^0 cross sections and most of their π^+ results in agreement with the cross sections of this work, indicating that the differences actually scale with cross section, not beam energy. Nonetheless, with this rescaling, the Bonn π^+-production at extreme forward and backward angles are noticeably higher than our results. We speculate that these differences are due to $e^\pm$ backgrounds in the Bonn data. Compared with bremsstrahlung sources, laser-backscattering produces a photon beam that is virtually background-free. Assuming this explanation, one concludes that the essential difference between the LEGS and Bonn π-production cross section data is a normalization factor of 10%. This is in fact much larger than can be accommodated by systematic scale uncertainties. Frankly, we found this quite surprising and a great deal of effort has gone into cross-checking our results.

New experiments at Mainz and at Bonn have reported results on Compton scattering and π production. While the Mainz Compton cross sections [40–42] are in quite good agreement with our results, the new π-production cross sections from Mainz [43], and the recent π^+ measurements from Bonn [44], are both close to the old Bonn data. Neither the Mainz work nor the new Bonn experiment measured π^+ production at extreme forward and backward angles, so no information is available on possible backgrounds.

The measurement of Compton, π^0 and π^+ cross sections, with scales that are locked together with a common systematic uncertainty, is a unique feature of this experiment. The key components of the measurement and the analysis are described below. This is covered in some detail because of the differences between our π-production cross sections and those measured at Bonn and Mainz. Beam characteristics are discussed in Sec. II, and experimental geometry in Sec. III. The Compton/π^0 analysis is detailed in Sec. IV, and the π^+ analysis in Sec. V. The final data are presented and compared with other experiments in Sec. VI. We have carried out a multipole analysis of these data and this is described in Sec. VII. The extracted $E2$ and $M1$ $N \rightarrow \Delta$ transition amplitudes are discussed in Sec. VIII, and the proton polarizabilities in Sec. IX. We conclude with a summary of the key points in Sec. X.

II. BEAM CHARACTERISTICS

The experiment was performed at the Laser Electron Gamma Source (LEGS) facility located at the National Synchrotron Light Source (NSLS) of Brookhaven National Laboratory. Linearly polarized γ rays between 213 and 333 MeV were produced by backscattering polarized ultraviolet laser light from 2.58 GeV electrons. The γ-ray energies were determined to $\sim$5.4 MeV, full width at half maximum (FWHM), by detecting the scattered electrons in a tagging spectrometer, as described in [45]. This resolution is dominated by the momentum spread of the electrons in the storage ring. A typical spectrum of tagging electrons is shown in Fig. 1. The backscattered energy is related to the laser and electron energies, ε_l and E_e, by

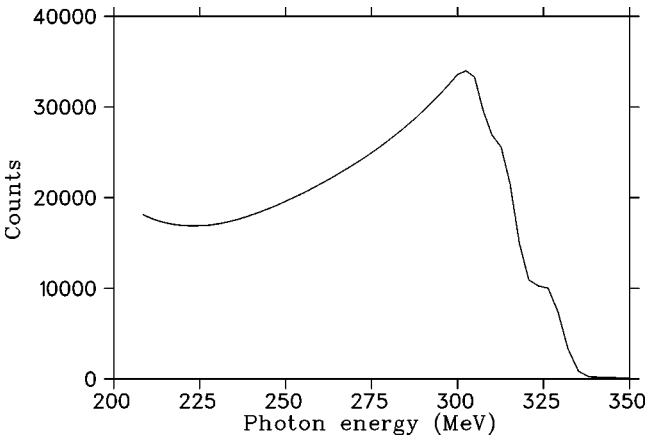

FIG. 1. The spectrum of electrons at the focal plane of the LEGS tagging spectrometer. The horizontal scale gives the corresponding photon energy, $E_\gamma = E_{ring} - E_{tag}$. Three high-energy edges are evident at 307 MeV, 317 MeV, and 332 MeV, corresponding to the backscattering of 364 nm, 351 nm, and 333 nm light from 2.584 GeV electrons, respectively.

$$E_\gamma = \frac{4\varepsilon_l (E_e/m_e)^2}{1 + 4\varepsilon_l E_e/m_e^2 + \theta^2 (E_e/m_e)^2}, \tag{1}$$

where m_e is the electron mass and θ is the laboratory angle between the electron and γ-ray momenta. Maximum γ-ray energies correspond to $\theta = 0°$. Since the laser was operated in a multiline mode (364 nm, 351 nm, 333 nm), this spectrum is actually a superposition of three backscattering spectra with corresponding maximum energies of 307 MeV, 317 MeV, and 332 MeV, respectively. Data for this experiment were collected in three blocks (corresponding to three arrangements of detectors—see Table I below) and the same tagger calibration was maintained throughout. This calibration depends on the value of the electron beam energy. We have verified the storage ring energy by measuring the angle of tagged photons relative to the electron momenta, θ, for different laser lines and different tagger settings. Uncertainties in this measurement lead to a distribution of ring energies with half width $\Delta E_e = \pm 13$ MeV. The corresponding changes in the γ-ray spectrum are quadratic with energy, but in the tagging interval these are approximately given by $\Delta E_\gamma(\text{MeV}) = \pm[0.016 \times E_\gamma(\text{MeV}) - 1.942]$.

The laser-electron backscattering process is simply Compton scattering in the rest frame of the electron, but the Lorentz boost to the laboratory creates a photon *beam* by collapsing the entire angular distribution into a narrow cone about the electron momentum vector. The spatial distribution of the high-energy photon beam after the nuclear target

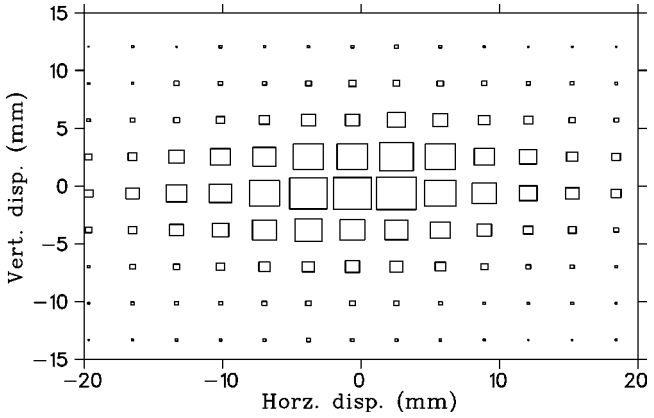

FIG. 2. The measured spatial distribution of the LEGS tagged photon beam. The size of the square symbols is proportional to the intensity.

(~40 m from the center of the interaction region) is shown in Fig. 2. The horizontal ellipse reflects the divergence of the stored electrons which is a factor of five smaller vertically than horizontally. Horizontal and vertical nickel slits, located 20 m upstream of the target and followed by a magnet to sweep $e^{\pm}$ pairs out of the beam, are used to eliminate possible tails and confine the photon beam completely within the target.

Laser backscattering produces substantially higher degrees of polarization than coherent bremsstrahlung. Furthermore, since the production process is simply the Klein-Nishina scattering of light from free electrons in vacuum, the resulting γ-ray polarization can be exactly calculated from the incident laser polarization [46]. Figure 3 shows the calculated energy dependence of the γ-ray linear polarization, $\mathcal{P}(E_\gamma)$, for 100% linearly polarized incident laser light. The result is nearly 100% for the maximum γ-ray energy and never falls below 75% for either state throughout the tagging range (213 to 333 MeV). While there is a slight dependence upon polarization state because of differences in the electron beam divergence in and out of the plane of the storage ring,

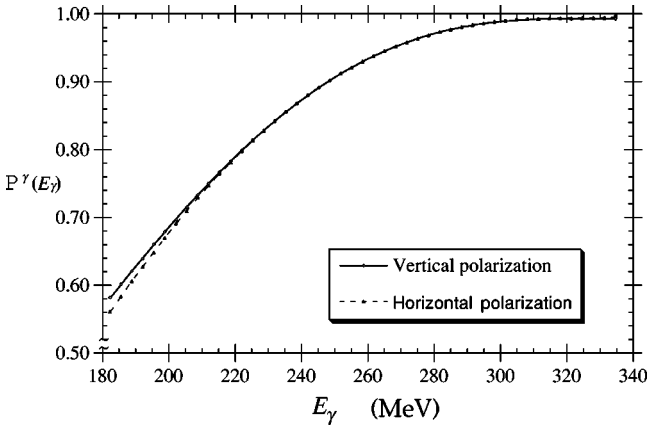

FIG. 3. The energy dependence of the polarization upon γ-ray energy for the two linear polarization states produced in the backscattering of multiline (364 nm, 351 nm, 333 nm) laser light from 2.58 GeV electrons.

above 200 MeV the degree of polarization is virtually identical for both vertical and horizontal orientations of the photon's electric vector.

The actual γ-ray polarization is modified slightly from the curves of Fig. 3 by two effects: bremsstrahlung in the residual gas of the electron-beam vacuum chamber, and partial depolarization of the laser light due to synchrotron radiation damage in the optics used to transport the light into the storage ring. The unpolarized contribution from bremsstrahlung was monitored at random intervals between 150 to 450 s. Within the tagging range it was always a small ($<1\%$) fraction of the flux, F_{brem}, independent of tagging energy. This resulted in an effective correction to the polarization $P_{brem}=(1-F_{brem})$. The laser polarization was measured after the interaction region, at the exit of a 180° port in the bend-magnet upstream of the ring straight section (which is free of synchrotron radiation). The laser light was prepared in two polarization states, horizontal (*state 1,* in the plane of the storage ring) and vertical (*state 2*, perpendicular to the ring plane). Denoting the polarizations of the laser light, as measured after the interaction region, by P_1^l and P_2^l, the corresponding *net* γ-ray polarizations are given by

$$P_1^\gamma(E_\gamma)=P_{brem}\{P_1^l\mathcal{P}_1(E_\gamma)-\tfrac{1}{2}(1-P_1^l)[\mathcal{P}_2(E_\gamma)-\mathcal{P}_1(E_\gamma)]\}, \tag{2a}$$

$$P_2^\gamma(E_\gamma)=P_{brem}\{P_2^l\mathcal{P}_2(E_\gamma)-\tfrac{1}{2}(1-P_2^l)[\mathcal{P}_1(E_\gamma)-\mathcal{P}_2(E_\gamma)]\}. \tag{2b}$$

The second term in Eq. (2) arises from the decomposition of the unpolarized component into its orthogonal components and, since $\mathcal{P}_1\approx\mathcal{P}_2$, this term is very small except at the lower energy end of the tagging interval. The measurements of P_1^l and P_2^l were carried out frequently (67 times during the course of the experiment, split approximately equally between the three data blocks). The standard deviation of measurements within each data block was used to generate the systematic γ-ray polarization uncertainty ($\sim 1\%$) for that block.

During the course of the experiment, the laser polarization was flipped between directions parallel ($\|$) to the reaction plane (*state 1*) and perpendicular ($\perp$) to the reaction plane (*state 2*) at random intervals between 150 to 450 s. Various observables can be constructed from the cross sections measured with the laser polarization in these two states, σ_1 and σ_2. In particular, the cross sections that would be measured by a beam of 100% polarized γ rays with electric vector oriented in, or perpendicular to, the reaction plane ($\sigma_\|$ or $\sigma_\perp$) are given by

$$\sigma_\|=\frac{(1+P_2^\gamma)\sigma_1-(1-P_1^\gamma)\sigma_2}{P_1^\gamma+P_2^\gamma}, \tag{3a}$$

$$\sigma_\perp=\frac{-(1-P_2^\gamma)\sigma_1+(1+P_1^\gamma)\sigma_2}{P_1^\gamma+P_2^\gamma}. \tag{3b}$$

The cross section that would be measured with unpolarized γ rays is just the average of $\sigma_\|$ and $\sigma_\perp$,

$$\sigma = \frac{P_2^\gamma \sigma_1 + P_1^\gamma \sigma_2}{P_1^\gamma + P_2^\gamma}. \tag{3c}$$

The beam asymmetry, $\Sigma = (\sigma_\parallel - \sigma_\perp)/(\sigma_\parallel + \sigma_\perp)$, is

$$\Sigma = \frac{\sigma_1 - \sigma_2}{P_2^\gamma \sigma_1 + P_1^\gamma \sigma_2}, \tag{3d}$$

and the numerator of this quantity, the spin-difference $\hat{\Sigma} = \frac{1}{2}(\sigma_\parallel - \sigma_\perp)$, is related to σ_1 and σ_2 by

$$\hat{\Sigma} = \frac{\sigma_1 - \sigma_2}{P_1^\gamma + P_2^\gamma}. \tag{3e}$$

Since the photon has only two quantum states, any two of $\sigma_\parallel$, $\sigma_\perp$, σ, Σ, and $\hat{\Sigma}$ completely characterize the reaction. The choice of observable usually depends on whether one is trying to suppress or emphasize model dependence when comparing data to a calculation. In all cases, it is important to construct the desired quantities directly from σ_1 and σ_2 in order to avoid the needless amplification of uncertainties.

The calculation of the γ-ray polarization was verified just prior to the start of this experiment by measuring the $D(\vec{\gamma},p)n$ nuclear asymmetry with two different laser lines which produce different photon polarizations at a fixed tag energy [47]. The two data sets are in excellent agreement. The difference between the two asymmetry measurements at each angle, compared with the expected value of zero, gives a χ^2/N_f of 0.84, summed over angles. A second cross check of the beam polarization was provided by the $^4\mathrm{He}(\vec{\gamma},\pi^0)$ asymmetry. Data for the present experiment were collected in three blocks and in between the second and third periods a $^4\mathrm{He}(\vec{\gamma},\pi^0)$ measurement was carried out. Angular momentum and parity conservation require the linear beam polarization asymmetry to be -1 for this reaction, and a comparison of the measured π^0 asymmetry with this expected value yielded a $\chi^2/point$ of 1.39 [48]. As comforting as it is to verify the beam polarization with a nuclear reaction, it is important to keep in mind that such measurements will never approach the accuracy with which the polarization can be calculated from the Klein-Nishina process. Nor is it practical to repeat such nuclear measurements with sufficient frequency to sample their systematic uncertainty. Fortunately, the beam production at LEGS involves only the simplest of processes, and the measurements of the polarization of the light that collided with the free electrons of the storage ring and the small component from bremsstrahlung in the residual gas of the ring vacuum chamber remove the only potential unknowns.

The electron ring at the NSLS operates at a frequency of 52.88 MHz with 25 of a possible 30 Rf *buckets* filled with electrons. LEGS γ rays are thus separated by multiples of 18.9 ns. With an average tagged flux of 4×10^6 s^{-1}, two or more scattered electrons strike the tagging focal-plane detector about 8% of the time. Since a separate time measurement is made for each of the 64 tagger elements relative to a reaction from the target, events associated with multiple tagger hits are easily rejected. Single-hit analyses are used in constructing asymmetry ratios. However, for absolute cross sections, rather than attempting to correct for such a rejection efficiency, multiple tagger hits are treated as accidental coincidences and subtracted by monitoring events associated with the five electron buckets following the *true* event bucket.

At LEGS, the optics of the storage ring guarantee that 100% of the electrons which scatter light to produce γ rays reach the tagging focal plane, provided only that their momentum matches the acceptance setting for the tagger ($p_e < 2.385$ GeV/c, corresponding to $E_\gamma > 207$ MeV for the measurements reported here). This is true even if a scattered electron is out on the tail of the beam divergence distribution and pointed in such a way that the backscattered photon will be stopped in the nickel beam slits. For this reason, we monitor the beam that actually passed through the target, rather than simply counting tagged electrons. The beam flux was monitored by counting e^+e^- pairs in a sampling calorimeter constructed by interspersing scintillators with a thin, copper converter of very uniform thickness. Accidental coincidences with the tagger were subtracted in exactly the same way as in the analysis of the reaction data. The efficiency of this monitor ($\sim$6% with a small energy-dependent slope) was determined by decreasing the flux and comparing with tagged rates measured in a large *monitoring* NaI(Tl) crystal placed directly in the beam. This procedure was tested with counting rates in the NaI ranging from 0.1 kHz to 100 kHz and showed no discernible rate dependence. (The deduced fluxes agreed with the number of tagged electrons within $\sim$5%, and proved to be more stable over long time periods, being independent of the electron orbit in the storage ring.) The efficiency of the sampling calorimeter was measured frequently (54 times throughout the course of the experiment, split approximately equally between the three data blocks). The standard deviation of measurements within each data block was taken as the systematic uncertainty in the flux normalization for that block. This systematic flux normalization uncertainty proved to be nearly constant at $\sim$1%. [Approximately half of this variation could be accounted for by changes in the barometric pressure of the air between the sampling calorimeter and the *monitoring* NaI(Tl) crystal, although no attempt was made to correct for this effect.]

III. EXPERIMENTAL GEOMETRY

In this experiment, the polarized γ-ray beam traversed a cylindrical 13.0 cm long cell of liquid H_2, 6.4 cm in diameter with rounded end-caps. The target walls were made from 0.25 mm thick Mylar, thinned to 0.12 mm at the entrance and exit windows.

Six high resolution NaI(Tl) detectors surrounded the target and were used to detect photons, recoil protons and charged pions. For the $p(\gamma,\gamma)$ and $p(\gamma,\pi^0)$ reactions, photons were detected in a large volume NaI(Tl) crystal (48 cm diameter $\times$ 48 cm deep), while recoil protons were tracked through wire chambers and stopped in an array of plastic scintillators. This arrangement is shown in Fig. 4. A 2.5 cm thick plastic scintillator (BC 408 [49]) in front of the large

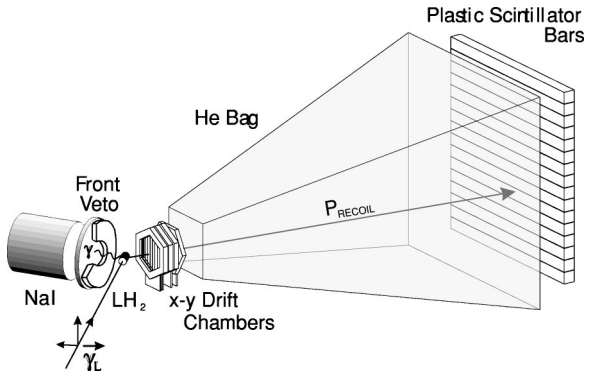

FIG. 4. Arrangement of detectors used to identify γ+proton coincidences, with photons measured in a large NaI(Tl) crystal and protons tracked through wire chambers and stopped in an array of scintillators 4 m from the target. A lead collimator is shown cut away to expose the plastic veto scintillator in front of the NaI.

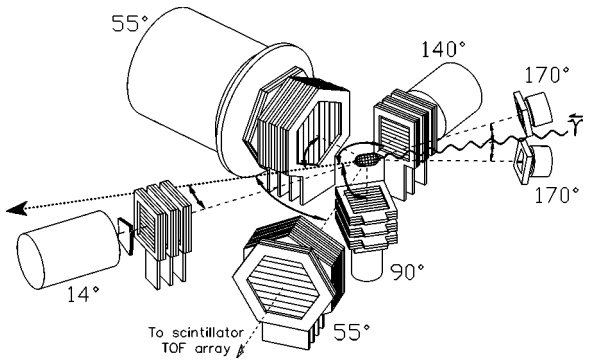

FIG. 5. The detectors used during the third data group (see Table I), labeled by their central lab angles. The NaI(Tl) crystals at 90° and at 170° are in the vertical plane, above and below the beam line. The rest of the detectors are in the horizontal plane. The NaI(Tl) centered at 55° was used both by itself to detect π^+ from $p(\gamma,\pi^+)$ and in coincidence with the time-of-flight arm (labeled TOF here) for $\gamma+p$ events from $p(\gamma,\gamma)$ and $p(\gamma,\pi^0)$, as shown in Fig. 4.

NaI separated neutral and charged particles, and in front of this a 5 cm thick lead collimator with a conical aperture restricted the acceptance to the full diameter of the NaI at its back face. Although 5 cm of lead will stop all protons and pions produced in the target, this thickness is not sufficient to completely absorb the energy of a high energy photon. Nonetheless, it does guarantee the generation of an electromagnetic shower which will be detected by the 2.5 cm thick plastic immediately behind it, thus providing an efficient, compact active collimator for γ rays. On the recoil arm, a stack of 7 high resolution drift chambers were used to reconstruct proton trajectories. Six of these were oriented with wires vertical to measure position in the horizontal plane (*x chambers*) and one was oriented with wires horizontal (*y chamber*). This combination determined proton reaction angles to about 0.4°, FWHM, limited by multiple scattering in the target. A thin-walled helium bag after the wire chambers minimized further multiple scattering. The protons stopped in an array of 16 plastic scintillator bars (BC 408), each 10 cm by 10 cm by 160 cm long, stacked in a wall 4 m from the target to provide a long time of flight (TOF). The relative timing of light signals from opposite ends of these bars provided a horizontal position (to $\sim$7 cm, FWHM) while the segmentation of the array determined the vertical position. This provided a second independent measurement of proton angles, with an accuracy of about 1.4°, FWHM.

Data were collected in three groups of runs corresponding to three different angular settings of the 48 cm diameter NaI and TOF detectors. The central laboratory angles for the NaI ($\overline{\theta}_{lab}$) and recoil arms ($\overline{\Psi}_R$) are listed in Table I, along with the center of mass (c.m.) angles of the different channels for which data were extracted. The detector settings were chosen so as to provide an overlapping angular range to verify consistency between the three groups of data.

During the third group of data runs, a set of four wire chambers (identical to those used on the recoil TOF arm) was installed in front of the 48 cm diameter NaI to provide simultaneous tracking of charged pions. An additional five NaI crystals were also used during the *group III* runs to

TABLE I. Detectors, settings, and corresponding c.m. angles for the three data groups.

Data group	NaI size (cm)	$\overline{\theta}_{lab}$	($\overline{\Psi}_R$)	$\theta^{p(\gamma,\gamma)}_{\text{c.m.}}$	$\theta^{p(\gamma,\pi^0)}_{\text{c.m.}}$	$\theta^{p(\gamma,\pi^+)}_{\text{c.m.}}$
II	48×48	107°	(−30°)	135°, 125°, 115°, 105°	130°, 120°, 110°, 100°, 90°	
I	48×48	76°	(−44°)	105°, 90°, 75°	100°, 90°, 80°, 70°	
III	48×48	55°	(−55°)	75°, 65°,	70°, 60°	85°, 75°,
		55°				65°, 55°
III	24×36	14°			150°	20°
III	13×15	90°				105°
III	24×25	140°				150°
III	8×13	170°				170°
III	8×13	170°				170°

obtain a broad sampling of the $p(\gamma,\pi^+)$ angular distribution. The recoil neutron was not detected in any of the $p(\gamma,\pi^+)$ measurements. The dimensions and angular settings of the *group III* detectors are listed in Table I and their arrangement is shown in Fig. 5. The detectors at 90° lab and 140° lab were preceded by wire chambers that were used to track π^+ events and to define the solid angles.

In addition to defining solid angles, wire chambers provide the potential for reconstructing the source of emitted particles. However, this latter capability disappears at extreme angles where the detector is essentially looking down the beam axis. On the other hand, for these angles a small and accurately known azimuthal acceptance must be maintained to avoid large errors on the polarization asymmetry. For these reasons the solid angle of the 170° NaI crystals for π^+ events was defined by lead collimators having tapered apertures whose cross sections were formed from arcs defining a fixed azimuthal acceptance. The same technique could have been used for the 14° NaI crystal which detected both forward-angle π^+ and recoil protons corresponding to backward-angle π^0 production. However, because of the concern for placing lead in the path of forward going $e^{\pm}$ from atomic pair production, this detector was preceded instead by a pair of scintillators in the shape of arcs defining a fixed azimuthal acceptance. These were used to define the solid angle. (By requiring a coincidence between these scintillators, false triggers from the Cerenkov effect in the nonoverlapping light guides were eliminated.) Wire chambers preceding these scintillators were installed for part of the running period and were used to check the efficiency of these arc-shaped scintillators.

The light from all of the NaI(Tl) crystals in this experiment was collected using Hamamatsu R1911 [50] photomultiplier tubes and voltage dividers equipped with temperature-compensated resistors. This combination produced a highly linear and stable response. The gains of the NaI tubes (and those on the plastic bar array) were continuously monitored with a pulsed HeCd laser system. Shifts in NaI gains were found to be insignificant over the time scales of any of the data groups ($\sim$2 months each).

IV. ANALYSIS OF COMPTON AND π^0 PRODUCTION

A. The $(\gamma,\gamma)/(\gamma,\pi^0)$ separation

The $p(\gamma,\gamma)$ and $p(\gamma,\pi^0)$ reactions were separated with the detectors shown in Fig. 4. An event in the 48 cm diameter NaI triggered the data acquisition system, and a software coincidence was required with the TOF arm. Protons were identified by comparing the energy deposited in the scintillator bars with the corresponding TOF. A spectrum is shown in the top panel of Fig. 6 from the *group I* data. Spectra from the other data *groups* are virtually identical. This plot contains contributions from protons, and electrons and positrons, as indicated. (Charged pions would overlap with the $e^{\pm}$ band, but are essentially eliminated by the requirement of an accompanying high energy γ ray with energy greater than 100 MeV.) Because electrons undergo considerable multiple scattering even in thin amounts of material, the additional requirement of a low χ^2 ($\leqslant 3$) from a linear fit of the tracks

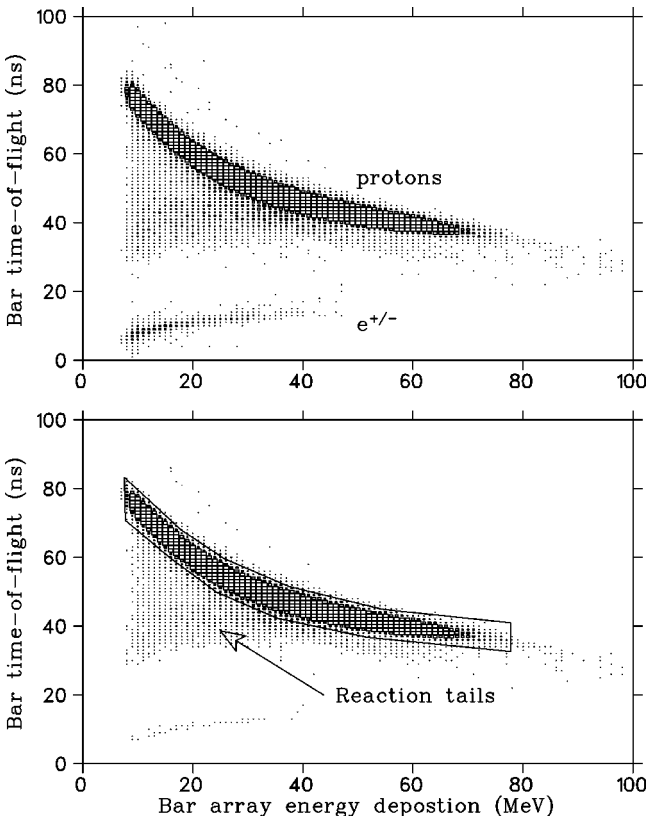

FIG. 6. Energy deposition in the array of plastic scintillator bars of Fig. 4 plotted against the TOF to the bars, shown without (top) and with (bottom) the requirement of a straight track through the wire chambers. The polygon in the bottom panel defines the region used in the Compton/π^0 analysis.

in the six *x-wire chambers* eliminated almost all $e^{\pm}$ events (bottom panel of Fig. 6). The polygonal arc surrounding the dense band in the lower panel defines the region of accepted proton events. Events to the left of this area are due to nuclear reactions in the plastic bars. It is important to exclude these events since they are associated with an incorrect energy signal and would confuse the kinematic identification of the Compton and π^0 channels.

The drift chambers on the TOF arm provided precision tracking of charged particle events. In addition to simple $e^{\pm}$ rejection and the determination of reaction angles, they were used to project the track onto the plastic bar array. The predicted horizontal coordinate (wc_x^{bars}) was compared to the bar position determined from the time difference of the light signals at opposite ends of the scintillator (bar_x), and agreement was required to within $|wc_x^{bars}-bar_x| \leqslant 20$ cm. In the dimension perpendicular to the reaction plane, the bar segmentation (bar_y) and the vertical wire chamber position (wc_y) were used to project the ray back to the beam axis, and the position was required to fall within ± 5 cm of the target center. These requirements eliminated virtually all $e^{\pm}$ events not already suppressed by the *x-chamber* χ^2 cut. The *x chambers* were also used to project tracks back to the beam axis to form an image of the source of emitted particles. This is shown in Fig. 7 for the *group I* data. The vertical lines indicate the physical limits of the target cell. The broadening

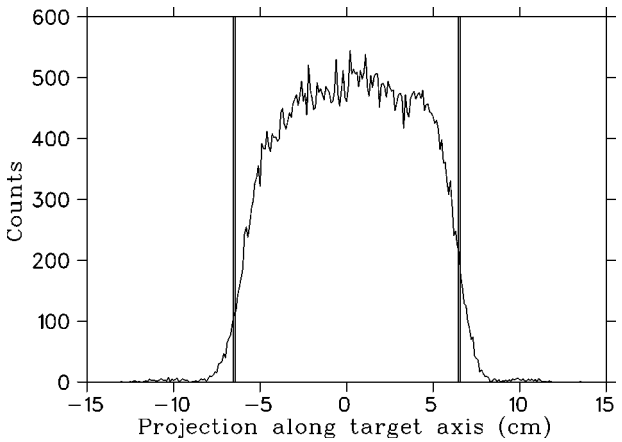

FIG. 7. Projection of tracks from the TOF wire chambers onto the beam axis for the *group I* data. The vertical lines indicate the physical length of the target.

of the target edges is due partly to its rounded end caps, but mostly to the uncertainty in the depth within the target at which events originate. The latter effect smears the source resolution when the laboratory recoil angle is different from 90°. For the *group I* data, $\overline{\Psi}_R = -44°$, as listed in Table I. The small peaks to either side of the target cell (at about ± 10.5 cm) are produced by the Mylar vacuum windows at the entrance and exit of the target chamber. The target definition was slightly better for the *group III* data ($\overline{\Psi}_R = -55°$) and a little worse for the *group II* data ($\overline{\Psi}_R = -30°$). In all cases, the reconstruction resolution was sufficient to completely remove the contributions from vacuum windows by restricting to source points within ± 9 cm of the target center (Fig. 7).

The $p(\gamma,\gamma)$ and $p(\gamma,\pi^0)$ channels have been separated by comparing the γ-ray energy deposited in the 48 cm diameter NaI with the proton TOF to the bar array. This is shown in Fig. 8, where the energy expected for Compton scattering, as calculated from the angles measured in the wire chambers and the tagged beam energy, has been subtracted from the abscissa. The net recoil TOF has been constructed as the weighted mean of the time deduced from the proton energy deposited in the plastic scintillator bars and the direct flight-time measurement, the latter being dominant due to its smaller uncertainty. (This net TOF is essentially the distance along the polygonal arc in the proton identification plot; Fig. 6, bottom.) The expected TOF, calculated again from the angles measured in the wire chambers and the tagged beam energy assuming $p(\gamma,\gamma p)$ kinematics, has been subtracted from the ordinate in forming the plots of Fig. 8. Results are shown here for $120° \pm 5°$, $90° \pm 5°$, and $60° \pm 5°$ c.m. from the *group II*, *group I* and *group III data*, in the top, center and bottom panels, respectively. In each case, Compton scattering events are clearly resolved in a peak centered at the origin. These particular plots have been made for the tagging interval between 290 MeV and 333 MeV. The channel separation is even larger for lower tagging energies.

Since the energy of π^0-decay photons is always less than that of Compton scattering, π^0 events appear at negative values of ΔE in the plots of Fig. 8. The low-ΔE limit at the

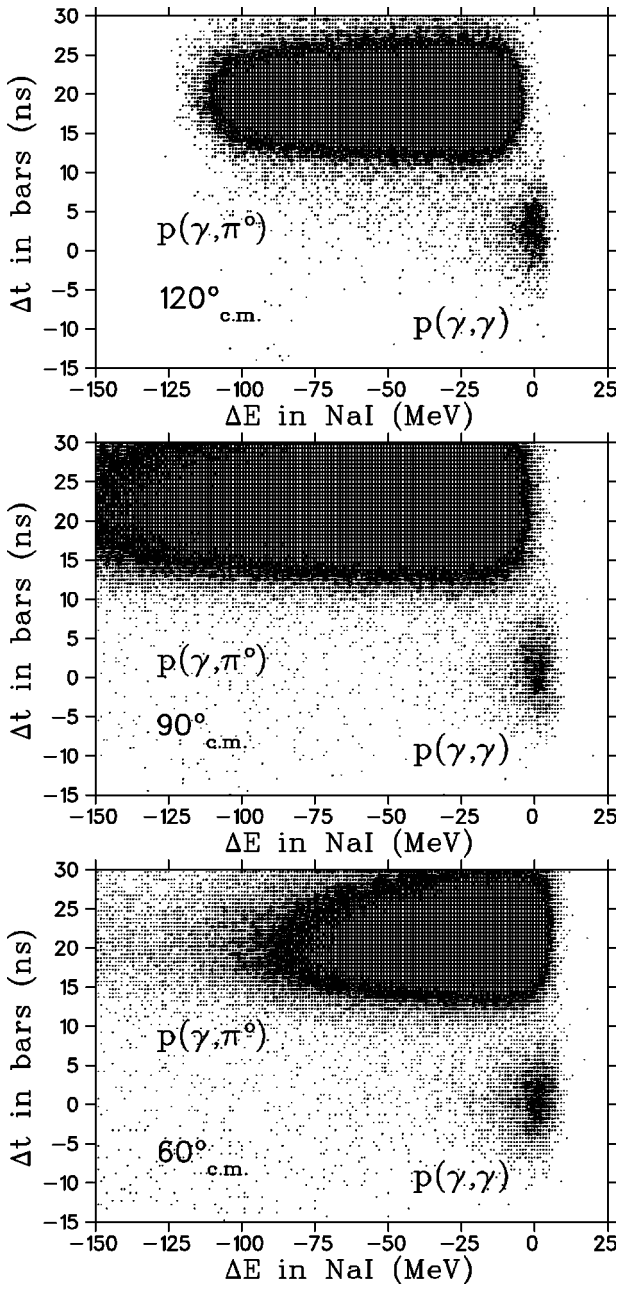

FIG. 8. Recoil proton TOF to the plastic bar array, plotted against energy deposited in the 48 cm diameter NaI. For both axes the values expected for Compton scattering, calculated from the angles determined by the TOF wire chambers and the tagged beam energy, have been subtracted. Results for 10° bins centered at 120°, 90°, and 60° c.m. from the *group II*, *group I*, and *group III* data are shown in the top, center, and bottom panels, respectively, for the tagging interval $290 < E_\gamma < 333$ MeV.

left side of the π^0 cluster in the top panel is created by the combination of Compton kinematics and a 100 MeV NaI threshold that was imposed on all three data *groups*. As the γ-ray angle decreases (center panel of Fig. 8), the expected Compton energy increases which extends the π^0 cluster to more negative ΔE values. Similarly, recoil protons from π^0 production are always lower in energy than those from Compton scattering, and thus have a longer TOF. As a result,

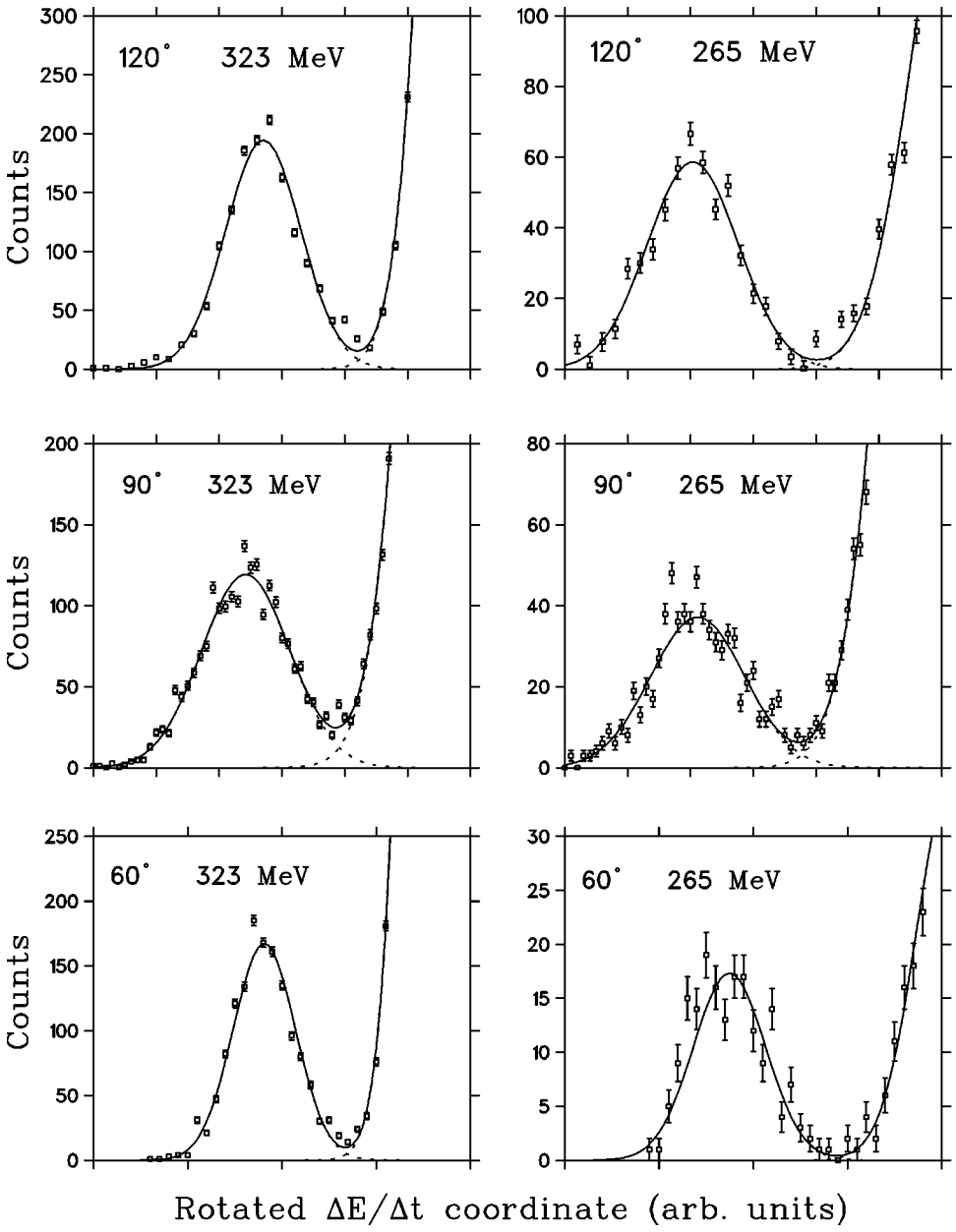

FIG. 9. Spectra of events below a line rotated $\sim 30°$ between the (γ,γ) and (γ,π^0) peaks in plots similar to Fig. 8, shown here for two tagged energies (right and left panels). The high energy peaks result from Compton scattering. The data in the top, center, and bottom panels are from the *group II*, *group I*, and *group III* sets, respectively.

the π^0 clusters extend to positive values of Δt in the plots of Fig. 8. The larger γ-ray angles are associated with higher energy recoils and shorter TOFs. The cutoff of the π^0 cluster below $\Delta E \approx -75$ MeV in the lower panel results from the low proton energies associated with this forward γ-ray angle. Here, most of the low energy π^0-recoil protons are stopped in the target.

Compton scattering yields were extracted from spectra similar to those of Fig. 8 by cutting data with NaI energies different from the Compton process by more than ΔE_0^{NaI}, where $|\Delta E_0^{NaI}| \leqslant 20$, 20, and 30 MeV thresholds were used with the *group II*, *group I* and *group III* sets, respectively. The remaining high energy events were projected onto a line rotated by about $+30°$ from the energy axis [parallel to a line between the (γ,γ) and (γ,π^0) peaks]. These projections are shown in Fig. 9 for two tagged energies, 323 MeV and 265 MeV. The data in the top, center, and bottom panels are from the *group II*, *group I*, and *group III* sets, respectively. (Accidental coincidences with the tagger have been treated in the same way for these reactions as for the beam flux measurement, Sec. II, and have been subtracted from these spectra.) The widths of the high energy peaks from Compton scattering are dominated by the energy loss of the recoil protons in the hydrogen target, and in the rotated coordinate system of Fig. 9 their shape is essentially Gaussian. (The ΔE_0^{NaI} cut reduces the π^0 background in these rotated-coordinate spectra. The cutoff used with the *group III* data, 30 MeV, is the largest because the π^0 peak in Fig. 8 is the most limited for the low proton energies associated with that angle.) The spectra of Fig. 9 were fit to separate Compton scattering from the residual tail of π^0 events. The yields from the two polarization states were extracted by first fitting

the sum of spectra from the two states, using the result to fix the line shape parameters, and then refitting the individual polarization states by varying only the peak area. (Various fitting procedures were explored, but the result was insensitive to the method because of the high degree of separation between the Compton and π^0 peaks.)

The (γ,π^0) yields have been extracted by making a rough cut to exclude most of the Compton events (without truncating tails from the π^0 peak) in plots similar to those of Fig. 8, and summing the remaining counts. The Compton cross section is such a small fraction of π^0 production that further fitting cannot affect the experimental uncertainties in the π^0 cross sections.

Empty target data were collected for each of the three measurement *groups* in order to sample the contribution from the walls of the target cell. These were analyzed with the same requirements used to extract Compton scattering and π^0 production, but subtractions proved unnecessary since the number of events surviving these requirements was completely negligible.

B. Measurement of detector efficiencies

Events were added to the NaI energy verses TOF histograms used to separate the Compton and π^0-production channels (as in Fig. 8) only when the following criteria were fulfilled: the recoil proton had an energy and TOF within a polygonal arc similar to that shown in the bottom panel of Fig. 6; the fit of the six TOF *x-wire-chamber* positions to a straight line had a reduced $\chi^2 \leqslant 3$; the *x projection* of the wire-chamber track onto the bar array agreed to within 20 cm of the hit position recorded by the bars, $|wc_x^{bars} - bar_x| \leqslant 20$ cm; the *x projection* of the wire-chamber track back to the beam axis was consistent with an event originating in the target cell ($-9 < z < +9$ cm in Fig. 7); the *y projection* of the track back to the beam axis, using the bar position (bar_y) and the vertical wire chamber (wc_y), fell within ± 5 cm of the target axis; the 2.5 cm plastic *veto* in front of the 48 cm diameter NaI had less than 5 MeV deposited energy.

Each of these requirements has an efficiency associated with it. While Compton and π^0 production are both two-body reactions, and as such are completely specified by two kinematic observables, in fact eight kinematic variables have been measured in this experiment: the tagged beam energy; the proton *time of flight* to the bar array; the energy deposited by the proton in the scintillator bar array; the polar and azimuthal angles of the recoil proton measured in the TOF-arm wire chambers; the proton recoil angles determined again by the hit position in the bar array; the γ-ray energy in the 48 cm diameter NaI.

In addition to providing the first unambiguous separation of the $p(\gamma,\gamma)$ and $p(\gamma,\pi^0)$ reactions, this large kinematic overdetermination has allowed us to deduce the detector efficiencies directly from the data themselves, thus avoiding potential systematic uncertainties associated with simulations. We describe each of these efficiency measurements in turn.

1. Scintillator-bar-array efficiency

A proton is identified in the array of plastic scintillator bars on the TOF arm as an event within a polygonal area similar to that shown in the lower panel of Fig. 6. The efficiency of this requirement can be directly measured by using non-bar variables to guarantee that a proton was incident on the bar array. The fraction of these with valid bar signals is then the net bar efficiency.

The TOF wire chambers are sensitive only to charged particles and can be used to restrict their source to the liquid hydrogen. The additional requirement of a high-energy signal (>100 MeV) in the 48 cm diameter NaI from a neutral particle (with no signal in its front veto plastic) eliminates the $p(\gamma,\pi^+)n$ reaction. Thus, protons in the bars are guaranteed by requiring a single electron in the tagger, N^{tag}_{1-hit}, a neutral high-energy NaI signal, $N^{NaI}_{\gamma>100}$, and a wire-chamber track that passes the χ^2 test for a straight line, $N^{wc_x}_{\chi^2}$, coming from the central 10 cm of the 13 cm long target, $N^{wc_x}_{tgt_{10}}$, and pointed at the bar array, $N^{wc}_{\rightarrow bar}$. For N^{bar}_p events satisfying the proton requirements imposed on bar signals (that is with bar_x hit positions within 20 cm of the values predicted by the *x chambers*, with bar_y positions which project back through the *y chamber* to within ± 5 cm of the target axis, and with bar energy and TOF falling within the polygonal bands in bar identification plots as in Fig. 6), the bar array efficiency for protons is given by

$$\text{bar eff} = \frac{\{N^{tag}_{1-hit} \cap N^{NaI}_{\gamma>100} \cap N^{wc_x}_{\chi^2} \cap N^{wc_x}_{tgt_{10}} \cap N^{wc}_{\rightarrow bar}\} \cap N^{bar}_p}{\{N^{tag}_{1-hit} \cap N^{NaI}_{\gamma>100} \cap N^{wc_x}_{\chi^2} \cap N^{wc_x}_{tgt_{10}} \cap N^{wc}_{\rightarrow bar}\}}. \tag{4a}$$

This net efficiency includes all possible effects encountered after the proton leaves the wire chambers: multiple scattering, dead layers, and lost signal from nuclear reactions in the detector material.

The bar detection efficiency depends upon energy, and since the data are dominated by π^0 production, the proton (vertex) energy can be reconstructed from the wire-chamber angle and tagged-beam energy assuming $p(\gamma,p)\pi^0$ kinematics. The efficiency from the *group II* data for the central ± 70 cm of the array (avoiding the edges of the ± 80 cm bars) is plotted as a function of proton vertex energy in the top panel of Fig. 10 as open circles. The solid curve is a fit of a smooth function to these data points. Since the scintillation light is collected at either end of each bar, there can be an additional position dependence to the *bar eff*. This is shown in the lower panel of Fig. 10. There, the parametrized energy dependence (the solid curve in the top panel) is divided out to expose the separate position dependence. The full two dimensional map of *bar eff* is shown in Fig. 11 using the smooth functions that were fitted to the measurements (the solid curves of Fig. 10). In general, data extraction was limited to regions of detector response where the efficiency was slowly varying. The only exception was in the minimum proton vertex energy where the efficiency was allowed to drop to 66%. (This is a compromise in extracting data at as low a beam energy as possible without having too large an efficiency correction.) The vertical lines in Fig. 10, and the heavy lines in Fig. 11, indicate these extraction thresholds.

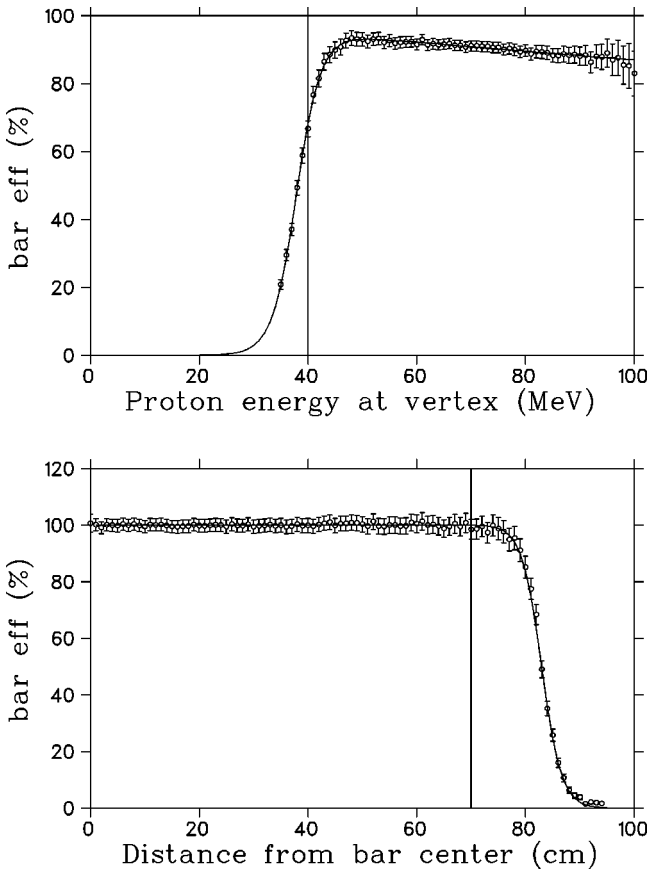

FIG. 10. Measured efficiency for proton detection (open circles) in the TOF-bar array as a function of proton vertex energy, top. A smooth function fitted to these data (solid curve in the top panel) was used to divide out this energy dependence from the efficiency verses position plot shown in the bottom panel. Vertical lines indicate thresholds used in data extraction.

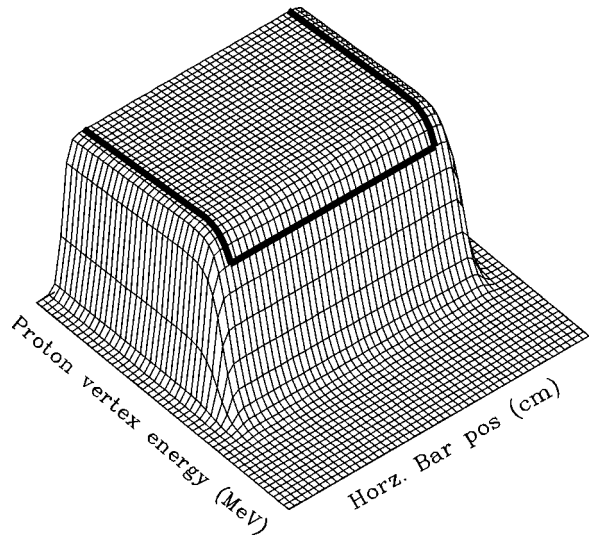

FIG. 11. Efficiency of the plastic bar array as a function of both vertex energy and horizontal bar position, using smooth parameterizations of the data (such as the solid curves of Fig. 10). Heavy lines indicate thresholds used in data extraction.

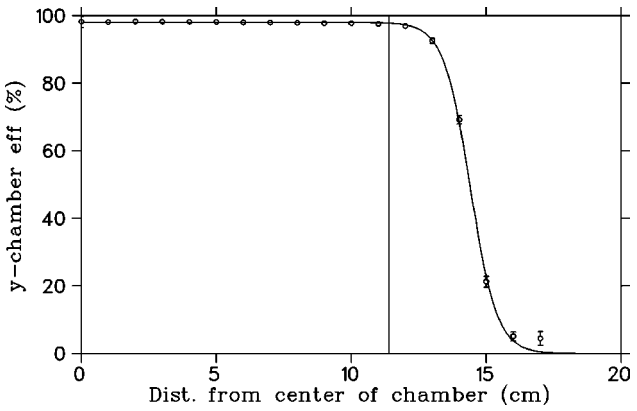

FIG. 12. Measured efficiency for protons in the *y-wire-chamber* of the TOF arm (open circles) as a function of distance from the center of the chamber. The solid curve shows a smooth function fitted to the data. The vertical line indicates the limit used in data extraction.

The bar efficiencies are very similar in the *group I* and *group III* data sets, although the dynamic range of proton energies is somewhat less.

2. Wire-chamber efficiencies

The seven drift chambers used to track charged particles on the TOF arm were all identical in construction, six oriented with wires vertical (*x chambers*) and one oriented with wires horizontal (*y chamber*). The geometrical layout of detectors in Fig. 4 guaranteed that any proton originating from the region of the target, including the liquid H_2 cell and the mylar vacuum chamber windows, which reached the plastic bar array had to have passed through the stack of wire chambers. The position of a charged particle in the *y chamber* could be predicted from the *x chamber* track and the hit position on the bar array. Thus, protons in the *y chamber* could be guaranteed from *non-y-chamber* observables by requiring a single hit in the tagger, N^{tag}_{1-hit}, a neutral high-energy NaI signal, $N^{NaI}_{\gamma>100}$, an *x-chamber* track that passes the χ^2 test for a straight line, $N^{wc_x}_{\chi^2}$, with bar_x hit positions within 20 cm of the values predicted by the *x chambers*, $N^{wc_x-bar_x}_{\leqslant 20}$, and an energy and TOF lying within the polygonal bands in bar identification plots, N^{bar}_{ID}. With $N^{wc_y}_{p}$ events detected in the *y chamber*, its proton efficiency is

$$wc_y \text{ eff} = \frac{\{N^{tag}_{1-hit} \cap N^{NaI}_{\gamma>100} \cap N^{wc_x}_{\chi^2} \cap N^{wc_x-bar_x}_{\leqslant 20} \cap N^{bar}_{ID}\} \cap N^{wc_y}_{p}}{\{N^{tag}_{1-hit} \cap N^{NaI}_{\gamma>100} \cap N^{wc_x}_{\chi^2} \cap N^{wc_x-bar_x}_{\leqslant 20} \cap N^{bar}_{ID}\}}. \tag{4b}$$

This efficiency is shown for the *group I* data as a function of the distance from the center of the chamber in Fig. 12. The full two-dimensional map of the *y-chamber* efficiency is shown in Fig. 13, and displays the hexagonal shape of the wire chamber frames. Regions near the frames for which the efficiency was rapidly varying were avoided during data

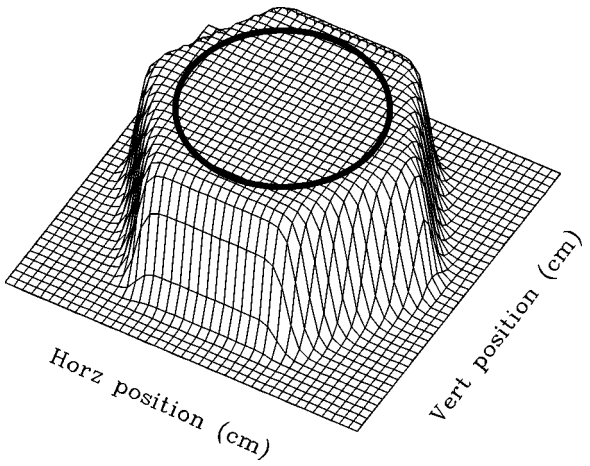

FIG. 13. Two dimensional map of the *y-wire-chamber* proton efficiency using smooth parametrizations of the data (such as the solid curve in Fig. 12). Data extraction was limited to the interior of the indicated circle.

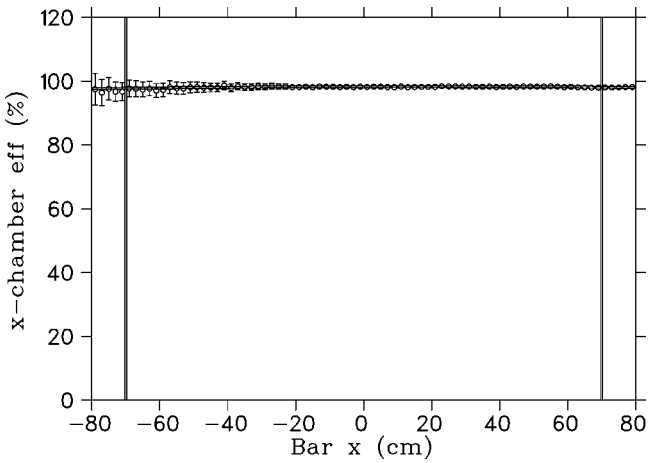

FIG. 14. The measured net efficiency of the tracking algorithm used with *x-wire-chambers* of the TOF arm, plotted as a function of bar_x for the *group I* data. The center of the bar array corresponds to $bar_x = 0$. Reaction angles increase, and proton energies decrease, as bar_x becomes increasingly negative.

analysis. The vertical line in Fig. 12 and the circle in Fig. 13 show the maximum radius (11.4 cm) used in the Compton and π^0 analyses. The measured efficiencies for the *group II* and *group III* data are very similar.

Efficiency maps similar to those of Fig. 12 and Fig. 13 can be developed for each of the *x chambers* in turn by using the other chambers to define charged particle trajectories. Because of the χ^2 test applied to the fit of the *x-chamber* signals, it is convenient to develop a net efficiency for the full stack of six *x chambers* and their track-reconstruction algorithm. Protons in the *x-chamber* stack can be guaranteed from *non-x-chamber* observables by requiring a single hit in the tagger, N^{tag}_{1-hit}, a neutral high-energy NaI signal, $N^{NaI}_{\gamma>100}$, an energy and TOF in the bars within the polygonal bands in identification plots similar to Fig. 6, N^{bar}_{ID}, and with bar_y positions which project back through the *y chamber* to within ± 5 cm of the target axis, $N^{bar_y+wc_y}_{tgt\pm 5}$. For $N^{wc_x}_{\chi^2}$ protons having *x-chamber* tracks that pass the $\chi^2 \leqslant 3$ test for a straight line, the net *x-chamber* reconstruction efficiency is

$$wc_x \text{ eff} = \frac{\{N^{tag}_{1-hit} \cap N^{NaI}_{\gamma>100} \cap N^{bar}_{ID} \cap N^{bar_y+wc_y}_{tgt\pm 5}\} \cap N^{wc_x}_{\chi^2}}{\{N^{tag}_{1-hit} \cap N^{NaI}_{\gamma>100} \cap N^{bar}_{ID} \cap N^{bar_y+wc_y}_{tgt\pm 5}\}}. \tag{4c}$$

This net *x-chamber* efficiency is plotted in Fig. 14 as a function of bar_x for the *group I* data. Because of the two-body nature of the reactions, the bar_x variable combines both position and energy dependence, with proton recoil energy decreasing to the left. The solid curve is a smooth function fitted to the data. The vertical lines mark the ± 70 cm limits of the ± 80 cm bars that were in the final analyses. The same maximum radius cut as in Fig. 12 (11.4 cm) was used with the *x-chambers* in the Compton and π^0 analyses to avoid regions near the frames where efficiencies varied rapidly. The measured efficiencies for the *group II* and *group III* data are very similar.

3. Large-NaI-veto efficiency

Signals in the 2.5 cm veto plastic scintillator preceding the 48 cm diameter NaI are used to eliminate charged particle events. This results in rejection of some γ rays due to either $e^{\pm}$ pair production while transmitting this plastic veto or to leakage coming back from electromagnetic shower production in the large NaI crystal. Photons from either $p(\gamma,\gamma)$ or $p(\gamma,\pi^0)$ incident on this veto scintillator are guaranteed from nonveto observables by the same requirements used in the data analysis: a single hit in the tagger, N^{tag}_{1-hit}, a high-energy NaI signal, $N^{NaI}_{\gamma>100}$, and a valid proton event in the TOF bar array (i.e., with energy and TOF within the polygonal bands in proton identification plots, with *x-chamber* tracks that pass the $\chi^2 \leqslant 3$ test for a straight line, with bar_x hit positions within 20 cm of the values predicted by the *x chambers*, and with bar_y positions which project back through the *y chamber* to within ± 5 cm of the target axis), N^{bar}_{p}. With N^{veto} events in the 2.5 cm plastic scintillator, the net NaI+veto efficiency for photon detection is

$$\text{NaI eff} = 1 - \frac{\{N^{tag}_{1-hit} \cap N^{NaI}_{\gamma>100} \cap N^{bar}_{p}\} \cap N^{veto}}{\{N^{tag}_{1-hit} \cap N^{NaI}_{\gamma>100} \cap N^{bar}_{p}\}}. \tag{4d}$$

This net NaI eff was computed separately for the $p(\gamma,\gamma)$ and $p(\gamma,\pi^0)$ reactions by selecting the appropriate peak in the ΔE versus TOF plots (Fig. 8) with a cut along a line rotated $\sim 30°$ with respect to the NaI energy axis. The results from the *group I* data are shown in Fig. 15 as a function of the threshold in the veto scintillator. The measurements from the *group II* and *group III* sets are very similar. A veto threshold of 5 MeV was used for all cross section extractions. The fraction of Compton events rejected by the veto plastic is less because the TOF arm requirements on the recoil proton guarantee that the corresponding scattered γ rays are completely contained within the aperture of the lead collimator that is located just before the front veto. In contrast, the

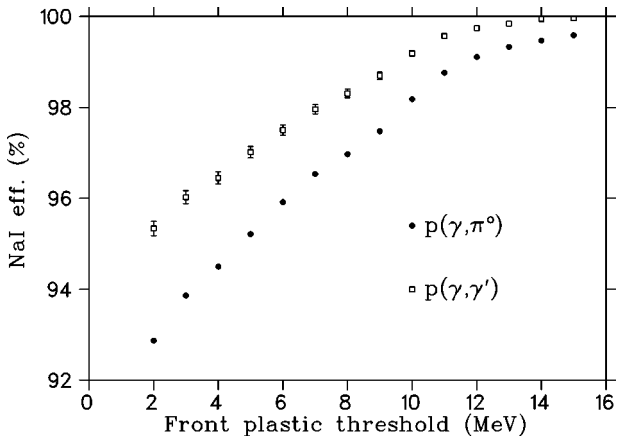

FIG. 15. The measured net efficiency of the 48 cm diameter NaI, due to photon rejection by the front veto plastic, as a function of the energy threshold in the veto scintillator.

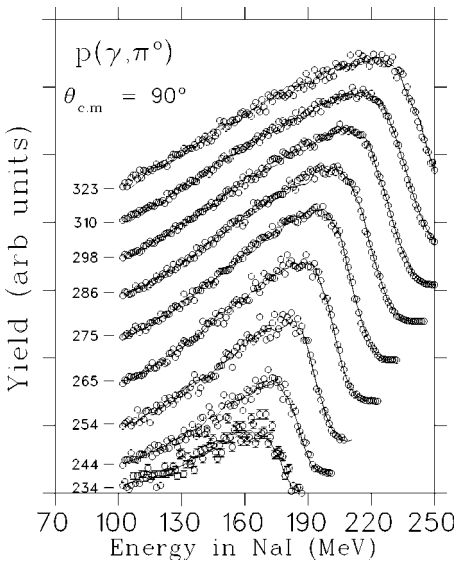

FIG. 16. High-energy $p(\gamma,\pi^0)$ γ-ray spectra from the *group I* measurements. Data for nine tagged beam energies between 234 MeV and 323 MeV are shown, offset, as open circles. Monte Carlo generated spectra, with a NaI response function fitted to these data, are shown as solid curves.

photons from π^0 production illuminate a much larger area, and those that skim the inner surface of the lead aperture can produce a single $e^{\pm}$ pair, thus triggering the veto plastic while still depositing most of the photon energy in the large NaI. To minimize this, the lead collimator is conically tapered to project back to the center of the target. Nonetheless, the effect of this lead skin-thickness is somewhat enhanced by the finite extent of the target with the result that the net γ-ray efficiencies for $p(\gamma,\pi^0)$ are slightly smaller.

C. Large-NaI calibration

An accurate knowledge of the 48 cm diameter NaI response function is needed for optimal separation of the Compton and π^0 channels. This was determined separately for each of the three data *groups*. (Although it is straightforward to place this detector directly in the tagged beam, such a measurement does not actually reproduce the experimental conditions of γ rays filling a large conical acceptance.)

Both the calibration and the line shape of the NaI response function were measured directly from the π^0 data. NaI spectra from $p(\gamma,\pi^0)$, with a cut in the energy- and TOF-difference spectra (Fig. 8) to eliminate Compton events, were fitted for each tag bin simultaneously. Data from the *group I* measurements are shown in Fig. 16 as open circles, with the central tag energy indicated to the left of each spectrum. These were simulated with GEANT [51]. All tagged energies were fitted simultaneously, varying only three parameters (other than the numbers of counts): the slope and offset in a linear energy calibration, and the width of a Gaussian smearing function that was applied to the GEANT predictions to account for nonuniformities in the NaI crystal. The resulting Monte Carlo generated spectra are shown as the solid curves. The agreement in the *group II* and *group III* data is of equally high quality.

The Compton data provide a cross-check on the NaI calibration and line shape. NaI yields from $p(\gamma,\gamma)$, using a cut in the energy- and TOF-difference spectra (Fig. 8) to eliminate π^0 production, are shown in Fig. 17 (open circles) for two tagged beam energies from the *group I* data. The ΔE_0^{NaI} measured-minus-calculated energy difference requirement of Sec. IV A was not imposed in generating the spectra of Fig. 17 in order to expose the tail of the NaI response. The solid curves are the line shapes predicted from the fits to the π^0 data shown in Fig. 16, allowing only the peak areas to vary. The agreement here, as at other energies, is excellent.

As a final check on the fits to the π^0 data, we show in Fig. 18 the calibration of the 48 cm diameter NaI measured immediately prior to the *group I* data period by placing the detector directly in the tagged photon beam (open circles). The calibration deduced from the fits to the π^0 spectra of Fig. 16 is shown as the solid line.

D. Monte Carlo corrections for (γ,γ) and (γ,π^0)

There are a few parameters needed to construct cross sections that cannot be directly measured, and for which we must rely on Monte Carlo simulations.

Corrections are made for events that are lost due either to secondary reactions in the target or, at low energies, for recoil protons that stop in the target.

The effective target length from the extended target and the geometrical solid angle subtended by angular bins with a moderate polar acceptance and a large azimuthal acceptance is determined by Monte Carlo.

Finally, for the Compton analysis, a correction is made for γ rays that produce signals in the tail of the NaI response that are below the ΔE_0^{NaI} thresholds used in the analysis.

Although these corrections are all carried out simultaneously, we discuss them separately below in order to expose the magnitude of each component.

1. Corrections for secondary reactions in the target

A small fraction of the recoil protons undergo secondary nuclear reactions in the target. These are simulated with the

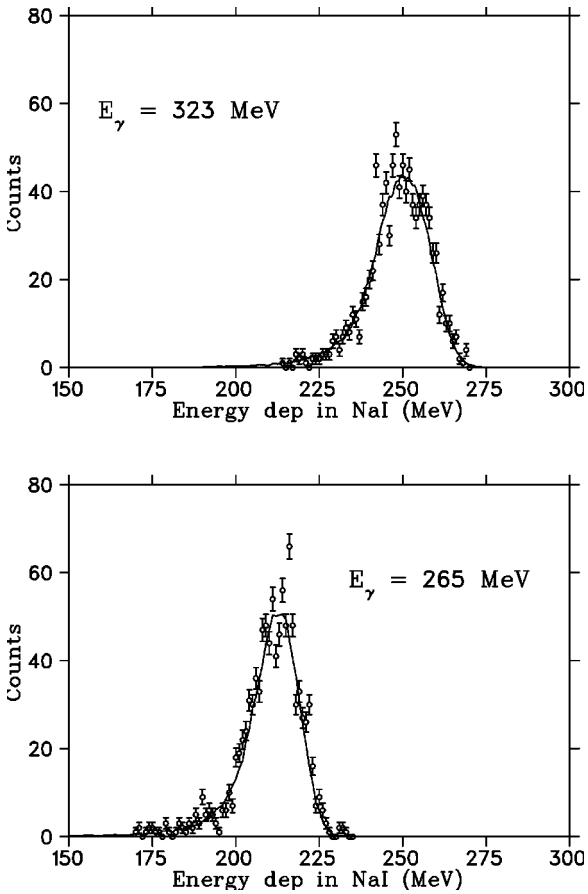

FIG. 17. Compton γ-ray spectra (open circles) for two tagged beam energies from the *group I* data. The solid curves are the line shapes predicted from the fits shown in Fig. 16 with only the areas of the peaks adjusted.

GCALOR hadronic interaction code [52]. This code reliably models hadronic interactions in plastic scintillator (which contain significant amounts of hydrogen), and successfully reproduces data on the ratios of nuclear-reaction-tails to atomic-energy-loss-peaks produced by 10 MeV to 100 MeV protons [53,54]. The percentage of proton recoils from

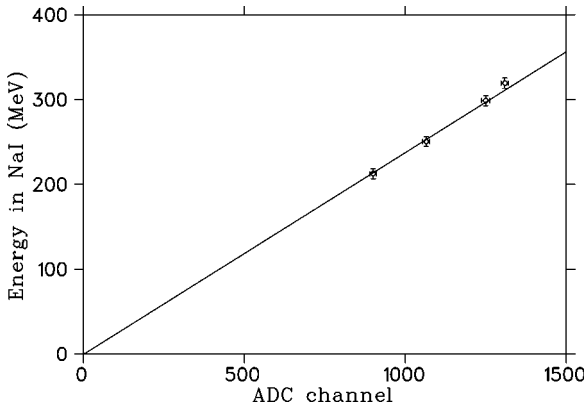

FIG. 18. The calibration of the 48 cm diameter NaI as measured by placing the detector directly in the tagged photon beam (open circles), compared with a prediction from the fits to the π^0 spectra of Fig. 16 (solid line).

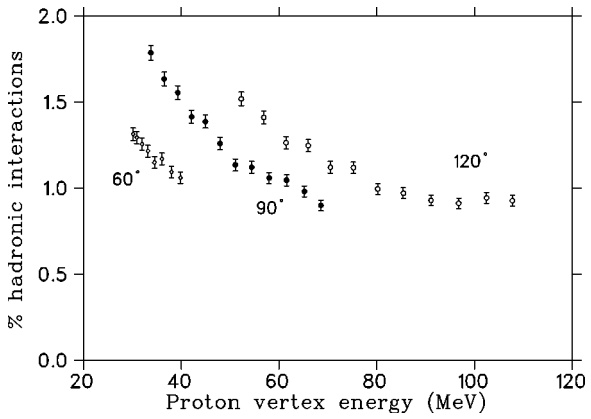

FIG. 19. Fraction of recoil protons that undergo secondary hadronic interactions. Data are shown for one $\pm 5°$ angle bin from each of the three data *groups* of Table I. The lower limit reflects the minimum 30 MeV proton vertex energy required in all the analyses.

Compton scattering that undergo hadronic interactions in the liquid hydrogen target is shown in Fig. 19 for three $\pm 5°$ angular bins from the three data *groups*. These GCALOR results are plotted as a function of the initial energy at the $p(\gamma,\gamma p)$ vertex. The calculations for $p(\gamma,\pi^0 p)$ are virtually identical. Results for energies below 30 MeV are not shown since the requirement of a minimum vertex energy of at least 30 MeV was imposed on all analyses. The rise at low proton vertex energy is due to the increase in the nuclear elastic scattering cross section. The shift between the 60° (*group III*), 90° (*group I*), and 120° (*group II*) points is due to the decreasing recoil angle (Table I) and the associated increase in the length of liquid hydrogen traversed by the recoiling protons. In all cases, secondary nuclear reactions affect less than 2% of the events.

2. Determining the effective target length and solid angle

The effective target length and solid angles from the finite size target and detectors are determined by Monte Carlo simulation. Interaction points are chosen randomly along a fixed cylinder with *sampling target length*, κ_s, that contains the target cell, following the measured beam profile (Fig. 2). Events are distributed into a *sampling solid angle*, Ω_s, defined by a cone spanning a fixed reaction angle. This cone is chosen so as to encompass all angular bins for which data are extracted, regardless of the point of origin within the target, and Ω_s is determined by simple analytic integration. Then, for N_s photons reacting in the sampling target length, κ_s, which produce reaction products in the sampling solid angle, Ω_s, and N_g events that (a) pass all of the experimental cuts applied to the data, and (b) come from an interaction point inside the actual target cell, the effective target-length and solid-angle product is just

$$(\kappa\Omega)^{eff} = \kappa_s \Omega_s \frac{N_g}{N_s}. \tag{5}$$

Atomic interactions are included to account for the decrease in photon flux along the length of the target. Ω_s is chosen to be substantially larger than the physical detectors so as to

include contributions from multiple scattering and secondary reactions, but less than 4π to avoid the needless computation of events that have no chance of entering any of the detectors of interest. Events are spread randomly over Ω_s following an angular distribution that is iterated, converging quickly to the measured distribution.

3. Deconvoluting finite size effects

It is straight forward to show that the cross sections computed using the effective target-length and solid-angle product of Eq. (5), $(d\sigma/d\Omega)_{exp}$, represent an average over the entire *sampling solid angle*, Ω_s. Angular distributions measured in this way can then be used to deconvolute the finite size effects and construct the quantities of theoretical interest—the cross sections that would be observed from a pencil beam on a point target as seen by a point detector. Both the variation of the cross section with reaction angle and the strong azimuthal dependence accompanying a sizable beam asymmetry can result in significant differences between the *point cross sections* and the corresponding average values.

In the Monte Carlo computation of $(\kappa\Omega)^{eff}$, events are spread randomly over Ω_s following an assumed sampling distribution, $\sigma_s(E_\gamma,\theta,\phi)$. The best value for the *point cross section* at any energy and angle is then

$$\frac{d\sigma}{d\Omega}(E_\gamma,\theta,\phi)=\left(\frac{d\sigma}{d\Omega}\right)_{exp}\frac{\sigma_s(E_\gamma,\theta,\phi)}{\int_{\Omega_s}\sigma_s d\Omega/\Omega_s}. \tag{6}$$

If the choice for $\sigma_s(E_\gamma,\theta,\phi)$ is iterated using fits to the measured cross sections, then the left side of Eq. (6) quickly converges to the desired *point cross section*.

We illustrate this procedure with an example from Compton scattering. For reactions with linearly polarized photons and unpolarized targets, the angular dependence of the cross section factorizes into two components,

$$\sigma(\theta,\phi)=\sigma_{unp}(\theta)[1+\Sigma(\theta)\cos(2\phi)], \tag{7}$$

where $\sigma_{unp}(\theta)$ and $\Sigma(\theta)$ are the unpolarized cross section and beam asymmetry that would be measured with 100% polarized photons. To construct the initial *sampling cross section*, $\sigma_{s1}(E_\gamma,\theta,\phi)$, we fit $\sigma_{unp}(\theta)$ and $\Sigma(\theta)$ values predicted by a dispersion calculation [55] to polynomials in $\cos(\theta)$ and E_γ. This is shown as the dotted curve in Fig. 20 for 323 MeV. We use σ_{s1} in the Monte Carlo simulation to distribute events into Ω_s and deduce $(\kappa\Omega)^{eff}$ as in Eq. (5), which is then used to construct experimental cross sections. We insert these into the right hand side of Eq. (6), together with the integral of σ_{s1} over Ω_s. Fits to the left side of Eq. (6) are then used for the second iteration, σ_{s2}, which is shown as the dashed curve in Fig. 20. In this example, the 65° datum was included only in the final fit, which is shown as a solid line. This procedure converges to the final *point* cross sections, shown as solid circles. Although we could have started with flat distributions for σ_{s1}, a reasonable first guess ensures convergence in essentially one iteration. This

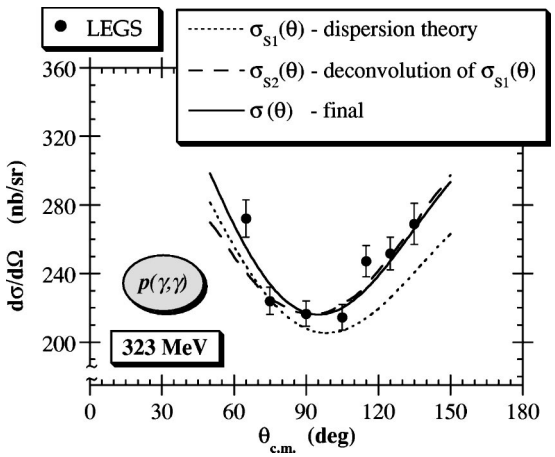

FIG. 20. Iterative stages in the deconvolution of finite size effects for the Compton cross sections at 323 MeV. The first choice for the *sampling* distribution in Eq. (6), σ_{S1}, is a dispersion calculation [55]. Fits to the left side of Eq. (6) are then used for the second iteration, σ_{S2}. This quickly converges to the final points, shown as solid circles (see Sec. IV D 3).

procedure has been applied to all of the LEGS results, and all cross sections plotted and tabulated in this paper represent the deduced *point* values.

Because of the $\cos(2\phi)$ dependence in Eq. (7), it is also necessary to correct the measured asymmetries for finite detector acceptance in order to obtain the corresponding *point* values. This is essentially a correction for those portions of the detector acceptance that are neither in nor perpendicular to the plane containing the photon's electric vector, and is equivalent to modifying the beam polarization with the geometrical factor,

$$P^G=\frac{\int\sigma\cos(2\phi)d\Omega}{\int\sigma d\Omega}, \tag{8}$$

integrated over the detector acceptance. Thus, $P_2^\gamma\sigma_1$ and $P_1^\gamma\sigma_2$ in Eq. (3d) must be multiplied by P_1^G and P_2^G, respectively, to construct the asymmetries that would be seen by a *point* detector. Fortunately, no Monte Carlo simulations are needed here. Since the wire chambers provide the polar and azimuthal angles for each event, these geometrical factors can be directly evaluated from the data for each angle and energy bin as the sum $(1/N_i)\Sigma\cos(2\phi)$ for the N_1 and N_2 events measured with the two polarization states.

4. Measuring the systematic uncertainty in the $p(\gamma,\pi^0)$ acceptance

The Monte Carlo simulations for the Compton scattering and π^0-production channels differ only in the event generators and in the shape of the differential cross sections used to distribute events; in all other aspects they are identical. For Compton scattering, Ω^{eff} is completely determined by the measurement of the recoil proton in the TOF wire chambers, since the accompanying γ ray is entirely contained within the lead aperture of the 48 cm diameter NaI. In contrast, the π^0 channel is considerably more complicated. There, the high

energy π^0-decay photons are spread over a large angular range, and the geometrical acceptance is necessarily a convolution of both proton-recoil and γ-ray arms. In such a case, the effective geometrical solid angle determined by Monte Carlo could potentially be more sensitive to small differences that may exist between the actual and the simulated geometry.

As discussed above, the detector calibrations and efficiencies are measured directly from the data, and the thresholds indicated by the solid lines in Figs. 10 to 14 have been imposed to avoid regions where efficiencies are varying rapidly. This maximal set of criteria leads to what we refer to as the *full acceptance* analyses. With everything but the small component from reactions in the target and the geometrical solid angle now determined directly by measurement, analyses using cuts that are more restrictive than this *full acceptance* treatment should then give the same $p(\gamma,\pi^0)$ cross sections. Variations in these results expose systematic uncertainties in the geometrical acceptance.

We have performed a series of analyses in which the maximum acceptable wire chamber radius, R_{wc}, was reduced from the *full acceptance* of 11.4 cm (Fig. 12 and Fig. 13), and in which the NaI energy threshold was increased above the *full acceptance* of 100 MeV (Fig. 16). The application of these more restrictive requirements changes the distribution of π^0 decay photons and allow us to sample systematic variations in the acceptance. This possibility of *measuring* a component of the systematic uncertainty is a unique by-product of being able to extract detector efficiencies directly from the data.

For each π^0 angular bin we have carried out between 8 and 12 different analyses. A sample of five of these using different requirements on (a) the proton recoil position within R_{wc} in the TOF wire chambers, and on (b) the γ-ray energy measured in the 48 cm diameter NaI, as compared with the maximum available from π^0 decay, E_γ/E_{max}, are plotted in Fig. 21. Here, E_{max} is calculated from the tagged beam energy and the proton recoil angle. Data are shown for 100° from the *group I* set (bottom panel), and for 130° from the *group II* data set (top panel). Upon inspection one notices shifts in these different analyses that are significantly beyond statistical fluctuations. For example, the $[R_{wc}<11.4$ cm; $E_\gamma/E_{max}>0.70]$ points denoted by crosses are the highest at most of the energies in the lower panel, while the $[R_{wc}<6.0$ cm; $E_\gamma/E_{max}>0.85]$ triangles tend to be the highest for most energies in the top panel.

The variations between data *groups* for the *full acceptance* analyses are small. This is shown in Fig. 22 where results from the $[R_{wc}<11.4$ cm; $E_\gamma>100$ MeV$]$ analyses are plotted for overlapping angles, 100° from the *group I and II* data and 70° from the *group I and III* data sets.

There are no obvious correlations between the different analysis requirements and angle (i.e., no one set of R_{wc}; $E_\gamma/E_{max}]$ results is always high, etc.). The recoil protons associated with the 100° *group I* data of Fig. 21 are approximately centered in the TOF wire chambers, while those from the 130° *group II* data are concentrated to one side of the full acceptance. Although we have looked for trends associated with such variations in wire chamber position, we have found none. The shifts evident in Fig. 21 simply reflect systematic differences between the actual and simulated geometries of the γ-ray and recoil-proton detectors. Such differences are present in every experiment. The current one is unique in its ability to *measure* such effects.

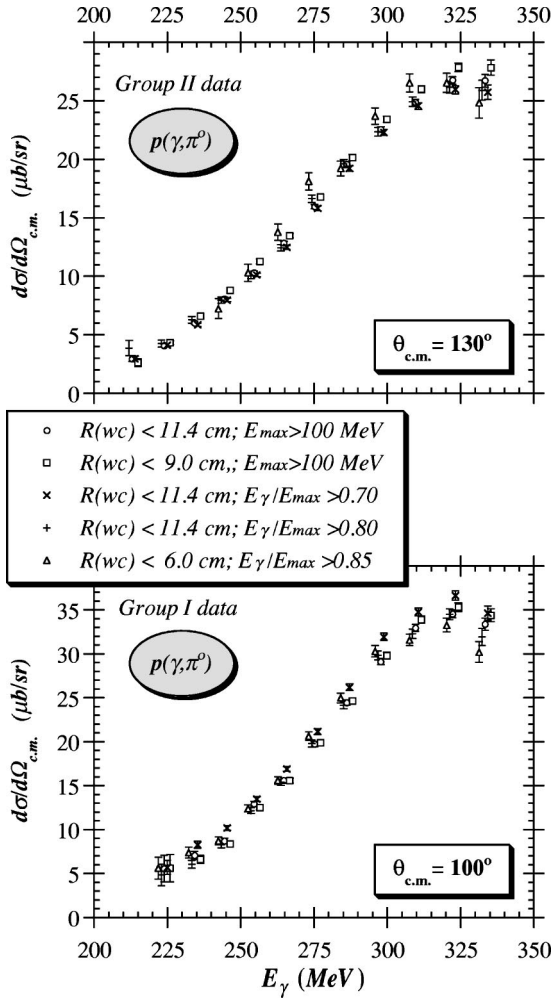

FIG. 21. Cross sections for $p(\gamma,\pi^0)$ for 130° from the *group II* data (top), and for 100° from the *group I* measurements (bottom) using different requirements on the proton recoil position within a circle of radius *R(wc)* in the TOF wire chambers, and on the γ-ray energy measured in the 48 cm diameter NaI as compared with the maximum available from π^0 decay, E_γ/E_{max} (see legend).

For each energy and each angle we have taken the mean of the results from the different data groups and the different $[R_{wc}$; $E_\gamma/E_{max}]$ analyses as representing the *net* value for the cross section, and we have taken the standard deviation of these different analyses as representing the systematic error on the acceptance. The latter has then been combined in quadrature with the statistical error from the *full acceptance* (which includes the propagated statistical errors on the efficiency measurements, as well as the Monte Carlo statistics for the secondary reaction correction and the solid angle determination) to yield a net *measurement* uncertainty for the $p(\gamma,\pi^0)$ cross sections. The resulting values are shown in Fig. 23 for two beam energies, 323 MeV and 265 MeV, along with the corresponding results from the *full acceptance*

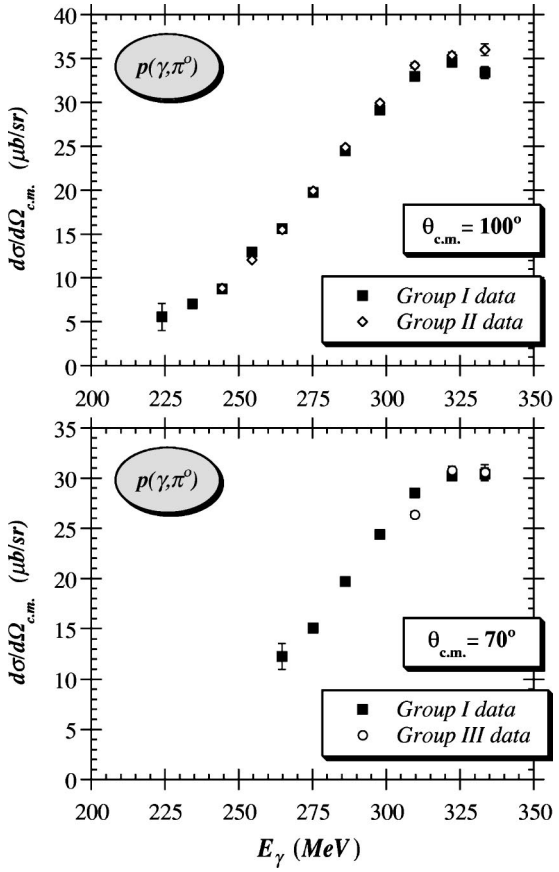

FIG. 22. Cross sections for $p(\gamma,\pi^0)$ from the different data *groups* at overlapping angles: 100° from *group I* and *group II* (top), and 70° from *group I* and *group III* (bottom). Each of these used the *full acceptance* analysis requirements, $[R(wc)<11.4$ cm; $E_\gamma>100$ MeV].

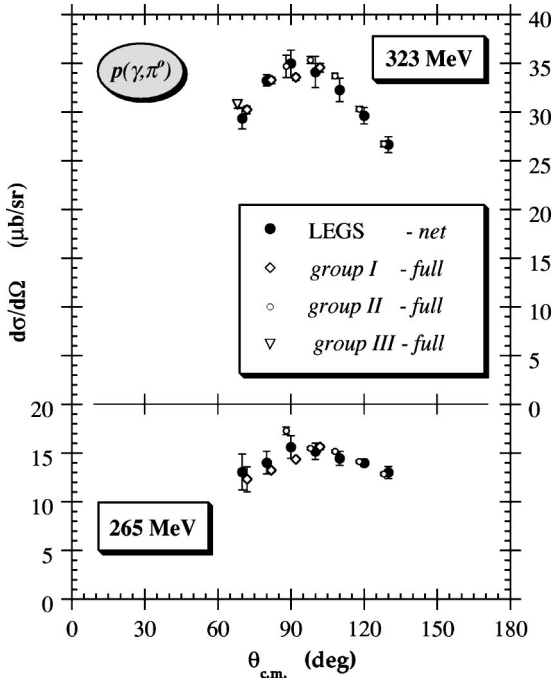

FIG. 23. Final *net* $p(\gamma,\pi^0)$ cross sections at 323 MeV and 265 MeV, along with their *measurement* uncertainties (see text). The corresponding *full acceptance* analyses, $[R(wc)<11.4$ cm; $E_\gamma>100$ MeV], are also shown with their statistical errors.

analyses of the three data *groups*.

5. A two-body consistency test for $p(\gamma,\pi^0)$ cross sections

The accuracy of the π^0 cross sections can be tested by comparing the final mean results with cross sections from an analysis in which restrictions are placed on the data that kinematically confine the high-energy photon from π^0 decay within the lead collimator of the 48 cm diameter NaI. This *two-body-like* analysis removes any dependence on the geometry of the NaI arm and reduces the computation of the solid angle to the angular range selected by the TOF wire chambers, as is the case in Compton scattering.

The distribution of high-energy photons from $p(\gamma,\pi^0 p)$ on a plane containing the lead collimator in front of the 48 cm diameter NaI is shown in Fig. 24, calculated for 300 MeV incident energy. The top panel corresponds to the *full acceptance* analysis in which events in the TOF wire chamber are limited to a radius of 11.4 cm and a minimum energy of 100 MeV is required in the NaI. Approximately half of the photons are outside the lead aperture, indicated by the circle. The highest energy photons are emitted along the π^0 momentum vector, opposite the recoil momentum in the c.m. frame. By restricting the proton recoils to a small angular range (within the central 6 cm radius of the wire chambers and within a central 40 cm radius as determined from bar_x and bar_y), and by limiting the γ rays to the high end of their spectrum (with greater than 85% of the maximum photon energy available from π^0 production), the distribution of photons collapses within the lead collimator, as shown in the lower panel of Fig. 24. With these $[R_{wc}<6.0$ cm; $E_\gamma/E_{max}>0.85]$ kinematic constraints, the solid angle is entirely determined by the TOF arm.

The $p(\gamma,\pi^0)$ cross sections from the *quasi-two-body* acceptance (bottom panel of Fig. 24), are compared with the mean results in Fig. 25 for two different beam energies. The agreement here, as at other energies, is very good. The high-energy requirement on the γ-ray energy is a crucial component of this *quasi-two-body* acceptance test. In fact, the test of Fig. 25 is only as good as the energy calibration of the NaI. As seen in Fig. 16 to Fig. 18, this is under very good control.

In summary, the determination of the NaI energy calibration and response function directly from the π^0 data itself, and the *quasi-two-body* acceptance analysis, confirm the accuracy of the calculation of the effective geometrical acceptance for the $p(\gamma,\pi^0 p)$ reaction. For Compton scattering, the geometrical solid angle is entirely determined by the proton recoil angles measured in the TOF wire chambers and, thus, is of high accuracy.

6. Corrections to $p(\gamma,\gamma p)$ for NaI tails below ΔE_0 threshold

There is a final component of the Monte Carlo correction that is unique to the Compton analysis. For the extraction of the Compton events described in Sec. IV A, a requirement is placed on the difference between the observed γ-ray energies and those predicted from the recoil angle measured in the

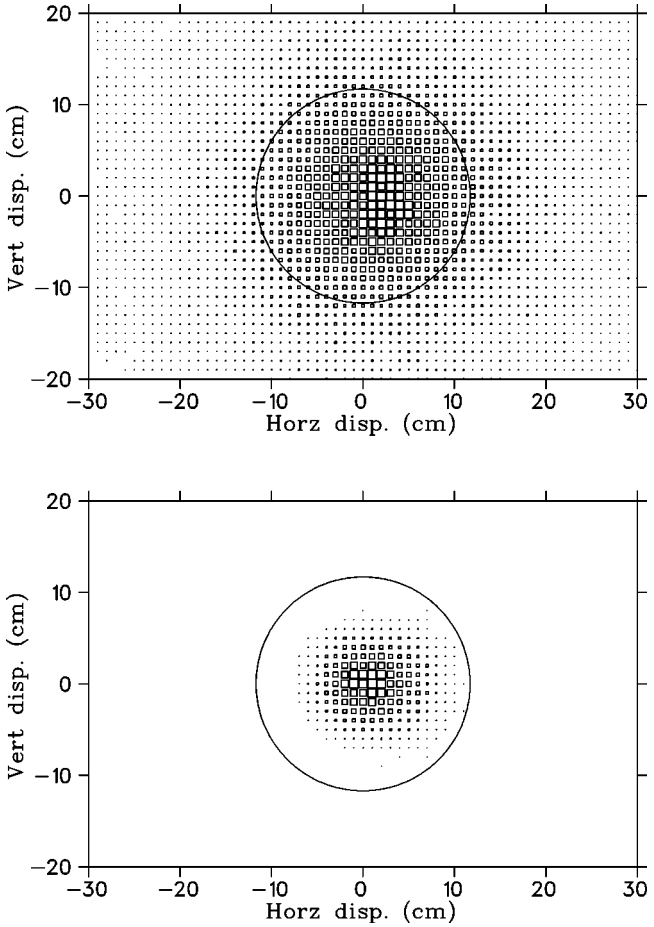

FIG. 24. Scatter-plot of the position of high-energy π^0-decay photons from $p(\gamma,\pi^0 p)$, calculated for $E_{beam}=300$ MeV, on a plane containing the lead collimator in front of the 48 cm diameter NaI. The lead aperture is indicated by the circle. The top panel shows the distribution of photons corresponding to the *full acceptance* requirements used with the TOF and NaI detectors. The *two-body-like* distribution in the bottom panel results from kinematic restrictions on the proton-recoil angle and the NaI energy (see Sec. IV D 5).

TOF wire chambers and from the tagged beam energy (Fig. 8). This requirement is $|\Delta E_0^{NaI}|\leqslant 20$, 20, and 30 MeV for the *group II, I, and III* data sets, respectively. This cut reduces the π^0 background in the rotated-coordinate spectra (Fig. 9), but limits events in the tail of the NaI response. A correction is made with GEANT for γ rays that produce signals below ΔE_0^{NaI} . The percentage of Compton events passing this requirement is shown in Fig. 26 for $\pm 5°$ angular bins centered at 125°, 90°, and 65° from the *group II, I, and III* data sets, respectively. The increase between the 125° *(group II)* and 90° *(group I)* points is due to the increasing recoil angle (Table I) and the associated decrease in the path length and multiple scattering through the liquid hydrogen. This in turn decreases the broadening in the expected Compton energy calculated from the wire chamber angles. The same trend is followed for the 65° *(group III)* points, which are further increased by the larger $|\Delta E_0^{NaI}|\leqslant 30$ MeV requirement that is

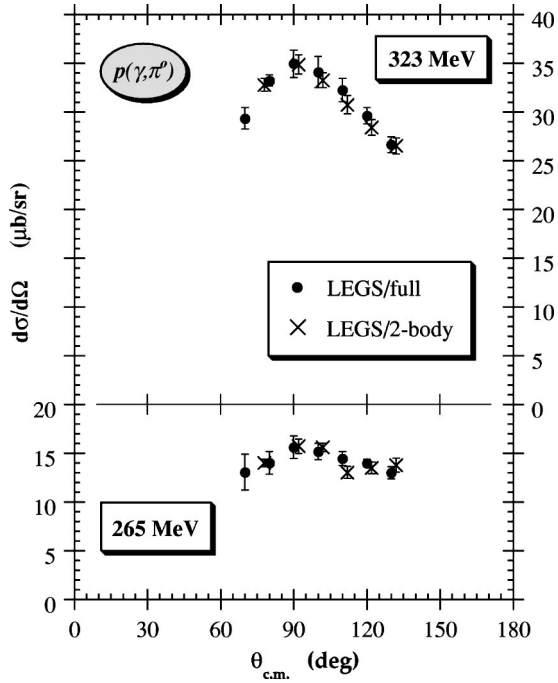

FIG. 25. Final net angular distributions for $p(\gamma,\pi^0 p)$ are shown here as solid circles. The crosses result from kinematically restricting the proton recoil and the highest-energy π^0-decay photon to a *quasi-two-body* distribution, as in the bottom panel of Fig. 24.

used with these data. The excellent agreement between the calculated NaI line shapes and those observed without imposing the ΔE_0^{NaI} requirement, as in Fig. 17, verifies the accuracy of these calculations.

V. ANALYSIS OF π^+ PRODUCTION

The $p(\gamma,\pi^+)n$ reaction was measured during the third group of data runs (Table I) using the six NaI detectors of Fig. 5. Each NaI was preceded with a plastic scintillator for

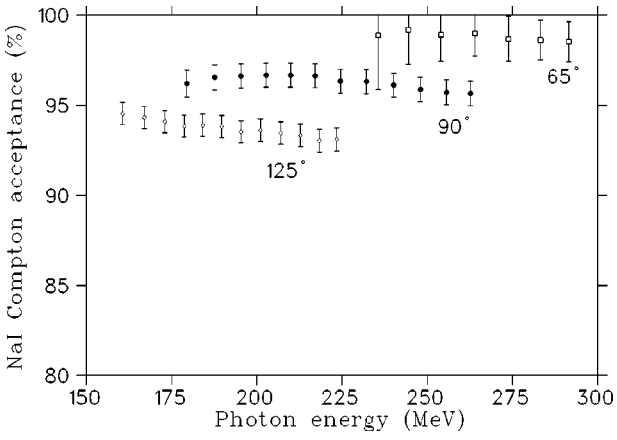

FIG. 26. Fraction of Compton events passing the $|\Delta E_0^{NaI}|\leqslant 20$, 20, and 30 MeV requirements on the difference between the predicted and observed γ-ray energies for $\pm 5°$ bins centered at 125°, 90°, and 65° from the *group II, I,* and *III* data sets, respectively. These GEANT predictions are plotted against the γ-ray energy in the 48 cm diameter NaI (see Sec. IV D 6).

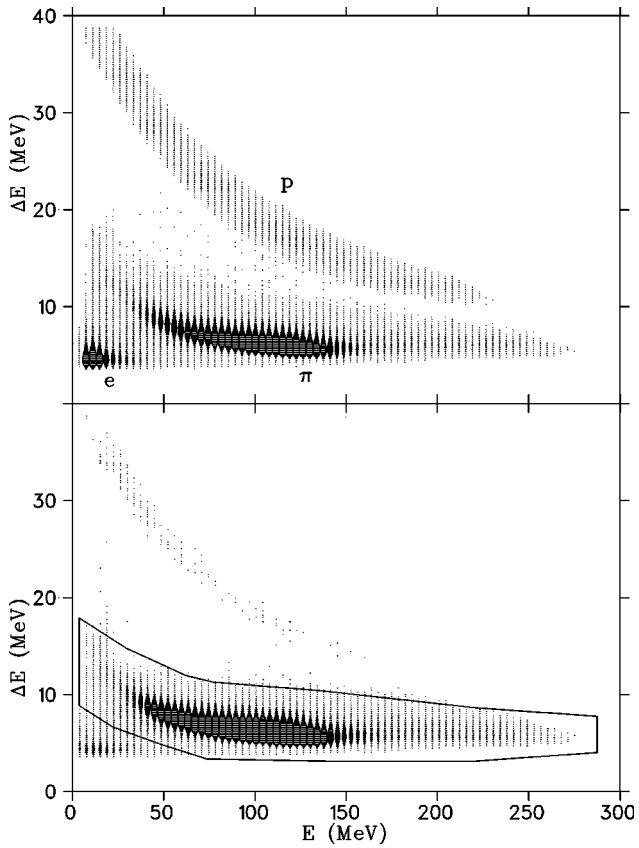

FIG. 27. Energy deposition in the 48 cm diameter NaI plotted against the energy loss in its preceding 2.5 cm plastic scintillator, top panel. Particle types are localized in bands as indicated. The bottom panel shows the effect of restricting the origin of events to the central region of the target (the hatched area in the wire chamber projection of Fig. 28).

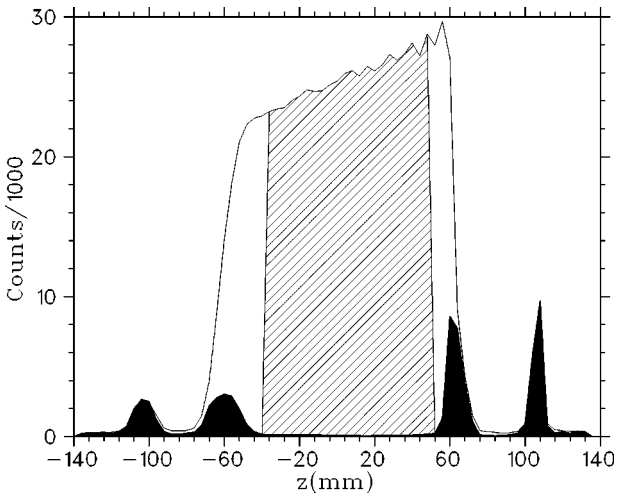

FIG. 28. Projection of charged particle tracks onto the beam axis from the wire chambers that were used in front of the 48 cm diameter NaI during the third group of data runs. The superimposed spectrum shaded in black was obtained with the target cell filled with hydrogen gas (normalized to the same beam flux as the full liquid target spectrum). The hatched area indicates the *central* region used during analysis to avoid reactions from the ends of the target cell (at ± 65 mm) and from the windows of the vacuum chamber (at ± 105 mm).

energy loss measurement and charged pions were identified in ΔE vs E spectra. As discussed in Sec. III, wire chambers were used with the detectors at 55°, 90°, and 140° to define solid angles while collimators were used with the crystals at 14° and 170° lab. The analysis of data from the 48 cm diameter NaI at 55° is detailed in Sec. V A below. This analysis is typical of all of the other detectors, except the most forward NaI at 14°. The reduction of the data from the latter is treated separately in Sec. V B below.

A. (γ, π^+) extraction at 55° lab

A typical particle identification spectrum obtained in the 55° NaI and its preceding plastic is shown in the top panel of Fig. 27. Protons, pions, and atomic electrons are resolved in separate bands. (This separation increases in the other detectors at larger angles as the energy of the particles decreases.)

The four wire chambers in front of the 55° detector (three *x chambers* measuring horizontal position and one *y chamber* measuring vertical position) can be used to project particle tracks back to the beam axis and form an image of their source. The result for the target filled with liquid hydrogen is shown in Fig. 28 as the solid curve. The spectrum shaded in black was obtained with the target filled with one atmosphere of hydrogen gas and is normalized to the same beam flux as the target-full data. The contributions from reactions in the mylar of the target cell entrance and exit windows and in the vacuum chamber windows result in the peaks at ± 65 mm and ± 105 mm, respectively. (These backgrounds are more prominent here than in the recoil-proton spectra of Fig. 7 which require a more-exclusive γ + proton trigger.)

Background contributions can be eliminated in one of two ways: either by subtracting normalized spectra obtained with the target filled with hydrogen gas, or by restricting to events that come from the *central* region of the target, as indicated by the hatched area in Fig. 28. Imposing this latter requirement results in the particle identification spectrum plotted in the bottom panel of Fig. 27. Electrons are dramatically reduced, since their production is now restricted to the low-Z low-density hydrogen, and protons are almost eliminated. The few protons that survive this cut are recoils from π^0 production which at these angles are low in energy and mostly stop in the plastic ΔE scintillator. Pions can be extracted with a polygonal cut such as shown in the bottom panel of Fig. 27. Although this central target cut provides the cleanest particle identification, it requires accurate calibrations which must be relied upon to fix the target length. (A cross check of the calibration is provided by the positions of the peaks in the target-empty spectra of Fig. 28.) A compromise that reduces electron contamination without requiring the wire chamber reconstruction to fix the target length is to place cuts at ± 80 mm in the spectra of Fig. 28, and use normalized empty-target spectra to subtract out the remaining effects of the target cell walls. This method has a slightly smaller systematic uncertainty and has been used throughout for π^+ analysis. Nonetheless, cross sections were also com-

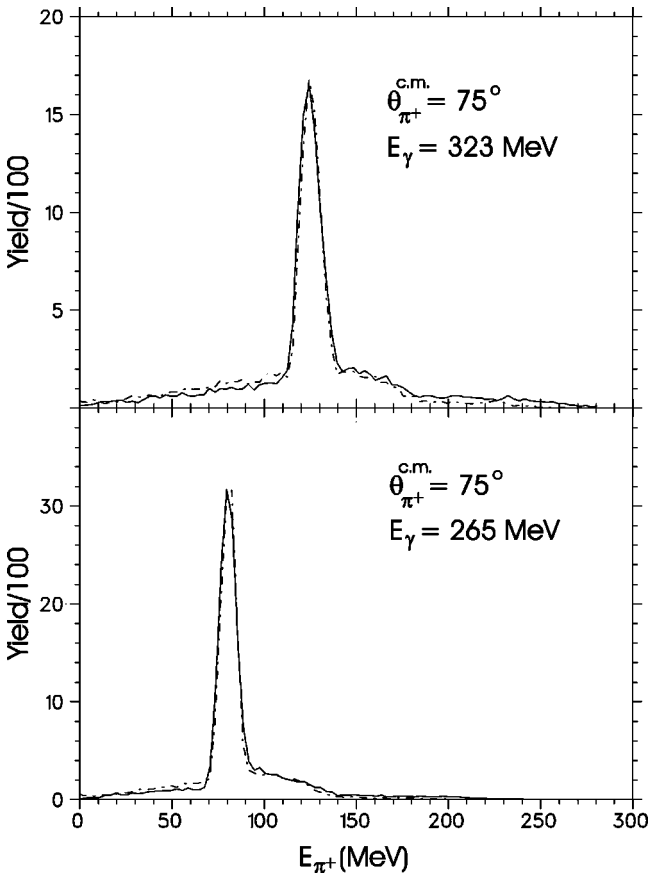

FIG. 29. Charged pion spectra (solid curves) for events lying within the polygonal band in the bottom panel of Fig. 27 and in the hatched area of Fig. 28 for $75° \pm 5°$ c.m. The dash-dot lines are the results of simulations using GEANT and GCALOR [51,52].

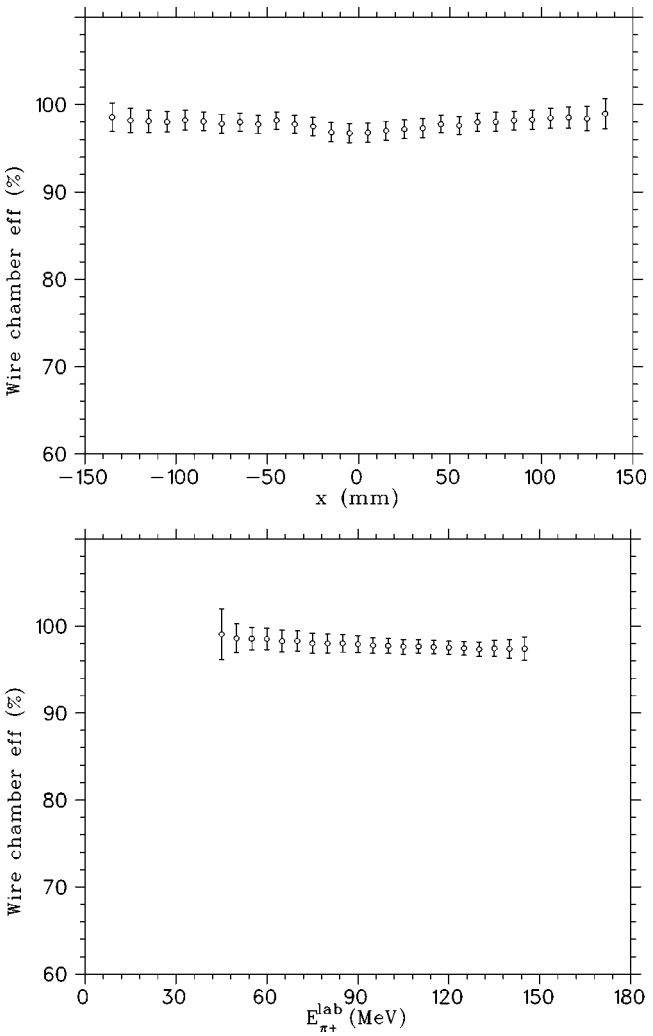

FIG. 30. Efficiencies of the stack of *x* drift chambers, preceding the 55° NaI during the *group III* data, for π^+ as a function of distance across the chamber (top) and as a function of pion energy (bottom panel).

puted using the central target cut of Fig. 28, and the root-mean-square (rms) deviation between the results of the two analysis methods was 1.4%.

Pion spectra are shown for $75° \pm 5°$ c.m. and two different beam energies in Fig. 29 (solid curves). The beam energy and the pion angle completely specify the reaction so that events in which the full ionization energy is deposited in the NaI appear in well defined peaks. The tails below these kinematic peaks are due to reactions in the material of the detector. Those above the peaks result from an increase in the deposited energy from the $\pi \rightarrow \mu \rightarrow e$ decay. The π^+ to $\mu^+ \nu$ decay occurs in 26 ns and imparts up to 4.1 MeV to the muon, which then decays to $e^+ \nu \overline{\nu}$ in 2.2×10^{-6} s. For the latter, the electron can carry up to 52.8 MeV of energy. The fraction of events for which decay energy is added to the pion signal depends upon the angle of the emitted neutrinos and upon the gating time used with the readout electronics. These factors have been incorporated into GEANT Monte Carlo simulations, using GCALOR to account for nuclear reactions in the detector material [51,52]. The resulting calculations are shown as the dash-dot curves in Fig. 29 and are in excellent agreement with the data. Pion production accounts for the entire spectra of Fig. 29, and their full integrated yields were used in determining cross sections.

The computation of cross sections requires the efficiencies of the wire chambers used in placing target cuts and these are measured in much the same way as described in Sec. IV B2. Geometry guarantees that a pion identified in the NaI has to have passed through the complete stack of drift chambers. For example, the efficiency of one of the *x* chamber is the fraction of detected tagged pions that are tracked in the other two chambers,

$$\varepsilon_1^{wc_x} = \frac{\{N_{1-hit}^{tag} \cap N_{ID}^{NaI} \cap N_2^{wc_x} \cap N_3^{wc_x}\} \cap N_1^{wc_x}}{\{N_{1-hit}^{tag} \cap N_{ID}^{NaI} \cap N_2^{wc_x} \cap N_3^{wc_x}\}}. \quad (9a)$$

The analysis algorithm required a hit in at least two of the *x* chambers, so that the net efficiency is

$$wc_x^{55°}\text{eff} = \varepsilon_1^{wc_x}\varepsilon_2^{wc_x} + \varepsilon_1^{wc_x}\varepsilon_3^{wc_x} + \varepsilon_2^{wc_x}\varepsilon_3^{wc_x} - 2\varepsilon_1^{wc_x}\varepsilon_2^{wc_x}\varepsilon_3^{wc_x}. \quad (9b)$$

This is plotted in Fig. 30 as a function of horizontal position (top panel) and pion energy (bottom panel). (The slight dip

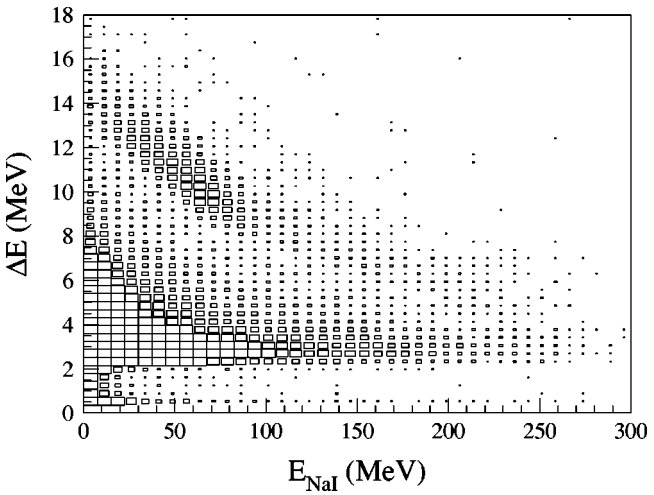

FIG. 31. Energy deposition in the 24 cm diameter NaI plotted against the energy loss in its preceding 1 cm plastic scintillator. The upper band is due to protons while the lower contains both electrons and pions.

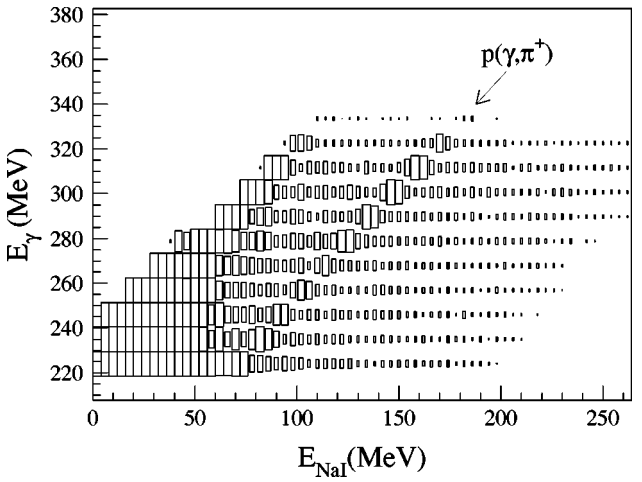

FIG. 32. The correlation of energy deposition in the 14° NaI vs the tagged beam energy for those events in the lower $e+\pi$ band of Fig. 31. The kinematic band of pions from the two-body $p(\gamma,\pi^+)n$ reaction is clearly visible.

seen in the top panel near $x=0$ is due to a dead wire in one of the chambers.) The efficiency of the *y chamber* is constructed in a similar way.

Monte Carlo simulations were used to correct for events lost due to secondary reactions within the target, and to calculate the effective target length from the extended target as well as the geometrical solid angle subtended by moderately large angular bins. Here, we followed the same procedures discussed in Sec. IV D, including the deconvolution process used to generate the *point* cross sections that would be obtained with a pencil beam on a point target as seen by a point detector.

The above analysis procedures were repeated with the 90° and 140° detectors. Very similar spectra and efficiencies were obtained, the only difference being increased separation between particle bands in plots such as those of Fig. 27. Since the two 170° detectors, positioned symmetrically above and below the beam line, were not equipped with wire chambers, only the target-empty subtraction method was used to eliminate their contributions from the mylar target and vacuum windows.

B. (γ,π^+) extraction at 14° lab

A typical plastic-ΔE vs NaI-E plot observed in the 14° detector is shown in Fig. 31. The upper band is due to protons and is resolved. However, at this forward angle both atomic electrons and pions are considerably higher in energy than at other angles, and as a result the two merge to form the lower band in the figure. Furthermore, as mentioned earlier, the small angle relative to the beam precluded the use of wire chambers to resolve the dominant electron sources from the target cell and vacuum chamber windows. For these reasons, the analysis techniques of Sec. V A are not suitable.

Despite the presence of electrons, the angular acceptance of this detector and the tagged beam energy are sufficient to determine the pion energy from the $p(\gamma,\pi^+)n$ reaction, and as a result the full pion ionization-energy peak appears as a narrow feature above a smoothly varying background. This is shown in Fig. 32 where the energy deposited in the NaI is plotted against the tagged beam energy. The kinematic band from the two-body $p(\gamma,\pi^+)n$ process is resolved for nearly the full range of tagged beam energies. (Software cuts limit the left-hand side of this plot.)

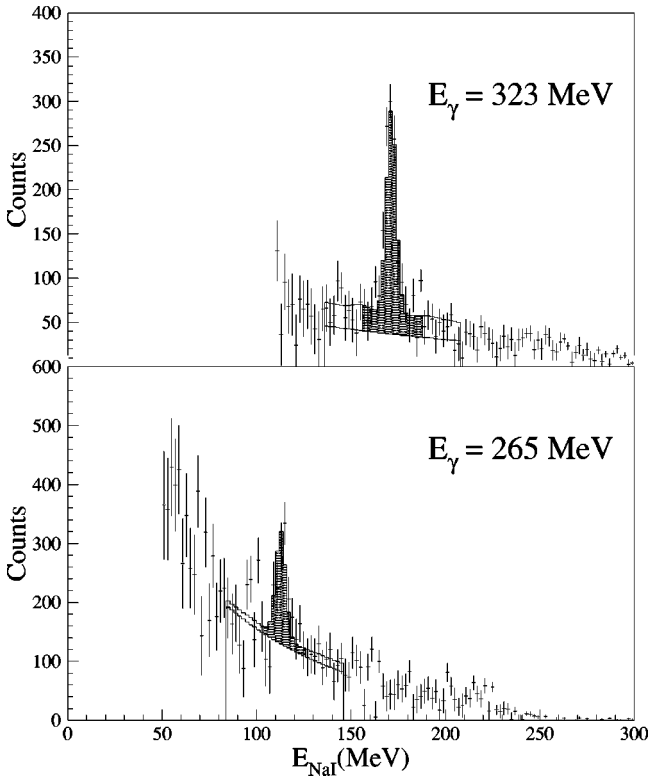

FIG. 33. Energy deposition in the 14° NaI at two of the incident beam energies of Fig. 32. The shaded peaks denote the contributions from the absorption of the full ionization energy of pions from $p(\gamma,\pi^+)n$. The lower lines below the peaks indicate the fitted electron background.

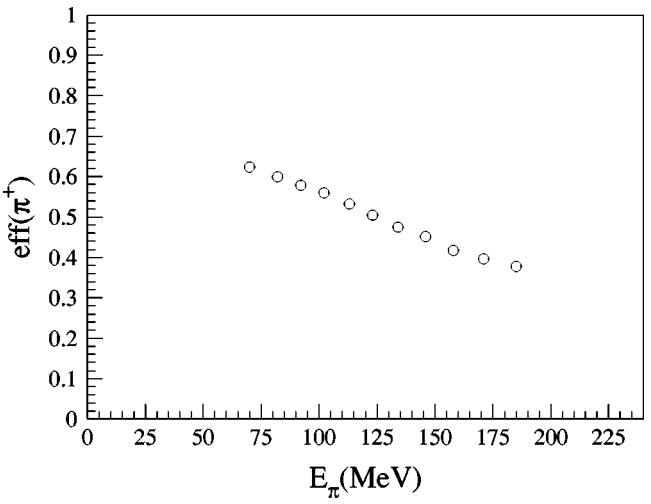

FIG. 34. Pion efficiency for the 14° detector, using only the full kinetic energy peaks as in the shaded areas of Fig. 33. These were calculated with GEANT, using GCALOR to account for reactions [51,52].

Accidental-event subtracted NaI spectra for two of the beam energies of Fig. 32 are shown in Fig. 33. These spectra were fit to a GEANT-generated pion line shape and an exponential background (solid lines). The peaks are associated with pions that deposit their full kinetic energy in the detector. To minimize the systematic error associated with possible uncertainties in the energy dependence of the background, only the region near the kinematic peaks have been used to extract π^+ cross sections. These are the shaded areas in Fig. 33. (Fits with a linear electron background have also been carried out. These produce statistically equivalent results.)

The efficiency of using only the π^+ full kinetic energy peak can be determined with GEANT, and the results for this detector are shown in Fig. 34. The decrease with energy seen here is caused by an increase in the nuclear reactions within the detector material. On average, the π^+ response is outside the shaded areas of Fig. 33 about one-half of the time. As a result, the systematic error in the resulting cross section is

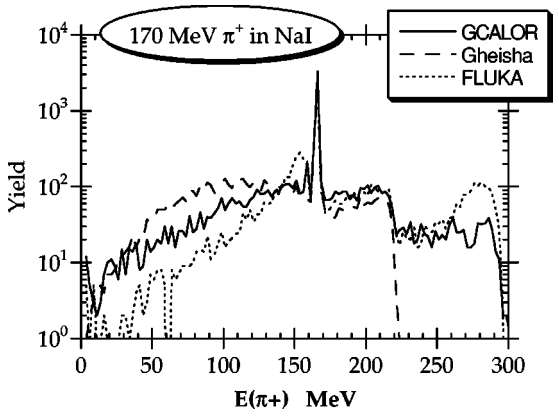

FIG. 35. The response of NaI to 170 MeV π^+, as simulated with GEANT using three different hadron packages to model reactions in the material of the detector [51,52,56].

critically dependent upon the accuracy of the hadron package used with GEANT to simulate reactions. This is illustrated in Fig. 35 where we plot the predicted response of NaI to 170 MeV π^+ using GCALOR [52] and two standard packages, Gheisha [56] and FLUKA [51]. The peak to total-area ratios can differ by more than 5% depending upon which of these is used. Fortunately, the full π^+ response could be measured, free of electron contamination and with moderately high resolution, in the NaI detectors at other angles (as in Fig. 29). Simulations with GCALOR provide a consistently excellent description of the observed line shapes while those using Gheisha or FLUKA are noticeably poorer. For this reason, GCALOR has been used throughout the simulations reported here.

The solid angle for this detector was determined by a pair of plastic scintillators in the shape of arcs with fixed azimuthal acceptance. This shape was chosen to minimize uncertainties in the geometrical asymmetry correction, P^G in Eq. (8), which otherwise could be significant at extreme forward and backward angles. (For the same reason, similar arced-shape apertures were used with the 170° detectors.) A coincidence between the two 14° scintillators eliminated false events triggered by Cherenkov radiation in the nonoverlapping light guides. This pair was located after a larger plastic scintillator used for the ΔE measurement of Fig. 31. Because of this slightly unusual geometry, the efficiency of the scintillator pair was measured with a set of wire chambers that were positioned in front of the pair for part of the running period. This efficiency is just the fraction of events in the pair of arced scintillators that trigger the wire chambers, pass the particle-ID cuts, and are accompanied by a valid tag,

$$\text{pair}^{14^\circ}\text{eff} = \frac{\{N^{tag} \cap N_{ID}^{NaI} \cap N^{wc}\} \cap N^{pair}}{\{N^{tag} \cap N_{ID}^{NaI} \cap N^{wc}\}}. \qquad (10)$$

This is shown as a function of position in the plane of the scintillator pair in the top panel of Fig. 36. To avoid potential ambiguities from electrons, which undergo appreciable multiple scattering, this efficiency map was made using the proton band in Fig. 31. The geometrical shape of the scintillator pair (solid curve in the top panel) is reproduced. A slice through the middle of this efficiency map is shown in the bottom panel.

The above analysis was applied to target-empty spectra. The results were subtracted to eliminate the contributions from particles produced in the Mylar target and vacuum chamber windows.

The protons in the upper band of Fig. 31 were mostly recoils from π^0 production at 150° c.m. Coincidentally, the angular settings for the 14° NaI and the 48 cm diameter NaI, which was positioned on the other side of the beam line at 55° during the *group III* runs, corresponded to the conjugate angles for $\gamma p \rightarrow \pi^0 p$. When a π^0 decay photon was emitted along the pion momentum vector its energy was sufficient to trigger the large NaI. Events in this 55° detector had a higher priority in the data acquisition and, unfortunately, the signals from the 14° detector were not simultaneously recorded.

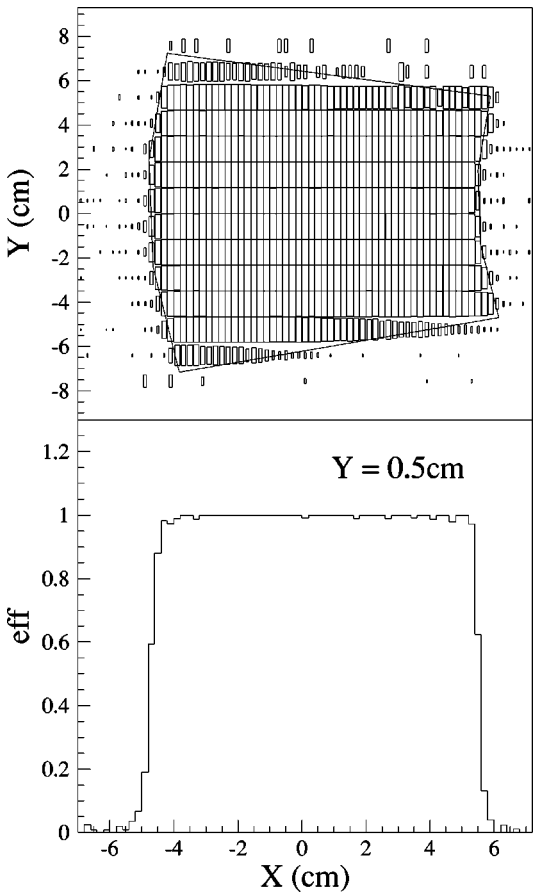

FIG. 36. Efficiency of the plastic scintillator pair used to define the solid angle of the 14° detector. A mapping in the plane of the scintillator is shown in the top panel, and a cut at $Y=0.5$ cm is shown at the bottom.

Corrections for such lost recoil protons were attempted but found to be too uncertain for cross section determinations. For this reason the proton recoils measured at 14° were used only to construct π^0 asymmetry ratios.

C. Monte Carlo corrections for (γ,π^+)

The extraction of π^+-production cross sections relied upon Monte Carlo simulations to determine the π^+-detection efficiency. This introduced only small uncertainties when essentially the full π^+ response could be used, as in Fig. 29, but was more critical for the 14° detector for which only the full-kinetic-energy peak could be used (Fig. 33). The cross sections were evaluated for each data point using the three hadron reaction packages, GCALOR [52], Gheisha [56], and FLUKA [51]. Tests included variations of the target thickness and of the materials of the hermetic NaI cans. The uncertainties associated with the π^+ response were taken as half the maximum variation between the results obtained with GCALOR and either Gheisha or FLUKA.

Uncertainties in detector alignment and beam position were also evaluated for each data point by varying the geometry in Monte Carlo. The largest variations occurred for the 14° and 170° detectors since at these extreme angles a change in the central angle value has some effect on the lab to c.m. Jacobian.

The above uncertainties are *systematic* in nature, but are dependent upon π^+ energy and angle, and for that reason have been evaluated separately for each datum. These were combined in quadrature with the *statistical* errors to yield a net *measurement* uncertainty for each point.

VI. FINAL RESULTS

Final c.m. cross sections for the $p(\gamma,\gamma)$, $p(\gamma,\pi^0)$, and $p(\gamma,\pi^+)$ reactions from this experiment are listed in Tables II, IV, and VI, respectively. Linearly polarized beam asymmetries for $p(\vec{\gamma},\gamma)$, $p(\vec{\gamma},\pi^0)$, and $p(\vec{\gamma},\pi^+)$ and are listed in Tables III, V, and VII, respectively. All finite size effects have been deconvoluted using the procedure outlined in Sec. IV D 3.

Portions of these results have appeared in Refs. [37,21,9,57,58]. (The 90° c.m. Compton data reported in [37] were extracted from an analysis that used a larger angu-

TABLE II. *Point* cross sections (Sec. IV D 3), $d\sigma/d\Omega_{\rm c.m.}$ in nb/sr, for $p(\gamma,\gamma)$ in the c.m. frame as a function of incident lab photon energy and c.m. scattering angle. The *net measurement errors* listed here are the quadrature sum of *statistical* and *point-specific systematic* uncertainties (Sec. VI). In addition to these, there is an additional systematic scale uncertainty of 2% (Sec. VI A).

E_γ (MeV)	65°	±err	75°	±err	90°	±err	105°	±err	115°	±err	125°	±err	135°	±err
333.8	272.1	25.9	197.2	19.5	216.4	18.2	197.8	21.0	227.8	23.6	227.5	22.9		
323.8	272.0	10.8	224.0	8.0	216.5	7.5	214.4	7.5	247.2	9.1	251.6	9.6	268.9	12.0
310.1	253.4	7.3	203.7	4.9	206.5	4.8	210.9	4.7	243.5	5.8	242.1	6.0	253.0	7.6
298.2	211.0	6.8	186.0	4.5	190.4	4.3	200.2	4.4	205.3	5.2	222.1	5.7	251.1	7.4
286.5	171.8	7.3	156.3	4.5	160.8	4.4	175.4	4.5	183.3	5.4	202.7	6.0	234.0	8.1
275.6	134.8	8.1	125.8	4.6	134.8	4.6	153.1	4.8	164.6	5.8	171.1	6.5	212.9	8.8
265.1	119.4	10.2	104.1	5.0	108.5	5.0	121.1	4.9	138.6	6.1	155.6	6.9	178.9	9.2
254.1	99.8	13.8	91.0	5.8	81.4	5.5	98.0	5.2	114.0	6.1	131.2	6.8	148.8	9.1
244.8			76.4	7.1	85.6	6.6	78.7	5.1	93.7	5.9	122.3	6.9	129.7	9.0
234.7			60.4	9.8	59.0	6.5	75.4	5.2	81.8	5.7	86.8	7.4	106.5	8.3
224.3					53.9	6.6	68.4	5.0	66.6	5.4	84.0	6.5	78.2	7.6
213.1					48.2	6.6	60.6	6.2	67.5	8.5	57.1	5.0	62.7	6.9

TABLE III. *Point* beam asymmetries (Sec. IV D 3), Σ, for $p(\vec{\gamma},\gamma)$ as a function of incident lab photon energy and c.m. scattering angle. The *net measurement errors* listed here are the quadrature sum of statistical and *point-specific systematic* uncertainties (Sec. VI). There are no additional systematic polarization scale uncertainties.

E_γ (MeV)	65°	±err	75°	±err	90°	±err	105°	±err	115°	±err	125°	±err	135°	±err
333.8	0.355	0.093	0.435	0.103	0.506	0.080	0.304	0.100	0.210	0.112	0.257	0.106	0.353	0.123
323.8	0.212	0.041	0.358	0.037	0.394	0.034	0.385	0.034	0.277	0.040	0.227	0.039	0.183	0.043
310.1	0.249	0.028	0.287	0.025	0.374	0.022	0.332	0.022	0.291	0.025	0.210	0.025	0.145	0.028
298.2	0.197	0.032	0.229	0.025	0.315	0.022	0.297	0.022	0.224	0.026	0.229	0.026	0.061	0.028
286.5	0.153	0.042	0.248	0.030	0.245	0.028	0.179	0.027	0.182	0.030	0.119	0.030	0.046	0.033
275.6	0.149	0.058	0.152	0.037	0.241	0.033	0.198	0.031	0.110	0.034	0.095	0.036	0.046	0.037
265.1	0.086	0.078	0.155	0.045	0.140	0.039	0.110	0.037	0.061	0.040	0.077	0.040	0.023	0.043
254.1	−0.112	0.124	0.034	0.062	0.105	0.047	0.134	0.043	0.093	0.049	−0.023	0.048	0.023	0.054
244.8			0.018	0.081	0.032	0.056	0.100	0.051	0.009	0.057	0.067	0.055	−0.126	0.061
234.7			0.078	0.138	0.064	0.071	−0.077	0.058	0.112	0.064	−0.037	0.065	0.055	0.070
224.3			0.070	0.231	−0.052	0.086	0.036	0.068	0.077	0.075	0.067	0.074	−0.092	0.082
213.1					−0.061	0.109	−0.079	0.084	−0.075	0.084	−0.155	0.084	−0.074	0.100

lar acceptance than that of the present work to minimize statistical errors. Those results should not be combined with this work, since that would involve double counting.)

A. *Measurement* and *systematic scale* uncertainties

As discussed in the previous sections, the large overdetermination of kinematics in this experiment has allowed us to measure detector efficiencies directly from the data itself. In addition, for the case of π^0 production where the effective solid angle was necessarily a convolution of the acceptances of two detector arms, the additional *systematic* uncertainties in this convolution were determined in the analyses described in Sec. IV D 4. As a result, there is a class of *point-specific systematic* uncertainties for each datum which include the propagated errors from efficiency measurements, the variations in acceptance, and, for π^+ production, possible variations in detection efficiency. These have been evaluated for each data point and combined in quadrature with statistical errors to yield the *net measurement uncertainties* listed in the data tables.

In addition to the *point-specific* systematic errors, there are also *common* systematic uncertainties that scale the entire set of cross sections. These include target density variations due to temperature fluctuations, heat loading and bubbles, which we have estimated from multiple temperature measurements as 0.8%; time variations in the flux normalization, which we have sampled through 54 independent measurements taken throughout the running of this experiment (Sect. II), and taken their standard deviation (1%) as a measurement of the associated systematic error; possible rate-dependent uncertainties (1%) in the efficiency of the flux monitor (Sec. II); uncertainties in the target length (0.2%), as determined from x-ray photographs of a full target taken under operating conditions; uncertainties in the geometric solid angles due to possible variations in wire-chamber calibra-

TABLE IV. *Point* cross sections (Sec. IV D 3), $d\sigma/d\Omega_{\text{c.m.}}$ in μb/sr, for $p(\gamma,\pi^0)$ in the c.m. frame as a function of incident lab photon energy and c.m. reaction angle. The *net measurement errors* listed here are the quadrature sum of *statistical* and *point-specific systematic* uncertainties (Sec. VI). In addition to these, there is an additional systematic scale uncertainty of 2% (Sec. VI A).

E_γ (MeV)	70°	±err	80°	±err	90°	±err	100°	±err	110°	±err	120°	±err	130°	±err
333.5	29.00	1.61	31.84	1.57	33.88	1.52	33.43	2.01	32.61	1.26	29.50	0.90	26.17	1.26
322.2	29.34	1.10	33.20	0.58	34.94	1.40	34.08	1.60	32.24	1.19	29.61	0.83	26.62	0.81
309.6	27.36	0.84	30.82	0.91	33.56	1.38	32.42	1.58	30.82	0.84	29.08	0.45	25.35	0.77
297.7	23.52	1.35	27.07	0.82	29.14	1.62	29.21	1.26	27.54	0.80	25.47	0.51	22.84	0.69
286.1	19.69	0.68	22.50	0.69	24.24	1.04	24.10	1.21	23.44	0.64	21.98	0.53	19.01	0.97
275.2	15.74	0.65	17.46	0.64	20.32	1.45	19.28	1.14	18.71	0.47	17.64	0.35	16.65	0.93
264.7	13.05	1.84	14.00	1.15	15.61	1.14	15.14	0.83	14.43	0.71	13.97	0.39	12.99	0.62
254.5			10.02	0.64	11.29	0.71	12.00	0.82	11.29	0.46	10.71	0.59	10.39	0.53
244.4			7.63	0.49	8.15	0.27	8.65	0.65	8.22	0.57	8.59	0.43	7.98	0.57
234.3					6.40	0.30	7.06	0.97	5.97	0.29	6.09	0.53	6.16	0.34
223.9					6.22	1.25	5.61	1.26	4.06	0.35	4.35	0.49	4.17	0.17
212.9											2.91	0.45	3.08	0.58

TABLE V. *Point* beam asymmetries (Sec. IV D 3), Σ, for $p(\vec{\gamma},\pi^0)$ as a function of incident lab photon energy and c.m. reaction angle. The *net measurement errors* listed here are the quadrature sum of statistical and *point-specific systematic* uncertainties (Sec. VI). There are no additional systematic polarization scale uncertainties.

E_γ (MeV)	60°	±err	70°	±err	80°	±err	90°	±err	100°	±err
333.5	−0.478	0.029	−0.510	0.014	−0.521	0.012	−0.536	0.009	−0.544	0.008
322.2	−0.470	0.014	−0.485	0.009	−0.525	0.007	−0.537	0.006	−0.533	0.005
309.6	−0.455	0.014	−0.484	0.008	−0.500	0.007	−0.512	0.005	−0.514	0.004
297.7	−0.429	0.022	−0.466	0.009	−0.484	0.007	−0.502	0.005	−0.491	0.004
286.1	−0.420	0.042	−0.471	0.012	−0.468	0.007	−0.473	0.005	−0.471	0.005
275.2			−0.430	0.020	−0.448	0.008	−0.449	0.006	−0.439	0.005
264.7			−0.397	0.083	−0.421	0.010	−0.424	0.007	−0.405	0.006
254.5					−0.349	0.017	−0.396	0.009	−0.379	0.007
244.4					−0.358	0.041	−0.368	0.013	−0.358	0.011
234.3							−0.330	0.022	−0.347	0.019
223.9							−0.300	0.074	−0.223	0.039
E_γ (MeV)	110°	±err	120°	±err	130°	±err	150°	±err		
333.5	−0.545	0.012	−0.516	0.012	−0.468	0.014	−0.308	0.044		
322.2	−0.522	0.006	−0.489	0.006	−0.444	0.007	−0.297	0.014		
309.6	−0.496	0.005	−0.468	0.005	−0.417	0.006	−0.254	0.009		
297.7	−0.471	0.006	−0.448	0.006	−0.384	0.007	−0.245	0.009		
286.1	−0.449	0.006	−0.410	0.006	−0.354	0.007	−0.230	0.010		
275.2	−0.411	0.007	−0.368	0.007	−0.333	0.008	−0.214	0.012		
264.7	−0.376	0.008	−0.355	0.008	−0.290	0.009	−0.189	0.031		
254.5	−0.349	0.009	−0.314	0.009	−0.266	0.011				
244.4	−0.343	0.011	−0.289	0.011	−0.239	0.013				
234.3	−0.265	0.017	−0.259	0.014	−0.233	0.016				
223.9	−0.238	0.083	−0.220	0.022	−0.182	0.021				
212.9					−0.204	0.045				

tions and/or detector alignment (1.1%).

Adding these in quadrature gives a *total systematic scale uncertainty* of 2% for the cross sections of Tables II, IV, and VI.

For the asymmetry ratios, the influence of the *point-specific* systematic effects discussed above is at most third order and is not significant. In addition, the *systematic scale uncertainties* cancel completely. However, these ratios are affected by variations in the beam polarization. There are two sources of such uncertainties, fluctuations in laser polarization and in the fraction of unpolarized bremsstrahlung. The polarization of the laser in its two orthogonal states was

TABLE VI. *Point* cross sections (Sec. IV D 3), $d\sigma/d\Omega_{\text{c.m.}}$ in μb/sr, for $p(\gamma,\pi^+)$ in the c.m. frame as a function of incident lab photon energy and c.m. reaction angle. The *net measurement errors* listed here are the quadrature sum of *statistical* and *point-specific systematic* uncertainties (Sec. VI). In addition to these, there is an additional systematic scale uncertainty of 2% (Sec. VI A).

E_γ (MeV)	20°	±err	55°	±err	65°	±err	75°	±err	85°	±err	105°	±err	150°	±err	170°	±err
322.2	10.47	0.81	20.90	0.42	22.46	0.38	23.90	0.40	25.08	0.55	23.93	0.68	15.38	0.39	12.23	0.55
309.6	8.40	0.54	20.06	0.39	21.66	0.36	23.73	0.39	25.21	0.54	25.48	0.64	16.42	0.40	15.04	0.43
297.7	5.65	0.49	18.61	0.36	20.45	0.33	22.53	0.37	24.14	0.52	24.93	0.64	16.68	0.40	15.03	0.43
286.1	5.03	0.52	16.71	0.33	18.43	0.30	20.85	0.34	22.23	0.48	23.68	0.64	16.52	0.40	15.89	0.44
275.2	5.07	0.54	14.65	0.29	16.49	0.27	18.68	0.31	20.12	0.43	21.93	0.60	15.47	0.38	14.81	0.43
264.7	2.74	0.54	13.08	0.26	14.45	0.24	16.57	0.27	17.69	0.39	20.80	0.62	14.44	0.35	13.53	0.43
254.5	3.38	0.66	11.88	0.24	13.21	0.22	14.72	0.25	16.13	0.35	18.75	0.59	13.48	0.33	12.44	0.41
244.4	3.20	0.67	10.43	0.21	11.58	0.20	13.43	0.23	14.48	0.32	16.00	0.52	12.76	0.32	11.42	0.40
234.3	4.29	0.71	9.93	0.20	10.69	0.18	11.68	0.20	12.36	0.28	15.36	0.52	11.57	0.29	10.56	0.42
223.9	4.85	0.83	9.60	0.20	9.75	0.17	10.58	0.18	11.42	0.26	14.23	0.51	10.21	0.26	10.12	0.79
212.9			8.67	0.18	8.90	0.16	9.68	0.17	10.08	0.24						

TABLE VII. *Point* beam asymmetries (Sec. IV D 3), Σ, for $p(\vec{\gamma},\pi^+)$ as a function of incident lab photon energy and c.m. reaction angle. The *net measurement errors* listed here are the quadrature sum of statistical and *point-specific systematic* uncertainties (Sec. VI). There are no additional systematic polarization scale uncertainties.

E_γ (MeV)	20°	±err	55°	±err	65°	±err	75°	±err
322.2	−0.364	0.075	−0.439	0.011	−0.435	0.008	−0.442	0.008
309.6	−0.294	0.061	−0.386	0.008	−0.377	0.006	−0.381	0.006
297.7	−0.417	0.089	−0.342	0.008	−0.323	0.006	−0.330	0.006
286.1	−0.354	0.112	−0.294	0.009	−0.291	0.007	−0.284	0.007
275.2	−0.332	0.110	−0.286	0.010	−0.261	0.008	−0.252	0.007
264.7	−0.767	0.246	−0.286	0.011	−0.238	0.009	−0.233	0.008
254.5	−0.348	0.209	−0.279	0.012	−0.231	0.009	−0.203	0.009
244.4	−0.221	0.237	−0.280	0.013	−0.246	0.010	−0.190	0.010
234.3	−0.019	0.195	−0.291	0.014	−0.246	0.011	−0.207	0.011
223.9	−0.261	0.215	−0.263	0.016	−0.259	0.013	−0.224	0.013
212.9			−0.263	0.018	−0.231	0.014	−0.202	0.014
E_γ (MeV)	85°	±err	105°	±err	150°	±err	170°	±err
333.5							−0.071	0.113
322.2	−0.425	0.010	−0.436	0.015	−0.150	0.011	−0.061	0.042
309.6	−0.374	0.008	−0.373	0.010	−0.145	0.007	−0.014	0.022
297.7	−0.327	0.008	−0.303	0.010	−0.103	0.007	0.017	0.022
286.1	−0.277	0.009	−0.259	0.011	−0.102	0.007	−0.039	0.021
275.2	−0.244	0.010	−0.232	0.012	−0.091	0.008	0.025	0.023
264.7	−0.201	0.012	−0.193	0.014	−0.076	0.009	0.021	0.027
254.5	−0.189	0.013	−0.189	0.015	−0.074	0.010	−0.017	0.029
244.4	−0.179	0.015	−0.134	0.018	−0.066	0.011	0.087	0.033
234.3	−0.172	0.017	−0.145	0.020	−0.039	0.012	−0.009	0.041
223.9	−0.174	0.018	−0.160	0.023	−0.034	0.014	−0.025	0.073
212.9	−0.157	0.020						

measured 67 times during the course of the experiment (Sec. II) and the associated systematic uncertainty was taken as the standard deviation of these measurements (1%). The unpolarized bremsstrahlung was sampled continuously and was always less than 1% (Sec. II). These effects lead to *point-specific* systematic uncertainties which have been propagated through the analysis for each datum [Eqs. (2) and (3d), and Fig. 3] and combined in quadrature with statistical uncertainties to yield the *net measurement errors* listed in the tables. There are no additional uncertainties on the asymmetry ratios beyond those listed in the tables.

B. Comparisons with other data

A selection of the results from Tables II–VII are compared with other published measurements in Fig. 37 to Fig. 42. The results from the present work are shown as solid circles, and other measurements are plotted as the open symbols defined in the legends.

Angular distributions for Compton scattering are shown in Fig. 37 for four incident beam energies. The Mainz cross sections (open circles) are taken from three different experiments at 75° c.m. [41], 90° c.m. [40], and 130.7° lab [42]. In the bottom panels, the average of the LEGS results at 224.3 MeV and 234.7 MeV are plotted to compare with 230 MeV data from the Saskatchewan Accelerator Lab (SAL), which are shown as open triangles [59]. All of these are in quite good agreement. As noted previously (Sec. I and in [37]), the Compton data prior to 1980 were systematically low in the region of the Δ peak. In the upper-left panel of Fig. 37 the Bonn data from [32] are shown rescaled by a factor of 1.28 (crossed squares). Apart from the obvious normalization problem, the general angular dependence of their reported cross sections is in good agreement with the new results. The only other published asymmetry datum in this energy region, from Frascati [60], is in agreement with our results within errors.

The energy dependence of the $p(\vec{\gamma},\gamma)$ c.m. cross sections and beam asymmetries are shown in Fig. 38 at the three angles for which data is available from recent experiments at Mainz: [41] using the CATS NaI detector and a recoil proton detector for 75° c.m. scattering, [40] using the COPP photon-proton coincidence apparatus for 90° c.m., and [42] using the CATS NaI to detect photons at ~138° c.m. The separation of the solid and dashed bands in the left panels indicate the magnitude of the systematic scale uncertainties for the LEGS and Mainz cross section data, respectively. At 75° and 90° c.m. the overlap with the present work is nearly perfect. These measurements used a photon-proton coinci-

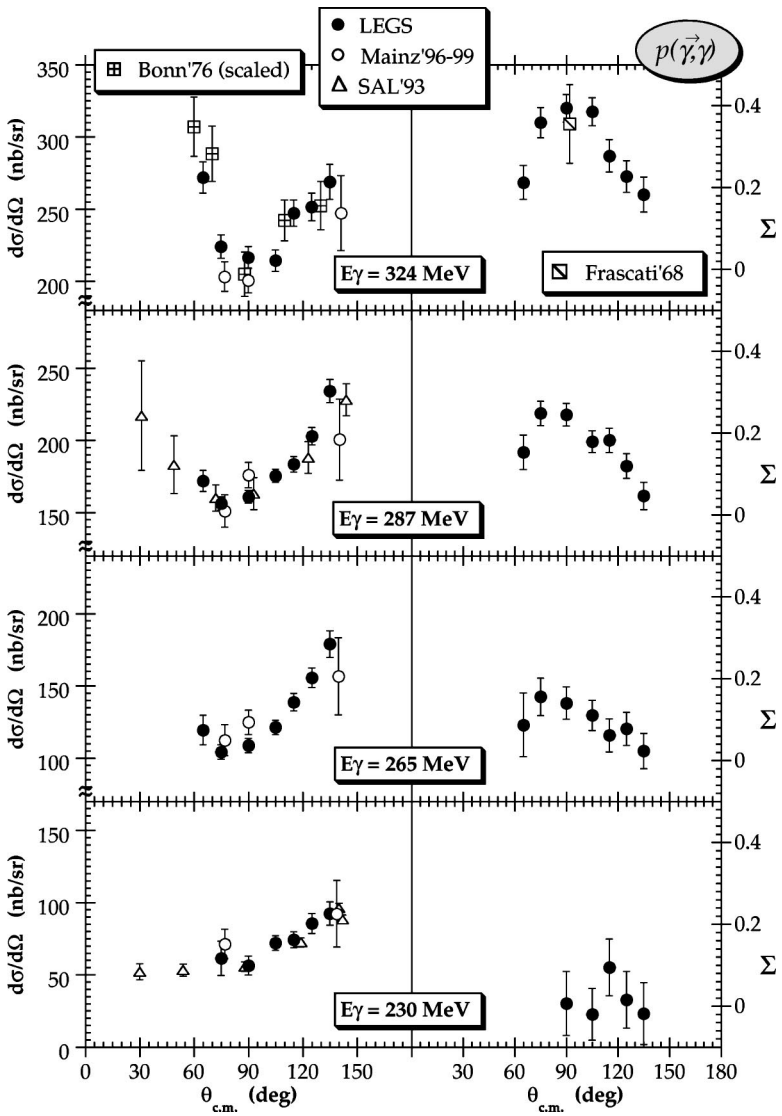

FIG. 37. Angular distributions of c.m. cross sections (left panels) and beam asymmetries (right panels) from the present work (solid circles) for the $p(\vec{\gamma},\gamma)$ reaction compared with measurements from other laboratories [41,40,42,59,60]. Data are shown for four incident (lab) beam energies. The Mainz point at 287 MeV and 75° is interpolated from [41]. The zero is suppressed in several of the left panels. The Bonn data in the upper-left panel have been scaled up by 28% from the values published in [32].

dence to separate the π^0 background in much the same way as in the present work. The Mainz data at $\sim 138°$ c.m. ignored the proton recoils and relied solely on the resolution of a NaI to resolve Compton scattering. Their statistical errors are sufficiently large to overlap completely with our data.

We note that in Ref. [42], *nominally equivalent* free-proton scattering data were extracted from an analysis of quasifree scattering from a deuterium target at 148.8° lab. Those results lie somewhat below the trends shown in Fig. 37. However, significant corrections were applied that lowered the cross sections from their $d(\gamma,\gamma p)$ values. As a test of these corrections, the authors of [42] offered their proton scattering measurements shown as the open-circle points at $\sim 138°$ c.m. in Fig. 37 and Fig. 38. However, the error bars on these data are clearly too large to support any conjecture of a shift between our LEGS results and the *centroids* of the open-circle points.

Angular distributions for π^0 photoproduction are shown in Fig. 39 for four incident beam energies. Recent measurements from Mainz using the DAPHNE detector [43] are shown as open circles. Data from Lund [61] are plotted as open triangles ($\triangle$), and results from Bonn [38] as crossed squares. Asymmetry data from Kharkov [62] are shown as inverted triangles ($\triangledown$) in the upper-right panel. These asymmetry data, and the LEGS results in Table V, include all statistical and systematic uncertainties. The error bars on the Mainz asymmetries are taken as the quadrature sum of the statistical and the 2% systematic polarization uncertainties quoted in [43]. While the asymmetry data all agree within errors, we observe a difference in the cross sections that grows with energy. Below about 270 MeV, our results are consistent with the Bonn data of [38] within errors, while at higher energies our data at central angles are noticeably higher, by as much as about 13% at the peak of the P_{33} Δ resonance. The Lund data of [61] are in agreement with our results at 322 MeV, but seem to remain higher than the Bonn data set at lower energies, although below 300 MeV the Lund data are quite sparse. The recent Mainz results of [43] are in agreement with the Bonn data.

In Fig. 40 we compare the energy dependence of the 90° c.m. $p(\vec{\gamma},\pi^0)$ cross sections and beam asymmetries from the present data set with those of Mainz [43] and Kharkov [62]. The separation of the solid and dashed bands in the left panel

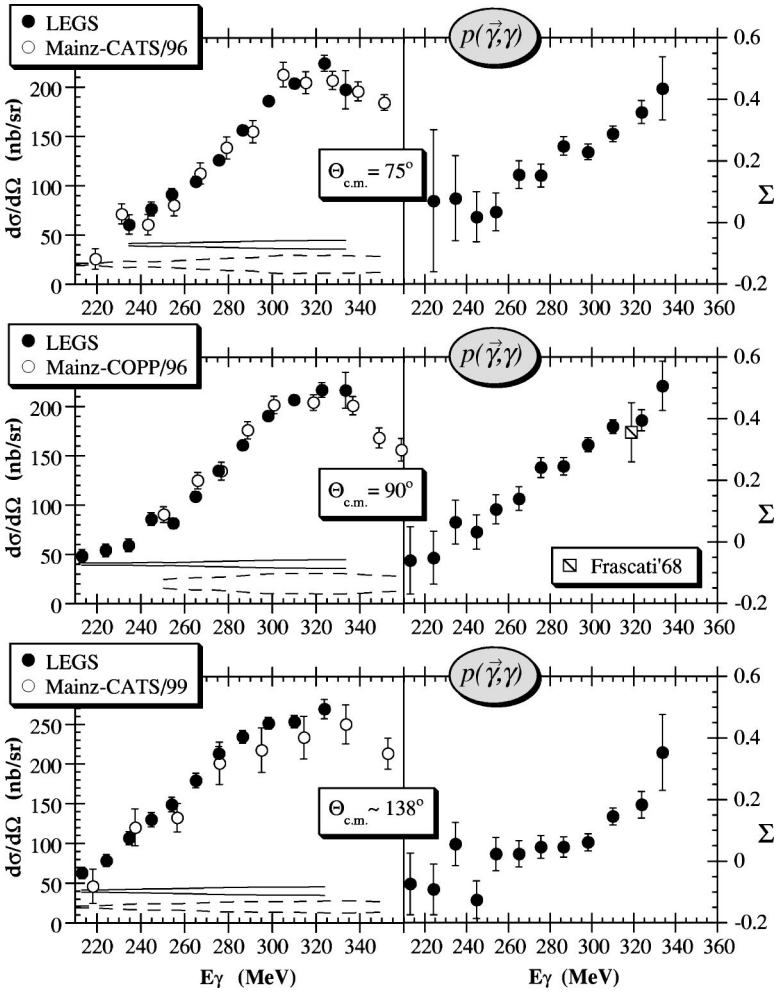

FIG. 38. Excitation functions for c.m. cross sections (left panels) and beam asymmetries (right panels) from the present work (solid circles) for the $p(\vec{\gamma},\gamma)$ reaction compared with recent cross section measurements from Mainz [41,40,42] and an asymmetry datum from Frascati [60]. Data are shown for three different c.m. scattering angles. The bottom-left panel, marked ~138°, compares the 135° c.m. LEGS data with Mainz results at a fixed lab angle of 130.7° [42]. The solid and dashed bands in the left panels indicate the systematic scale uncertainties for the LEGS and Mainz cross section data, respectively.

indicates the magnitude of the systematic scale uncertainties for the LEGS and Mainz cross section data, respectively. These systematic uncertainties allow one to adjust the corresponding data sets up, or down, by half the spacing of these bands, and that is a factor of 2 too small to bring these sets into agreement.

Angular distributions for π^+ photoproduction are shown in Fig. 41 for four incident beam energies. Recent measurements from Mainz using the DAPHNE detector [43], and from Bonn using the PHOENICS detector [44], are shown as open circles and open diamonds, respectively. A selection of the older Bonn data, interpolated in energy from [39], are plotted as crossed-squares. As was the case with the π^0 measurements, the Mainz and Bonn π^+-production experiments agree with each other but are below the LEGS data near the peak of the Δ-resonance. Cross sections from Tokyo are shown as crosses [63] and are closer to the LEGS results. Asymmetry data from Kharkov [64] are shown as inverted triangles ($\bigtriangledown$) in the upper-right panel. The LEGS asymmetries in Table VII include all statistical and systematic uncertainties. The error bars on the Mainz and Kharkov asymmetries are taken as statistical errors summed in quadrature with systematic polarization uncertainties of 2% [43] and 3% [64], respectively. While the Kharkov asymmetries are in reasonable agreement with our results, the Mainz data tend to be more negative at central angles, although the differences are not more than one standard deviation.

In Fig. 42 we compare the energy dependence of the 85° c.m. $p(\vec{\gamma},\pi^+)$ cross sections and beam asymmetries from the present data set with those from Mainz [43]. The separation of the solid and dashed bands in the left panel indicates the magnitude of the systematic scale uncertainties for the LEGS and Mainz cross section data, respectively. The cross section trends are similar to those of Fig. 40, and once again the estimated systematic uncertainties are too small to bring these data sets into agreement. The Mainz π^+ asymmetries also appear to become more negative with energy.

C. Total cross sections for $p(\gamma,\pi^+)$

In the present work, the angular coverage for π^+ production (20° to 170°) is sufficiently large to permit an integration of angular distributions to obtain total cross sections for $p(\gamma,\pi^+)$. The data of Table VI have been fitted to the functional form

$$\frac{d\sigma(\theta)}{d\Omega_{\rm c.m.}} = \frac{1}{(1-\beta_{\rm c.m.}\cos\theta)^2}\sum_{n=0}^{4}\alpha_n\cos^n\theta, \qquad (11)$$

where $\beta_{\rm c.m.}$ is the velocity of the pion in the c.m. frame. There are significant contributions to $p(\gamma,\pi^+)$ from the

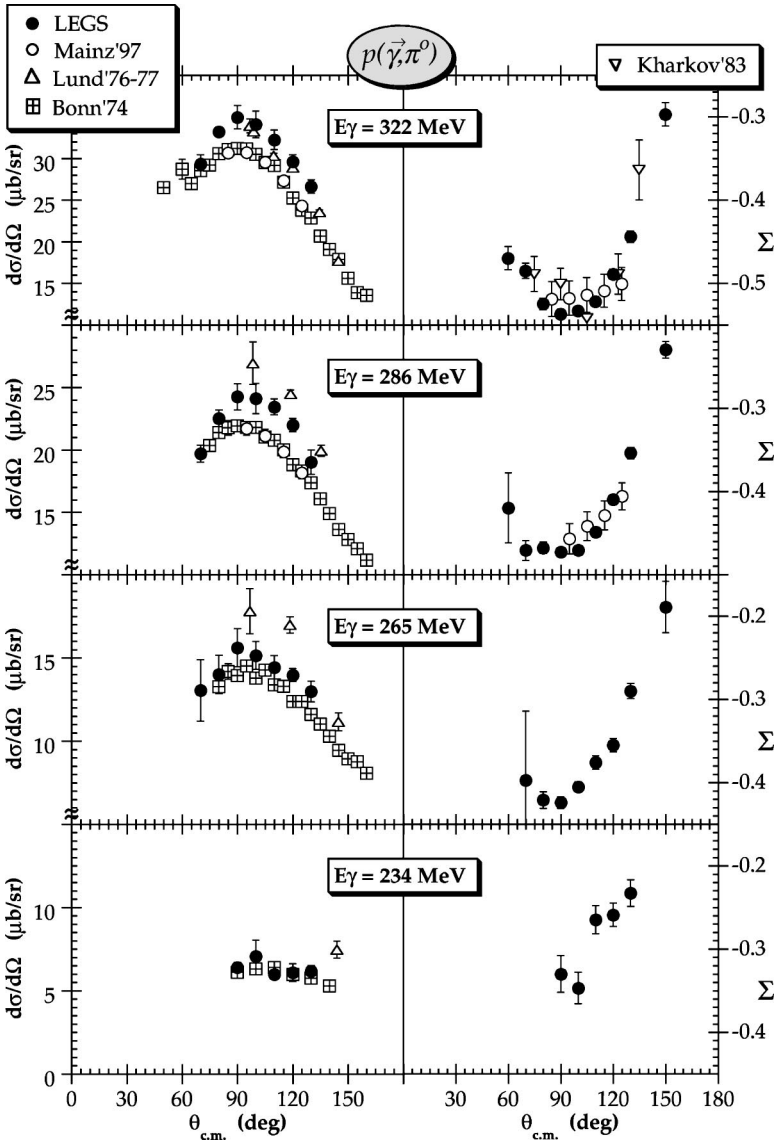

FIG. 39. Angular distributions of c.m. cross sections (left panels) and beam asymmetries (right panels) from the present work (solid circles) for the $p(\vec{\gamma},\pi^0)$ reaction compared with measurements from other laboratories [43,61,38,62]. Data are shown for four incident (lab) beam energies, and the Mainz and Bonn results have been interpolated to these energies. (The zero is suppressed in several of the left panels.)

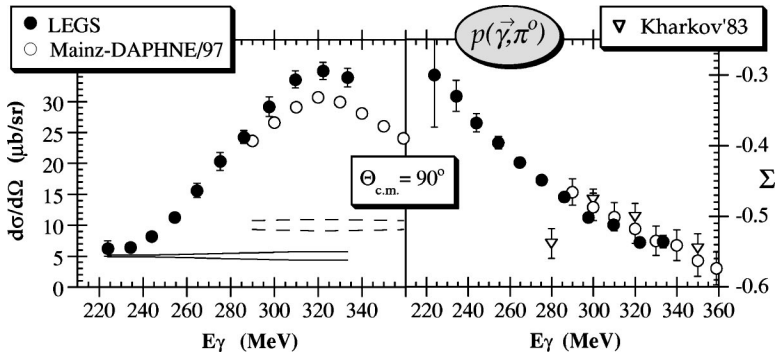

FIG. 40. Excitation functions for 90° c.m. cross sections (left panel) and beam asymmetries (right panel) from the present work (solid circles) for the $p(\vec{\gamma},\pi^0)$ reaction compared with measurements from Mainz and Kharkov [43,62]. The 90° Mainz points are the average of 85° and 95° data from [43]. The solid and dashed bands in the left panel indicate the systematic scale uncertainties for the LEGS and Mainz cross section data, respectively. The error bars on the Mainz asymmetries are taken as the quardature sum of statistical and 2% systematic polarization uncertainties [43]. (The asymmetry errors on the LEGS and Kharkov data reflect the total uncertainties.)

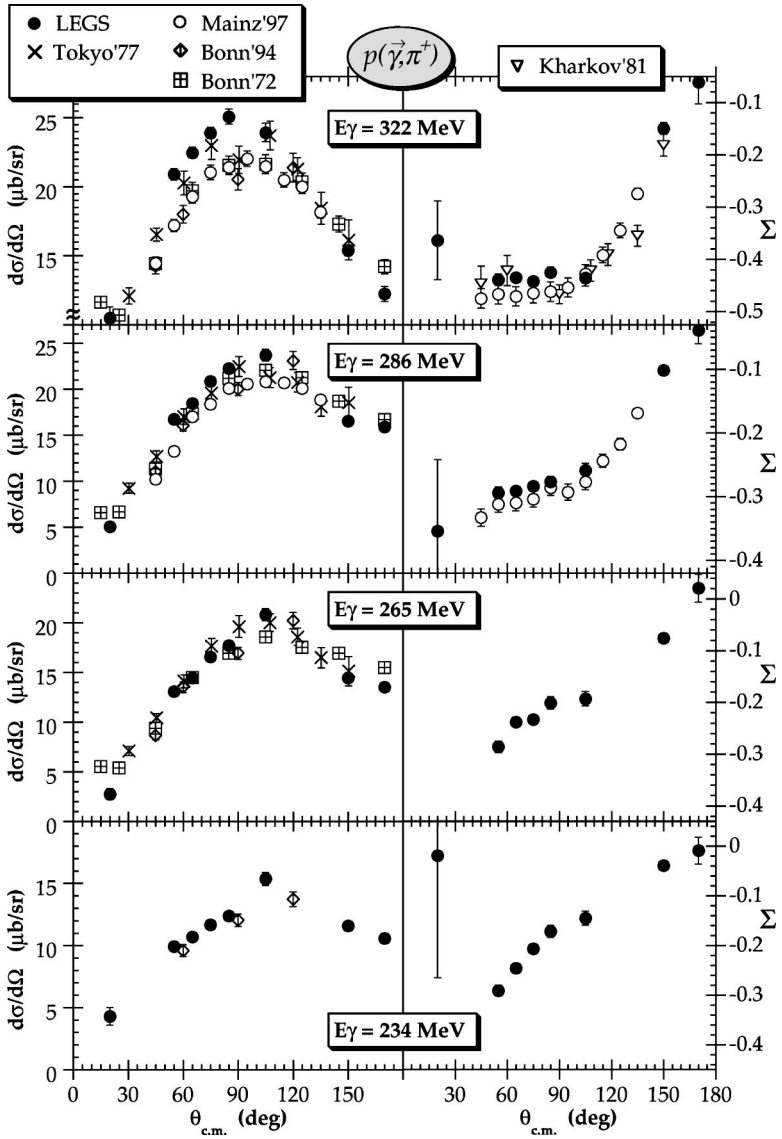

FIG. 41. Angular distributions of c.m. cross sections (left panels) and beam asymmetries (right panels) from the present work (solid circles) for the $p(\vec{\gamma},\pi^+)$ reaction compared with measurements from other laboratories [43,44,39,63,64]. Data are shown for four incident (lab) beam energies, and the Mainz, Bonn and Tokyo results have been interpolated to these energies. (The zero is suppressed in the upper-left panel.)

t-channel pole graph, which contains quite high angular momentum components. These affect the π^+ distribution at extreme angles, and the $(1-\beta_{c.m.}\cos\theta)^{-2}$ factor in Eq. (11) ensures rapid convergence [65]. Analytic integration of Eq. (11) then gives the total π^+ cross sections for each beam energy. The results are listed in Table VIII, and plotted in Fig. 43, together with similar integrations of the Tokyo and Bonn data from [63,66]. The LEGS and Tokyo cross sections are quite close, even without considering their systematic scale uncertainties (2% and 7%, respectively), while the Bonn results (which have a 6% systematic scale uncertainty) are about 10% lower at the peak of the Δ resonance.

D. Difference in (γ,π) cross section scales

There are several conundrums created by our new data. The first can be summarized by comparing the center-left panel of Fig. 38 and the left panel of Fig. 40. While the LEGS and Mainz results are in excellent agreement for $p(\gamma,\gamma)$, the cross sections for $p(\gamma,\pi^0)$ differ by more than evaluations of systematic uncertainties allow. Furthermore, the LEGS 90° c.m. Compton and π^0-production cross sections come from totally simultaneous measurements, using the same set of data runs to select two different regions of the same channel-identification spectrum (mid-panel of Fig. 8) from the same detectors. The same particles, photons and recoil protons, were detected for the two channels, and the detection efficiencies come not from simulations but from direct measurements. As a result, the LEGS $p(\gamma,\gamma)$ and $p(\gamma,\pi^0)$ results are locked together, so that even if one were to arbitrarily adjust the overall experimental cross section scale, it is impossible to remove the discrepancy with Mainz in the π^0 channel without destroying the agreement in the Compton channel.

The comparisons of Fig. 39 and Fig. 41 between the LEGS and Mainz/Bonn π-production cross sections reveal a discrepancy that appears to grow with energy. We have examined the extent to which this can be accommodated by a simple normalization scale factor. The result of scaling the Mainz and Bonn cross sections of Refs. [43,38,39] up by 10% is shown in Fig. 44. The overall agreement is quite good in the π^0 channel. Evidently, the differences in Fig. 39

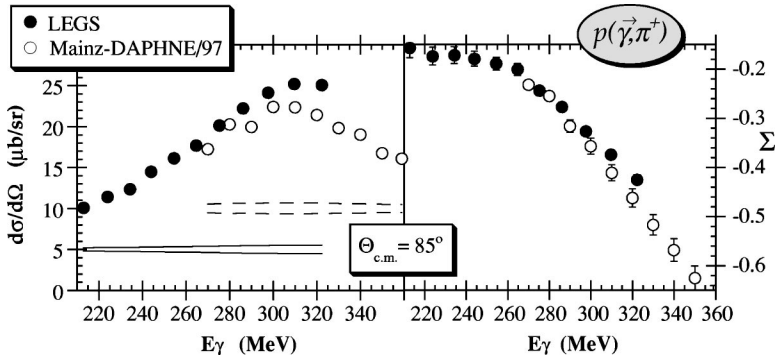

FIG. 42. Excitation functions for 85° c.m. cross sections (left panel) and beam asymmetries (right panel) from the present work (solid circles) for the $p(\vec{\gamma},\pi^+)$ reaction compared with recent measurements from Mainz [43]. The solid and dashed bands in the left panel indicate the systematic scale uncertainties for the LEGS and Mainz cross section data, respectively. The error bars on the Mainz asymmetries are taken as the quardature sum of statistical and 2% systematic polarization uncertainties [43]. (The asymmetry errors on the LEGS data reflect the total uncertainties.)

are growing, not because the energy is increasing, but simply because the cross sections are increasing. For π^+ production, this 1.10 rescaling factor achieves reasonable agreement over the central angular range, although the Bonn data are noticeably higher at forward and backward angles. Measurements of π^+ at extreme angles require detectors close to the beam, and we can easily speculate that these differences are due to $e^{\pm}$ backgrounds in the Bonn data. Compared with bremsstrahlung sources, laser-backscattering produces a photon beam that is virtually background-free. Assuming this explanation, one concludes that the essential difference between the LEGS and Mainz/Bonn data sets is a normalization factor of 10% [67]. The conundrum here is that this is *very large*. The estimated systematic scale errors on the LEGS, Mainz and Bonn data sets are 2%, 3% and 5–6 %, respectively. A 10% scale change is not easy to explain away.

As discussed in Sec. II, a $\gamma+{}^4$He measurement was carried out at LEGS between the second and third running periods of the present experiment, during which both elastic scattering and π^0 production were measured [68,48]. (That ^{4}He experiment in fact used the same flux monitoring and the same 48 cm diameter NaI to detect high energy γ rays as the present proton experiment.) It is interesting to note that the ${}^4\mathrm{He}(\gamma,\gamma)$ and ${}^4\mathrm{He}(\gamma,\pi^0)$ cross sections measured in that work do not show any scale shifts when compared with recent measurements of these reactions from Mainz [69–71]. On the whole, data from LEGS and Mainz on ^{4}He are in reasonable agreement, although both the LEGS and Mainz ^{4}He experiments relied on simulated detector efficiencies to extract cross sections.

The 10% scale difference between the LEGS and Mainz/Bonn data sets is quite troubling, particularly in light of the relatively minor role of simulations in the analysis of the present experiment. Any future experiment to investigate this scale difference will have to have at least comparably large levels of kinematic overdetermination, with similar capabilities of determining detector efficiencies by direct measurement.

TABLE VIII. Total cross sections in μb for $p(\gamma,\pi^+)$, as a function of incident lab photon energy.

E_γ (MeV)	$\sigma^{\mathrm{total}}(\gamma,\pi^+)(\mu\mathrm{b})$	$\pm$ err
322.2	257.5	3.1
309.6	259.2	2.9
297.7	248.5	2.9
286.1	232.3	2.8
275.2	212.3	2.7
264.7	193.1	2.6
254.5	177.0	2.5
244.4	158.2	2.4
234.3	146.7	2.3
223.9	137.4	2.4

VII. SIMULTANEOUS MULTIPOLE ANALYSIS OF $p(\gamma,\pi)$ AND $p(\gamma,\gamma)$

The Compton scattering, π photoproduction, and πN scattering channels are inter-related by unitarity through a common *S matrix*. Single π photoproduction can be described in terms of four independent helicity amplitudes, H_i with $i=[1,4]$, each having real and imaginary parts [72].

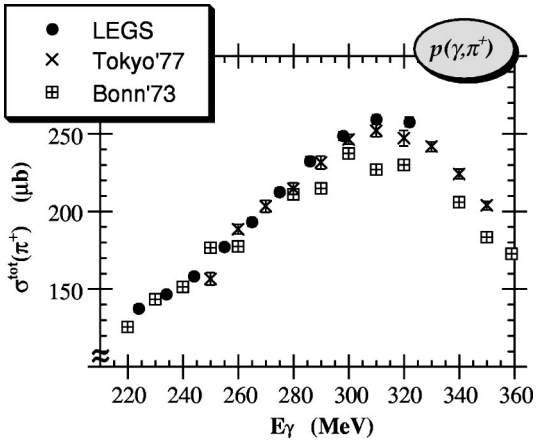

FIG. 43. Total cross sections for $p(\gamma,\pi^+)$ from the present work (solid circles) compared with results from [63,66].

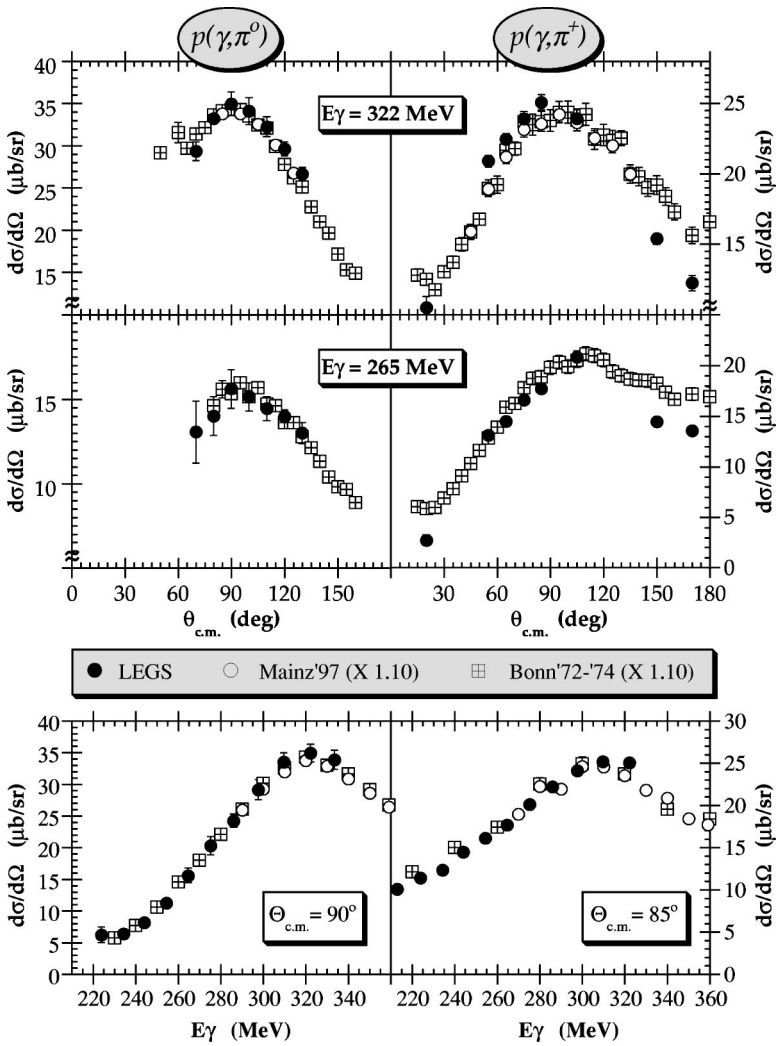

FIG. 44. Cross sections for $p(\gamma,\pi^0)$, left panels, and $p(\gamma,\pi^+)$, right panels, from the present work (solid circles). These are compared to data from Mainz [43] (open circles) and Bonn [38,39] (crossed squares), both *rescaled* by a factor of 1.10.

Cross sections and polarization asymmetry ratios can be expressed in terms of products of these amplitudes. At any given energy, a minimum of eight independent observables, for each pion charge state, are necessary to specify the photopion amplitude to within an overall phase [25]. (In principle, seven should be sufficient to fix the four complex H_i to within a common phase, but in fact there does not exist a measurable set of seven observables that are sufficiently independent.) Such complete information is not yet available at any energy. The conventional approach to overcoming this limitation is to utilize the unitarity connection with πN scattering. At energies where there is only one open channel, which for photoproduction implies energies below 2π threshold or $E_\gamma = 309$ MeV lab, Watson's theorem requires the (γ,π) and (π,π) channels to have a common phase [23], and various model-dependent prescriptions can be used to extend this unitarity relation to higher energies. Since the πN phase shifts are determined quite accurately in terms of angular momentum multipoles, Watson's theorem can be used to bring this information into photoproduction if the H_i helicity amplitudes are expanded in terms of multipoles with specific πN final state angular momenta. Once the (γ,π) multipoles are specified, the imaginary parts of the six Compton helicity amplitudes A_i are then completely determined by unitarity and a dispersion calculation involving integrals of the pion multipoles can be used to generate their real parts [24,9]. All previous analyses of π production have relied almost exclusively on multipole fits to only four (γ,π) observables, the cross section and the three single polarization asymmetries, Σ (linearly polarized beam), T (target), and P (recoil nucleon), with phases taken from πN scattering. Here we treat Compton scattering on an equal footing and simultaneously fit two additional observables, the (γ,γ) cross sections and beam polarization asymmetries. In this way we bring in two new pieces of information and exploit the complete (γ,γ), (γ,π), and (π,π) three-channel unitarity.

A. Parametrization of (γ,π) multipoles

Pion-production multipoles can readily be fitted to observables at a series of fixed energies. However, since one is always dealing with less than the complete set of observables needed to determine the amplitude, the χ^2 space will generally have multiple minima, and even the global minimum can be insignificantly deeper than another more physically meaningful one. This usually causes the extracted multipoles to fluctuate with energy more rapidly than can be physically

justified. The solution to this problem is to impose continuity by parametrizing the multipoles with a smoothly varying function of energy. This greatly reduces the number of free parameters and has the added advantage of bridging gaps in the data coverage that invariably occur [26]. There will be some model dependence with such a procedure, but this can be held to a minimum by using a physically motivated parametrization [16].

We have performed a series of energy-dependent analyses, expanding the π-production amplitude into electric and magnetic partial waves, $E^{\tau}_{l\pm}$ and $M^{\tau}_{l\pm}$ in the CGLN notation of [73], with relative πN angular momentum l, and intermediate-state spin $j=l\pm 1/2$ and isospin $\tau=1/2$ or 3/2. The (γ,π) multipoles have been parametrized with a K-matrix-like unitarization of the form [57]

$$A^{\tau}_{l\pm}(E_\gamma)=\{A^{\tau}_B(E_\gamma)+\alpha_1\varepsilon_\pi+\alpha_2\varepsilon_\pi^2 + \alpha_3\Theta_{2\pi}(E_\gamma-E_\gamma^{2\pi})^2\}(1+iT^l_{\pi N})+\beta T^l_{\pi N}. \tag{12}$$

Here, E_γ and ε_π are the beam and corresponding π^+ kinetic energies, and A^{τ}_B is the full pseudovector Born multipole, including ρ and ω t-channel exchange [74], included here for $l\leqslant 19$. In addition to the Born terms, a low-order polynomial in the pion energy ε_π has been included to allow for other possible terms that are expected from contributions such as u-channel resonances and pion rescattering [12]. While it is obviously desirable to keep the number of fitting constants to a minimum, the multipole parametrization must have enough degrees of freedom to be able to describe the actual energy dependence dictated by the underlying physics. To ensure this, our criterion has been to verify that fits to mock data generated from *GW-SAID* predictions are able to reproduce the GW[SM95] photo-pion multipole solution [75]. Each multipole up to and including F-waves contains a term in α_1, while the additional α_2 term is used only in the largest multipoles $E^{1/2}_{0+}$ and $M^{3/2}_{1+}$, and in the $E^{3/2}_{1+}$ which is of special interest. The α_3 term containing the unit Heaviside step function $\Theta_{2\pi}$ ($=1$ for $E_\gamma>309$ MeV) is used only in the E_{0+} amplitudes to accommodate possible effects from S-wave 2π production. The *GW-SAID*[SM95] πN scattering solution is used for the T-matrix elements [75]. Below 2π threshold, $E_\gamma^{2\pi}=309$ MeV, $T^l_{\pi N}$ reduces to $\sin(\delta_l)e^{i\delta_l}$, $\delta_l(E_\gamma)$ being the elastic πN phase shift, and $(1+iT^l_{\pi N}) = \cos(\delta_l)e^{i\delta_l}$. Thus, Eq. (12) explicitly satisfies Watson's theorem [23] below $E_\gamma^{2\pi}$ and provides a consistent, albeit model-dependent, procedure for maintaining unitarity at higher energies. The maximum E_γ included in our analyses is 350 MeV, which is over the 2π threshold, but since the $p(\gamma,2\pi)$ cross sections are negligible near threshold and still very small below 400 MeV, the model dependence associated with this extended unitarization procedure is insignificant.

When a single s-channel resonance dominates a partial wave having only one open decay channel, the last term in Eq. (12) exactly reduces to a Breit-Wigner energy dependence. The β term was fixed at zero for all multipoles except $M^{3/2}_{1+}$, $E^{3/2}_{1+}$, and $M^{1/2}_{1-}$, the first two describing $M1$ and $E2$ $N\rightarrow P_{33}$ excitation and the latter allowing for a possible tail from the P_{11} resonance. The sensitivity to tails from the $N^*(1535)$ and $\Delta(1700)$ resonances were examined by adding β terms to the $E^{1/2}_{0+}$ and $E/M^{3/2}_{2-}$ multipoles, respectively. These resonances, though higher in energy than the P_{11}, are quite broad. However, the presence of β terms in these multipoles does not improve the fit, and so these resonant contributions were not included in the fits described here. The multipole parametrization of Eq. (12) is equivalent to that used in analyses by the RPI group [16,76] and very similar to that used by the GW/SAID group [77].

B. Calculation of (γ,γ) multipoles

Once the (γ,π) multipoles are fixed by the choice of parameters in Eq. (12), the imaginary parts of the six crossing-even invariant Compton helicity amplitudes, $A_i(\nu,t)$ with $i=[1,6]$, are completely determined by unitarity [24,36], and dispersion integrals can be used to calculate their real parts. For the latter, we have followed the procedures of L'vov and co-workers [24,55], writing the real part of the scattering amplitude as fixed-t dispersion relations using a Cauchy loop of finite size,

$$\mathrm{Re}\,A_i(\nu,t)=A^B_i(\nu,t)+\frac{2}{\pi}P\int_{\nu_0}^{\nu_{max}}\frac{\nu'\,\mathrm{Im}\,A_i(\nu',t)}{\nu'^2-\nu^2}d\nu' + A^{as}_i(t). \tag{13}$$

Here, $\nu=(1/4M)(s-u)$, M is the nucleon mass, and A^B_i denotes the s- and u-channel Compton Born contributions which are determined completely by the nucleon's charge and magnetic moment. (Throughout this discussion s, u, and t are the usual Mandelstam variables, with $s+u+t=2M^2$.)

The principle value integrals in Eq. (13) are evaluated using pion multipoles in the range $\nu=E_\gamma+t/4M\approx 150$ MeV (π-threshold) to 1500 MeV. Within the interval, $200\leqslant E_\gamma \leqslant 350$ MeV, the π multipoles are varied to fit the data base (Sec. VII C). A reasonable set of pion multipoles is needed to extend the computation of these integrals through the full 0.15–1.5 GeV energy range, and for this we have used the GW[SM95] solution [75] which is close to our fitted solution. Nonetheless, the particular choice of the multipoles used for this extension has little effect on the evaluation of the amplitudes at beam energies below 350 MeV. This is because the numerator of the integrals, $\mathrm{Im}\,A_i$, is completely dominated by single π production and is very large in the fitting interval. At the same time 2π contributions, which are modeled in evaluating the above integrals and thus depend upon theoretical assumptions [55], are quite small below 400 MeV and at higher energies are suppressed by the energy denominator in Eq. (13). As a result, there is in fact very little freedom in these dispersion integrals up to the Δ peak. This allows the Compton observables to be used as an effective constraint on the pion multipoles without incurring additional model dependent uncertainties, provided that we restrict their use to energies below the onset of appreciable $(\gamma,2\pi)$ strength.

The asymptotic terms in Eq. (13), A_i^{as}, are the residual contributions that arise from closing the above integrals with a semicircle of radius ν^{max} in the upper half of the complex ν-plane. Three of the Compton amplitudes (A_3, A_4, and A_5) converge sufficiently rapidly that their asymptotic parts are zero, $A_i^{as}=0$ for $i=(3,4,5)$. The A_6 amplitude also converges rapidly, but its integral is not completely saturated by $\nu=1.5$ GeV. The residual component A_6^{as} is modeled as

$$A_6^{as}(t)=C_6 e^{B_p t/2}, \tag{14}$$

where B_p is taken as 6 GeV^{-2} from a Regge model [24], and C_6 is varied in the multipole fit. Choosing a different value for B_p has almost no effect (Sec. IX D) since the fit compensates by changing the parameter C_6.

The two Compton amplitudes associated with 180° photon helicity flip, A_1 and A_2, have appreciable asymptotic parts. L'vov and collaborators model A_1^{as} as the t-channel exchange of a pair of correlated pions in a relative S-wave. This is equivalent to exchanging the postulated σ-meson,

$$A_1^{as}(t)=\frac{g_{\sigma NN}F_{\sigma\gamma\gamma}}{t-m_\sigma^2}, \tag{15a}$$

with mass $m_\sigma=600$ MeV. Since the coupling constants $g_{\sigma NN}$ and $F_{\sigma\gamma\gamma}$ are essentially unknown, A_1^{as} is taken as

$$A_1^{as}(t)=\frac{C_1}{t-m_\sigma^2}, \tag{15b}$$

and the parameter C_1 is varied in the multipole fit. The asymptotic part of the A_2 amplitude is dominated by t-channel π^0 exchange,

$$A_2^{\pi^0}(t)=\frac{g_{\pi NN}F_{\pi^0\gamma\gamma}}{t-m_{\pi^0}^2}F_\pi(t). \tag{16a}$$

Here $g_{\pi NN}$ is the πNN coupling constant and $F_{\pi^0\gamma\gamma}$ is the π^0 lifetime, $g_{\pi NN}F_{\pi^0\gamma\gamma}=0.331\pm0.012$ GeV^{-1}, and m_{π^0} is the π^0 mass. $F_\pi(t)=(\Lambda_\pi^2-m_\pi^2)/(\Lambda_\pi^2-t)$ is an off-shell form factor for the πNN vertex with cutoff mass $\Lambda_\pi=0.7$ GeV [78]. All of the constants in Eq. (16a) are known and this term should strictly be considered part of the Born amplitude, A_2^B. However we group it with A_2^{as} to maintain consistency with the previous L'vov papers [24,55]. Those publications have assumed that this t-channel π^0 exchange component completely closes the A_2 contour, $A_2^{as}=A_2^{\pi^0}$. However, we have found this assumption insufficient to fit the high energy Compton data [9]. We have added in the pseudoscalar *Born-type* contribution from t-channel η^0 exchange through a term having the same functional form as Eq. (16a), with $g_{\eta NN}F_{\eta\gamma\gamma}=0.097$ GeV^{-1} and $\Lambda_\eta=1.2$ GeV [79]. However, the small coupling constants and the comparatively large η mass, $m_\eta=547.45$ MeV, result in an $A_2^{\eta^0}$ that is less than 2% of $A_2^{\pi^0}$. To provide greater freedom in fitting the amplitudes we have added another term with a t-dependence typical of a process following Regge theory,

$$A_2^{\delta}(t)=C_2 e^{B_\delta t/2}. \tag{16b}$$

This is functionally the same as Eq. (14) and B_δ is again taken as 6 GeV^{-2}. Its precise value is of secondary importance since C_2 is varied in the fit and readily compensates for different values of B_δ (Sec. IX D). The full asymptotic part of A_2 used in our multipole fitting is

$$A_2^{as}(t)=A_2^{\pi^0}(t)+A_2^{\eta^0}(t)+A_2^{\delta}(t). \tag{16c}$$

We have also investigated fits using the functional form of t-channel exchange for the extra A_2^δ term, similar to Eq. (15b), but obtained very similar results indicating that the exact form of the t dependence is not critical for this term (Sec. IX D).

C. Database for multipole fits

The multipoles for single pion photoproduction can be decomposed into terms of definite isospin,

$$\begin{aligned}
A_{\gamma p\to\pi^0 p}&=\left[A^{(0)}+\frac{1}{3}A^{(1)}\right]+\frac{2}{3}A^{(3/2)},\\
A_{\gamma p\to\pi^+ n}&=\sqrt{2}\left[A^{(0)}+\frac{1}{3}A^{(1)}\right]-\frac{\sqrt{2}}{3}A^{(3/2)},\\
A_{\gamma n\to\pi^0 n}&=-\left[A^{(0)}-\frac{1}{3}A^{(1)}\right]+\frac{2}{3}A^{(3/2)},\\
A_{\gamma n\to\pi^- p}&=\sqrt{2}\left[A^{(0)}-\frac{1}{3}A^{(1)}\right]+\frac{\sqrt{2}}{3}A^{(3/2)},
\end{aligned} \tag{17}$$

where the (0) and (1) superscripts indicate the scalar and vector parts of the isospin 1/2 multipole, and the (3/2) superscript denotes the $\tau=3/2$ component. A complete description of $A^{(0)}$, $A^{(1)}$, and $A^{(3/2)}$ would require data from at least three of the channels in Eq. (17), and this requires measurements with a neutron target. Some neutron data exist, mostly extrapolated from deuteron measurements, but the data are sparse and the systematic uncertainties are large. However, the same linear combination of $A^{(0)}$ and $A^{(1)}$ contributes to the $\pi^0 p$ and $\pi^+ n$ proton channels (with a different linear combination contributing to the neutron channels). If we define the net proton isospin 1/2 amplitude as

$$A_p^{(1/2)}=\left[A^{(0)}+\frac{1}{3}A^{(1)}\right], \tag{18}$$

then proton data alone are sufficient to determine $A_p^{(1/2)}$ and $A_P^{(3/2)}$. For the sake of accuracy in extracting the physically interesting $\tau=3/2$ multipoles associated with the $N\to\Delta$ transition, $M_{1+}^{3/2}$ and $E_{1+}^{3/2}$, it is better to restrict the multipole fits to only proton reactions. This is the approach we have taken. (This is not the approach used in several other recent multipole analyses [75,22], where neutron data have been included to extract the separate scalar and vector $\tau=1/2$ amplitudes. While this provides a more global description of all π-production channels, there remains an additional as yet

TABLE IX. Compilation of data included in the multipole analyses of this work. The total number of data points is 747. The systematic scale uncertainties of the data sets are listed in the second last column and the fitted normalization scales for solution $f3$ ($f4$) of Table X are shown in the last column.

Observable	E_γ (MeV)	Source	Scale uncertainty (σ_{f_i})	Fitted normalization (f_i)
$\gamma p \rightarrow \pi^0 p$:				
$d\sigma/d\Omega$	213-334	LEGS/this work	2.0%	0.982(0.981)±0.018
Σ	213-334	LEGS/this work		
Σ	244-314	LEGS [17]		
T	280-350	Kharkov [62]		
T	303-345	Bonn [81]		
P	280-350	Kharkov [62]		
$\gamma p \rightarrow \pi^+ n$:				
$d\sigma/d\Omega$	213-322	LEGS/this work	2.0%	0.982(0.981)±0.018
Σ	213-334	LEGS/this work		
T	280-340	Kharkov [64]	9.0%	1.017(1.003)±0.015
T	282-345	Bonn [80]		
P	280-340	Kharkov [64]	9.0%	1.017(1.003)±0.015
H	320-350	Kharkov [82]		
H	320	Kharkov [82]		
G	320-350	Kharkov [82]		
$\gamma p \rightarrow \gamma p$:				
$d\sigma/d\Omega$	213-334	LEGS/this work	2.0%	0.982(0.981)±0.018
$d\sigma/d\Omega$	207-339	Mainz [41]	4.4%	1.058(1.022)±0.021
$d\sigma/d\Omega$	250-349	Mainz [40]	5.0%	0.997(0.959)±0.018
$d\sigma/d\Omega$	149-286	SAL [59]	3.8%	1.039(1.025)±0.014
$d\sigma/d\Omega$	73-145	SAL [8]	4.0%	1.062(1.067)±0.019
$d\sigma/d\Omega$	98-132	MPI [83]	4.3%, 6.4%	*combined* [a]
$d\sigma/d\Omega$	81-110	Moscow [84]	8.0%	0.976(0.989)±0.022
$d\sigma/d\Omega$	33-81	Illinois [85]	2.0%	0.992(0.999)±0.020
Σ	213-334	LEGS/this work		

[a]The two data points from the [83] experiment do not have a common scale uncertainty, so their systematic errors were simply combined in quadrature.

unestimated uncertainty in their $\tau = 3/2$ multipoles due to the inclusion of neutron data in the fitting process.)

Many different observables are needed to constrain the pion multipoles. The data included in our analysis are summarized in Table IX. Because of the differences in (γ,π) cross section scales evident in Fig. 44, we have fitted only (γ,π^0) and (γ,π^+) cross sections from the present experiment (Tables IV and VI), and augmented our beam asymmetry data (Tables V and VII) with other published polarization *ratios* (in which systematic errors largely cancel). These include our earlier $\Sigma(\pi^0)$ data [17], $[T(\pi^0), T(\pi^+)]$ data from Bonn [80,81], $[T(\pi^0), P(\pi^0), T(\pi^+), P(\pi^+)]$ data from Khar'kov [62,64], and the few beam-target asymmetry points $[H(\pi^+), G(\pi^+)]$ from Khar'kov [82]. For photon scattering, there is good agreement among all modern Compton data and, together with our own results (Tables II and III) we have included in the multipole fits cross sections below 350 MeV from [40,41,59,8,83–85].

Some data points from the references of Table IX have been excluded from our fits, the most puzzling being the low energy Bonn target asymmetries $[T(\pi^+)$ for $E_\gamma = 220$, 241 and 262 MeV] and $[T(\pi^0)$ for $E_\gamma = 272$ MeV] from [80,81]. Fits to these T points, including only beam asymmetries (Σ) and leaving the cross sections completely unconstrained, are unable to reproduce these results. We conclude that there must be some problem with the low energy portion of the Bonn target asymmetry data. We have also excluded the Khar'kov beam asymmetry results from [62,64] since, while they are generally consistent with our own Σ data, their errors are 3 to 4 times larger and thus do not provide a useful constraint. For Compton scattering, the $\sim 150°$ Moscow results [84] have been shown to be inconsistent with other measurements [8], and so we have included only their $\sim 90°$ data. Finally, the recent Mainz Compton measurements at 130.7° lab [42] became available only after our analysis was completed, and are not included in the fit. In any case, these points would have negligible impact owing to their large errors (lower panel of Fig. 38).

The total number of data points included in our analysis is 747, of which 232 are from $\gamma p \rightarrow \pi^0 p$, 278 are from $\gamma p \rightarrow \pi^+ n$ and 237 are from $\gamma p \rightarrow \gamma p$. There are four main observables in the π-production data base: $d\sigma/d\Omega$ (158 points), Σ (186 points), T (108 points), and P (48 points), as well as a few isolated double-polarization asymmetries, H (7

points) and G (3 points). The Compton scattering data is limited to two observables: $d\sigma/d\Omega$ (158 points) and Σ (79 points). Thus there is a roughly even distribution among the different observables and no single observable dominates.

D. Fitting procedure

Starting with the test fit that reproduced the GW[SM95] solution (Sec. VII A) for the $A_p^{(1/2)}$ and $A_p^{(3/2)}$ multipoles of Eqs. (17) and (18), the parameters in Eqs. (12) to (16) were varied to minimize the χ^2 formed by comparing predictions with the data base of Table IX.

When combining data from different experiments, systematic uncertainties cannot be ignored. One simple method that has been used in past analyses is to add such an error in quadrature with the statistical uncertainties [86,87]. However, systematic errors represent uncertainties in normalization scales that are generally not a function of angle. Adding them in quadrature with the statistical component ignores very significant correlations and underestimates the uncertainties. The correct procedure is to let the fit determine relative normalization scales among the data sets. All of the cross section data sets of Table IX, and several of the polarization asymmetry data sets, have such systematic scale uncertainties. We have followed the procedure of [88], multiplying all data from a set with a systematic scale error (σ_f) by a common factor (f) while adding $(f-1)^2/\sigma_f^2$ to the χ^2. Specifically, our fitting procedure minimizes the following function:

$$\chi^2=\sum_{i=1}^{N_s}\left\{\sum_{j=1}^{N_i}\left(\frac{f_i x_{ij}^{exp}-x_{ij}^{fit}(\vec{\mathfrak{s}})}{f_i\sigma_{x_{ij}}}\right)^2+\left(\frac{f_i-1}{\sigma_{f_i}}\right)^2\right\}, \quad (19)$$

where N_s is the number of independent data sets, each having N_i points. x_{ij}^{exp} and $\sigma_{x_{ij}}$ are the jth experimental datum from the ith data set and its associated measurement error, respectively, $x_{ij}^{fit}(\vec{\mathfrak{s}})$ is the value predicted from the $\vec{\mathfrak{s}}$ parameter set, and f_i is the global scale parameter associated with the ith data set. The last term in Eq. (19) weights the penalty for choosing a normalization scale different from unity by the systematic uncertainty of the measurement. For some of the polarization data the effects of systematic uncertainties are more complicated than a simple scale shift and for these the statistical and systematic errors have already been reported as a combined net uncertainty. For such sets we fix $f_i=1$.

The procedure of Eq. (19) for accounting for systematic uncertainties is not unique. The GW/SAID group uses a very similar algorithm [75], and others were used in multipole analyses carried out in the 1970s. However, multipole analyses have recently been reported by groups from RPI and Mainz in which systematic scale uncertainties have simply been ignored [76,22]. This associates an unphysical level of accuracy with the data being analyzed and necessarily results in as yet unestimated errors in their reported results.

Two computer codes were used to determine the fit parameters by minimizing χ^2 in the above expression, MINUIT [89] from the CERN Program Library and E04FDF from the NAG Library [90]. These are distinct packages that use completely different algorithms to minimize a function. Tests using these two packages on the same data yielded results that differed by no more than 0.001%.

Ideally, one would like to vary all parameters simultaneously in one *grand fit*. However, this can lead to unphysical solutions arising from the ambiguities associated with incomplete sets of observables, and past analyses have generally varied parameters in stages [72,91,92]. In our work we have found that a *grand fit* yields several normalization scales that differ from unity by significantly more than the systematic scale errors associated with the measurements. In contrast, if either (a) the (γ,π) data is first fit and the resulting normalization scales are fixed before including (γ,γ) data in a subsequent fit, or the converse (b) the (γ,γ) data is used to fix their normalization scales before expanding the fit to include (γ,π) data, then all fitted normalization scales are consistent with expected systematic uncertainties. The reduced-χ^2 values for a *grand fit* compared to those of procedures (a) or (b) differ by trivial amounts (± 0.031 out of 1.535), and simply indicate the presence of multiple minima which occur because the data base has less than a complete set of observables. Both procedures (a) and (b) yield physically meaningful normalization scales, and in fact nearly equivalent results in all fitted parameters. We report here results obtained following procedure (b) since the Compton data measured in different laboratories are all in agreement.

With the normalization scales being fitted, the error computed from the covariance matrix on all fitted quantities inherently includes both statistical and systematic components. However, this alone is not the total uncertainty. The full variance associated with a quantity P having a *standard deviation* σ_P resulting from a fit to n points with k parameters is given by

$$s_P^2=\frac{\chi^2}{n-k}\sigma_P^2=\chi_{df}^2\sigma_P^2. \quad (20)$$

The quantity s_P is formally referred to as the *unbiased estimate uncertainty* or *estimated standard error* [93]. In other words, the total uncertainty is actually larger by the square-root of the reduced-χ^2. The point is best made with an extreme example. If two measurements reporting values of 1.0 ± 0.1 and -1.0 ± 0.1 are fitted to a constant, MINUIT will return their weighted mean, 0.00 ± 0.07. But the uncertainty on the observable from these measurements is clearly much larger than ± 0.07. The problem here is that the function assumed in the fit (a constant) was inappropriate. This is reflected in the large reduced-χ^2 value of 14.14, and results in a total *unbiased estimate uncertainty* of $s_P=\pm 1.00$ which is intuitively reasonable. (The E04FDF code from the NAG Library returns *unbiased estimate uncertainties* while the errors returned by MINUIT must be multiplied by $\sqrt{\chi^2_{df}}$.) All fitted errors quoted in this work are total *unbiased estimate uncertainties*. The errors reported from other recent analyses by the GW/SAID and RPI groups [75,76] are not and should be multiplied by the square-root of their associated reduced-χ^2 values.

TABLE X. Energy range for the data of Table IX included in the multipole fits.

Solution	$p(\gamma,\pi)$ range	$p(\gamma,\gamma)$ range	χ^2_{df}
$f2$ [21]	200–350 MeV	200–350 MeV	977/(644-34)=1.634
$f3$ (this work)	200–350 MeV	33–350 MeV	1126/(747-36)=1.583
$f4$ (this work)	200–350 MeV	33–309 MeV	983/(694-36)=1.494

E. Multipole solution

We have carried out a large number of multipole fits to the data of Table IX but will restrict most of the discussion to the three summarized in Table X. These differ in the energy range of the Compton data included in the χ^2 minimization. The first entry, solution $f2$, reported in [21], did not fit Compton data below 200 MeV and excluded comparisons with the last 4 cross section entries of Table IX. In fit $f3$ we have expanded the Compton data to low energies in order to increase the t-range for the fit of the asymptotic A_i^{as} components in Eq. (13). Most of the subsequent discussion is focused on fit $f3$. The fit $f4$ restricts the Compton data to energies below the $(\gamma,2\pi)$ threshold in order to minimize uncertainties in the extraction of polarizabilities. (The $f3$ and $f4$ solutions are very close to the ones used to produce the results listed in the third and first rows in Table I of [9], respectively. The differences are very small and result from iterating the procedure used to fit cross section scales and from the inclusion of a few additional high energy points.) The $\chi^2{}_{df}$ for all the solutions of Table X are comparable.

The fitted normalization scales for solution $f3$ (and $f4$) are listed in the last column of Table IX, together with the systematic scale uncertainties associated with the data sets (fourth column). The fitted scale factors are close to unity, with the largest deviations being less than 1.5 standard deviations of their associated systematic scale errors. We note that the fitted scales for the two Mainz Compton measurements of [40,41] differ by about 6%, confirming a similar result reported in [41]. The 180° Compton experiment of [83] reported the cross section at two energies, but with uncorrelated systematic uncertainties. We have therefore combined their systematic and statistical errors in quadrature since there was no common scale factor to fit. The polarization asymmetry data represent ratios of cross sections in which systematic effects largely cancel. Asymmetry results have generally been quoted with residual systematic errors propagated through to a net uncertainty. The one exception is the T and P measurements from Khar'kov [64] which have a 9% scale error due to target polarization uncertainties, and this scale we have also fitted.

The electric and magnetic pion multipoles are plotted as a function of beam energy in Fig. 45 and Fig. 46 where pairs of solid lines denote the *unbiased estimate uncertainty* bands. For comparison, we have also plotted the GW[SM95] solution from [75] as open diamonds, and the unitarized pseudovector pion-Born amplitude as open squares. The largest multipole is of course the $M_{1+}^{3/2}$ which displays the characteristic Δ resonance behavior with the real part crossing zero at $\sim$340 MeV, where the P_{33} πN-phase passes through 90°, and the imaginary part peaking near this energy. Our fitted $M_{1+}^{3/2}$ is essentially indistinguishable from that of the GW[SM95] solution from [75]. After this, the next most prominent multipoles are the $E_{0+}^{1/2}$ and $E_{0+}^{3/2}$ for which our solution is actually closer to the Born values over most of the fitted energy range and show a departure only over $(\gamma,2\pi)$ threshold. The largest D-wave multipoles are the $E_{2-}^{1/2}$ and $E_{2-}^{3/2}$. For these, our solution is consistent with the Born amplitudes, while the GW[SM95] solution is significantly different in the $E_{2-}^{1/2}$. In contrast, many of the smaller D-waves deviate somewhat from both Born and GW[SM95]. Most of the F-wave multipoles are consistent with Born values, although the uncertainty bands are certainly largest for these. (Since the phases of the $E_{3-}^{3/2}$, $E_{3+}^{1/2}$, $M_{3-}^{3/2}$ and $M_{3+}^{1/2}$ multipoles are indistinguishable from zero, their imaginary parts have been set to zero.)

The Compton helicity amplitudes of Eq. (13) depend upon both t and the energy parameter $\nu=(s-u)/4M_p$. The t range of the data being fit is relatively small, $-t<0.2$ $(\mathrm{GeV}/c)^2$. In Fig. 47 we plot the six Compton helicity amplitudes at $t=0$, with ν varying over the range of the integrals in Eq. (13). The (purely real) s- and u-channel Compton-Born terms are shown as dotted curves. The contributions of the integrals in Eq. (13) to the real parts are plotted as solid curves from 0 to 1.5 GeV, and the corresponding imaginary parts are shown as the dashed curves. The asymptotic parts from Eqs. (15b), (16b), and (14) are ν-independent and are indicated by the horizontal lines extending to 1.75 GeV in the A_1, A_2, and A_6 amplitudes, respectively. The t-channel π^0 and η^0 contributions, $A_2^{\pi^0}+A_2^{\eta^0}$ in Eq. (16c), contribute only to the A_2 amplitude. This essentially-*Born* component is also ν-independent and is shown as the other horizontal line in the upper-right panel. Thus for A_2, the full real part is the sum of the dotted and three solid curves. For all but A_2, most of the amplitude strength is in the vicinity of the Δ resonance. As expected the A_3, A_4, and A_5 amplitudes converge rapidly, and A_6 has only a small component beyond 1.5 GeV.

The general features of the A_i amplitudes shown in Fig. 47 persist throughout the t range of the present analysis. We illustrate the behavior of the total Compton amplitude with the special case of $t=0$ for which there are important limits. At exactly $t=0$, corresponding to 0° scattering, kinematic factors suppress the A_1, A_2 and A_5 helicity amplitudes so that the total *forward* c.m. amplitude reduces to

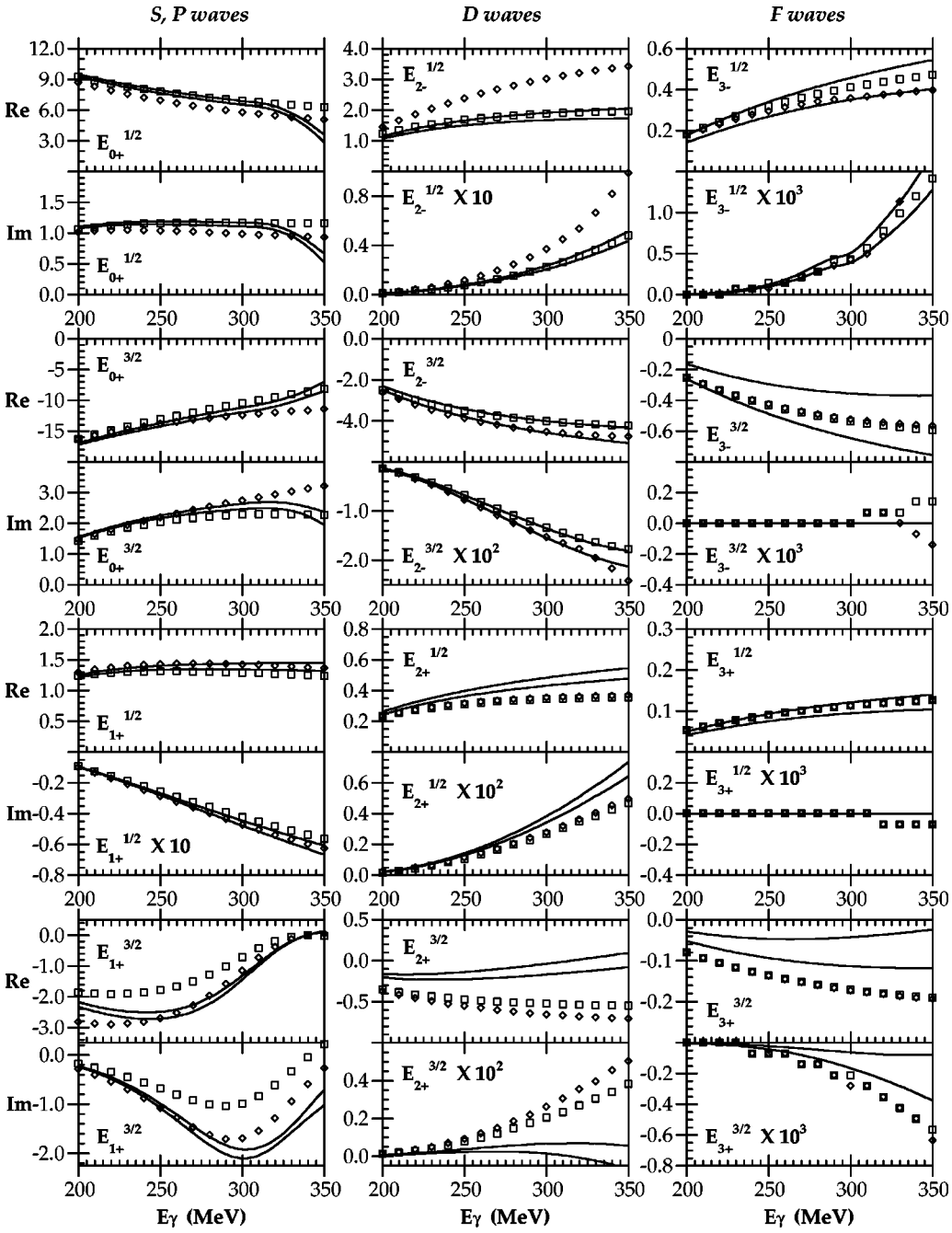

FIG. 45. The real and imaginary parts of the electric photo-pion multipoles ($E^{\tau}_{l\pm}$) from solution $f3$ (Table X), in units of $10^{-3}/M_{\pi^+}$ MeV^{-1}, are shown as a function of beam energy in sets of top and bottom panels, respectively, as pairs of solid curves indicating the *unbiased estimate uncertainty* bands. Also plotted for comparison are the GW[SM95] solution from [75] as open diamonds, and the unitarized pseudovector Born components as open squares. The contributions of S and P, D, and F πN-partial waves are organized into the left, middle, and right columns, respectively.

$$\frac{1}{8\pi\sqrt{s}}T_{fi}(0) = \frac{E_\gamma^2 M}{2\pi\sqrt{s}}\left\{-(A_3+A_6)\varepsilon'\cdot\varepsilon + i\frac{E_\gamma}{M}A_4\sigma\cdot(\varepsilon'\times\varepsilon)\right\}, \tag{21a}$$

where ε and ε' are the initial and final photon polarization vectors, σ is the target spinor and $s=M(2E_\gamma+M)$ is the square of the total c.m. energy. This displays the familiar form of the Gell-Mann–Goldberger–Thirring forward Compton amplitude [94],

$$\frac{1}{8\pi\sqrt{s}}T_{fi}(0) = f_1(E_\gamma)\varepsilon'\cdot\varepsilon + i f_2(E_\gamma)\sigma\cdot(\varepsilon'\times\varepsilon), \tag{21b}$$

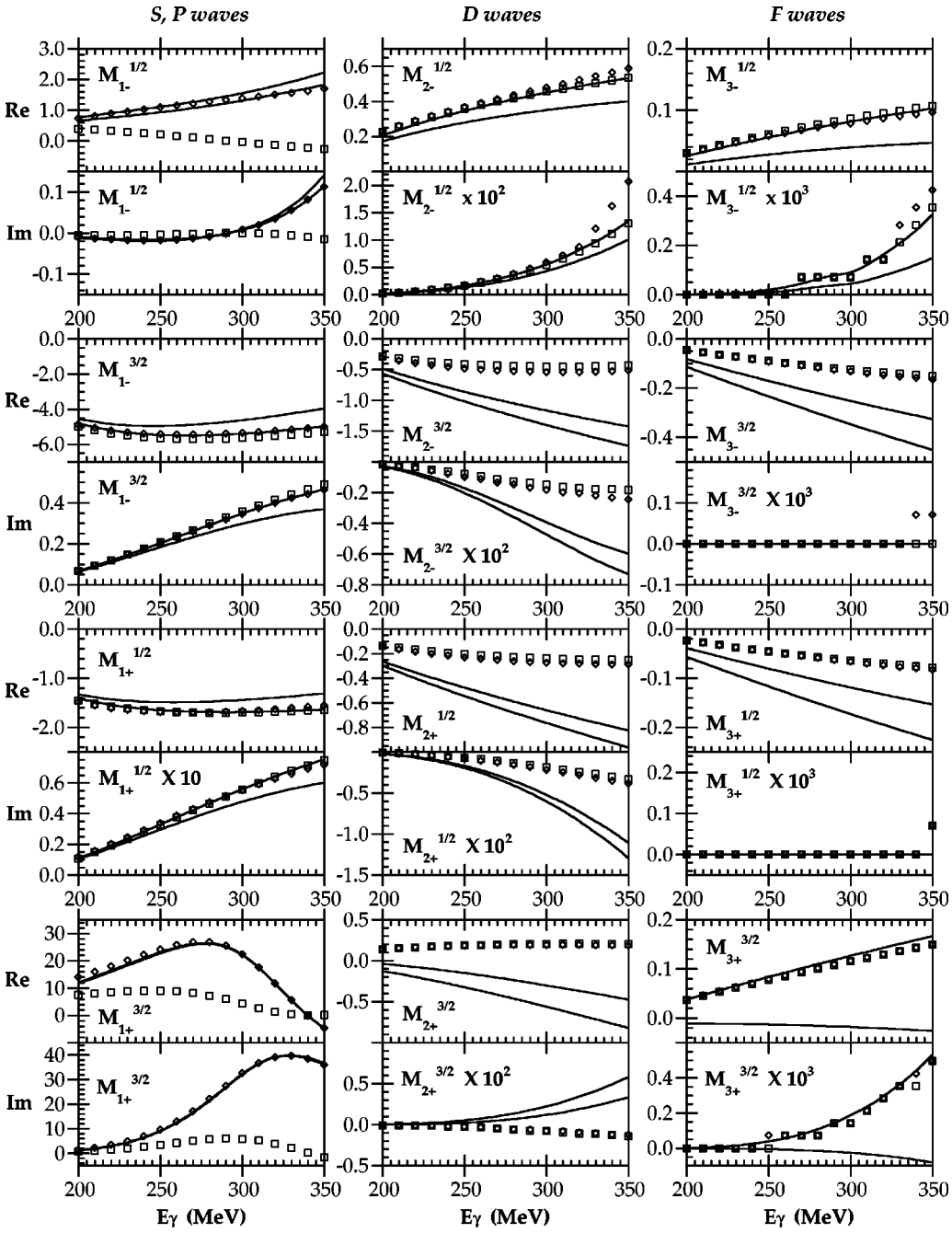

FIG. 46. The real and imaginary parts of the magnetic photo-pion multipoles ($M_{l\pm}^{I}$) from solution $f3$ (Table X), in units of $10^{-3}/M_{\pi^+}$ MeV^{-1}, are shown as a function of beam energy in sets of top and bottom panels, respectively, as pairs of solid curves indicating the *unbiased estimate uncertainty* bands. Also plotted for comparison are the GW[SM95] solution from [75] as open diamonds, and the unitarized pseudovector Born components as open squares. The contributions of *S* and *P*, *D*, and *F* πN-partial waves are organized into the left, middle, and right columns, respectively.

and the forward cross section, averaged over the spin states of an unpolarized target, is just the sum $d\sigma/d\Omega_{\text{c.m.}}(0^\circ) = |f_1|^2 + |f_2|^2$.

The forward amplitudes f_1 and f_2 are shown for the $f3$ multipole solution in Fig. 48 as solid curves for the real parts, and dashed curves for the imaginary parts, respectively. These provide several benchmarks. The amplitudes exhibit the expected resonance behavior with real parts crossing zero, and imaginary parts peaking at the delta resonance. The dashed curve in the upper panel in fact just reflects the total π-production cross section since the imaginary part of f_1 is determined by the *optical* theorem, Im $f_1 = E_\gamma \sigma_T / 4\pi$. The Re f_1 satisfies the Kramers-Kronig relation [95,96], which is guaranteed by the form of the dispersion integral in Eq. (13), and the value of Re f_1 at zero energy is just the Thomson limit of $-e^2/M$. With the assumption that $f_2(\infty)$ vanishes, a dispersion relation for Re f_2 results in the Gerasimov-Drell-Hearn (GDH) sum rule [94,95,97]; but

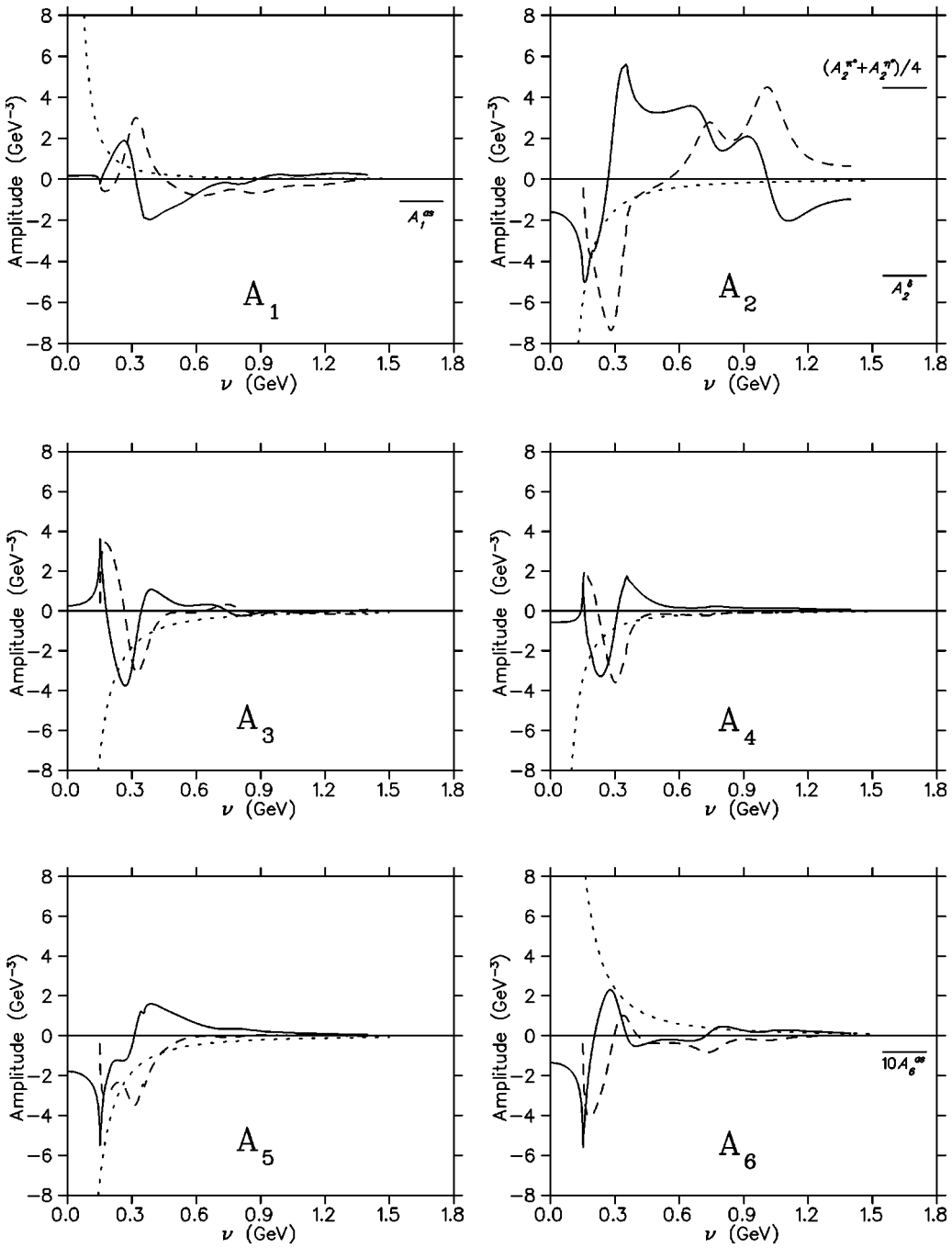

FIG. 47. Compton helicity amplitudes for $t=0$ as a function of $\nu=(s-u)/4M_p$ over the range of the integrals in Eq. (13) for solution $f3$ (Table X). Integral parts of Re(A_i) are shown as solid curves and Im(A_i) as dashed curves. The *s*- and *u*-channel Born contributions are given as dotted curves, and the *t*-channel π^0 and η^0 contributions, $A_2^{\pi^0}+A_2^{\eta^0}$, as the indicated horizontal line in the upper-right panel. The asymptotic ν-independent components A_1^{as}, A_2^{δ}, and A_6^{as} are also shown.

tests of this sum rule, or equivalently of the assumption that $f_2(\infty)=0$, are still at an early stage. A unitarity cusp, due to the opening of the πN channel, appears in both forward amplitudes at 150 MeV. Kinks are evident in the curves at 350 MeV due to the discontinuous jump between our fitted pion multipoles and the GW[SM95] solution that is used to extend the integration in Eq. (13) to higher energies. We have tested the effect of smoothing out these jumps in the pion multipoles with various algorithms. Although the 350 MeV kinks in the Compton amplitudes can be eliminated, there are no discernible changes to any of the predicted observables below 350 MeV.

The quality of the $f3$ solution is illustrated by comparing the predictions of our multipoles with π-production cross sections and beam asymmetries in Fig. 49, with Compton cross sections and beam asymmetries in Fig. 50, and with π-production T and P asymmetries in Fig. 51. The solid curves are the *unbiased estimate uncertainty* bands generated

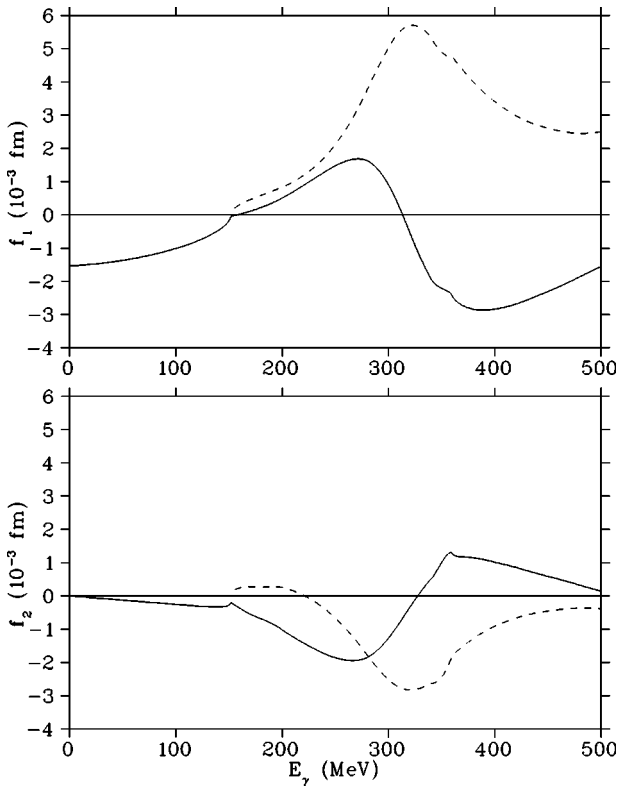

FIG. 48. Forward Compton amplitudes f_1 and f_2 of Eq. (21b) for multipole solution $f3$ (Table X). Real parts are shown as solid curves and imaginary parts as dashed curves.

from the $f3$ fit.

In Fig. 52 we plot the $f3$ predictions for the angle-integrated π^+ cross sections (top panel) and total pion-photoproduction cross sections (bottom panel). These are compared to the π^+ data of Table VIII, which was not used in the fit to avoid double counting, and to previous results from Tokyo [63], Mainz [98], Bonn [66], and Daresbury [99]. (The difference between the $f3$ predictions and the Mainz/Bonn total cross sections appears less than the 10% suggested by Fig. 44 because of their higher π^+ results at forward and backward angles.)

VIII. $N \rightarrow \Delta$ PROPERTIES

The *s*-channel excitations of the isospin $\tau = 3/2$ Δ resonance contribute to the $M_{1+}^{3/2}$ and $E_{1+}^{3/2}$ photo-pion multipoles. The imaginary parts of these are shown in Fig. 53 by the solid curves which denote the *unbiased estimate uncertainty* bands (labeled *LEGS* in the legend). For comparison, we have also plotted the GW[SM95] and GW[SP97k] multipoles from [75] as the dotted and dash-dotted curves, respectively. The dotted-GW[SM95] curve in the upper $M_{1+}^{3/2}$ panel is underneath the solid lines and is essentially invisible. While this is clearly in very good agreement with our own solution, the newer GW[SP97k] solution appears shifted slightly to lower energies. The Mainz solution of [22], labeled *HDT* in the legend and indicated by the circles, is about 2.2% lower than our $M_{1+}^{3/2}$ at the Δ peak but in good agreement at lower energies. The resonance position of 1232 MeV total energy where the P_{33} πN-scattering phase goes through 90° ($E_\gamma = 339.6$ MeV for the GW[SM95] $T_{\pi N}$ matrix), is indicated. This is about 20 MeV higher than the pole position where the $M_{1+}^{3/2}$ peaks [20].

Differences are more apparent in the $E_{1+}^{3/2}$ multipole. The HDT/Mainz solution is somewhat smaller than our multipole below the resonance position, but increases to meet our uncertainty band at 340 MeV. The GW/SAID solutions are both smaller than either the LEGS or HDT multipoles.

A quantity of considerable interest is the *EMR* ratio of the $E2$ to $M1$ $N \rightarrow \Delta$ transition strengths. This is determined from the resonant parts of the $M_{1+}^{3/2}$ and $E_{1+}^{3/2}$ multipoles and, since their $T_{\pi N}^{l=1}$ matrix elements in Eq. (12) are the same, this is just the ratio of the corresponding fitted β coefficients,

$$EMR = \beta[E_{1+}^{3/2}]/\beta[M_{1+}^{3/2}], \tag{22a}$$

or $EMR = -(3.07 \pm 0.26)\%$ for the $f3$ multipole solution.

The ratio of the $E2/M1$ $N \rightarrow \Delta$ transitions provides an important discrimination between nucleon structure models. The quantity most frequently compared to model calculations is the ratio of the corresponding photopion multipoles,

$$R_{EM}^{3/2} = \frac{\mathrm{Re}\,[E_{1+}^{3/2}(M_{1+}^{3/2})^*]}{|M_{1+}^{3/2}|^2}. \tag{22b}$$

The evolution of this quantity with energy is shown in Fig. 54 as dotted lines. For comparison, we also show this ratio constructed from the *non-Born* parts of the multipoles (dashed curves), and from only their resonant parts (solid lines). The latter is just the ratio in Eq. (22a) and is independent of energy. From this one sees that the background terms represented by the α_i in Eq. (12) have an appreciable effect and are comparable to the *Born* contributions. At the energy where the P_{33} πN-scattering phase crosses 90°, the point where all the curves cross in Fig. 54, the real part of $M_{1+}^{3/2}$ goes to zero and Eq. (22b) reduces to

$$R_{EM}^{3/2} = \frac{\mathrm{Im}\,[E_{1+}^{3/2}]}{\mathrm{Im}\,[M_{1+}^{3/2}]}, \tag{22c}$$

which from our multipoles takes the value $-(3.04 \pm 0.27)\%$. The small difference between this and the -3.07% value constructed from the purely resonant parts of the multipoles reflects the inelasticity of the T matrix in Eq. (12) which is very small since the resonance position is only slightly above the $(\gamma, 2\pi)$ threshold.

Sensitivity to the EMR enters the analysis chiefly through the π-production data. Near the Δ peak, the 90° π^0 cross section measured with the photon polarization parallel to the reaction plane, $\sigma_\parallel^{\pi^0}$, changes by about 5% for each percent variation in the EMR, while the perpendicular cross section, $\sigma_\perp^{\pi^0}$, is completely insensitive except at extreme angles near 0° and 180° [17]. This is illustrated in Fig. 55 with data at 322 MeV beam energy. Here the solid curves are the predictions of the $f3$ multipole solution (Table X) and the dashed and dotted curves are obtained by scaling the $E2$ $N \rightarrow \Delta$

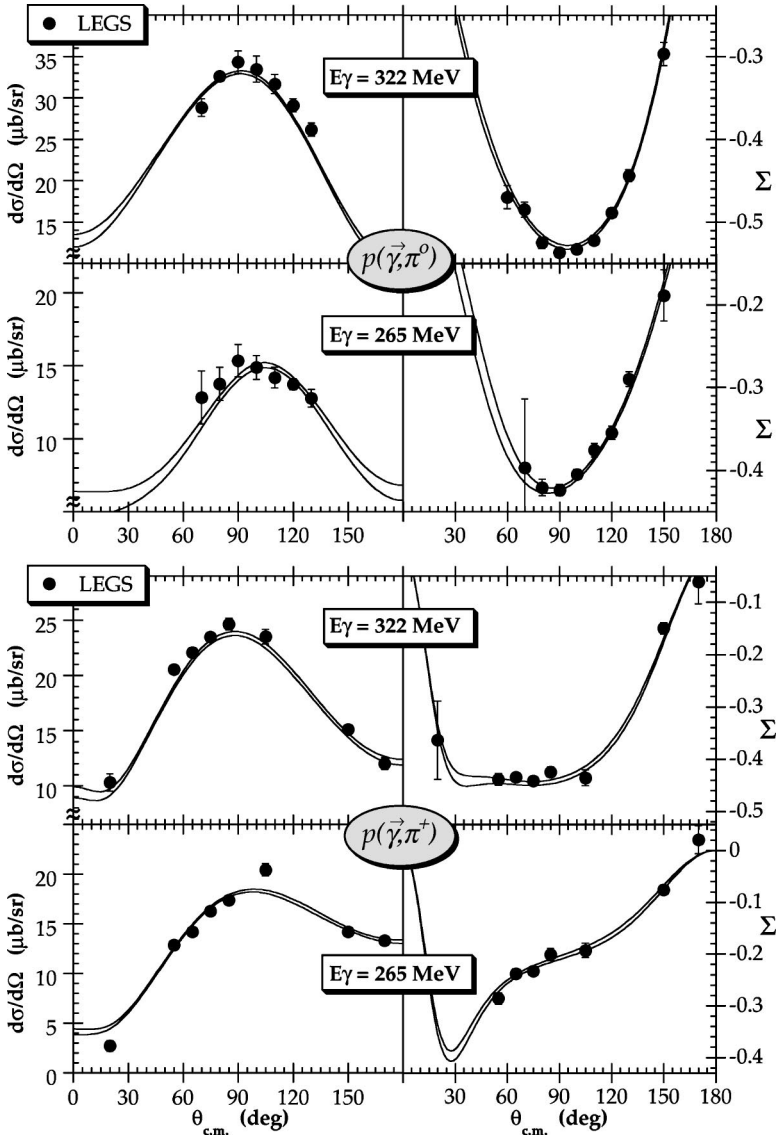

FIG. 49. Predictions from multipole fit $f3$ (Table X) shown as *unbiased estimate uncertainty* bands compared to a sample of the $p(\gamma,\pi^0)$ data base, upper-four panels, and the $p(\gamma,\pi^+)$ data base, lower-four panels, of Table IX. For this comparison, the data have been scaled by the fitted normalization factor of Table IX (last column).

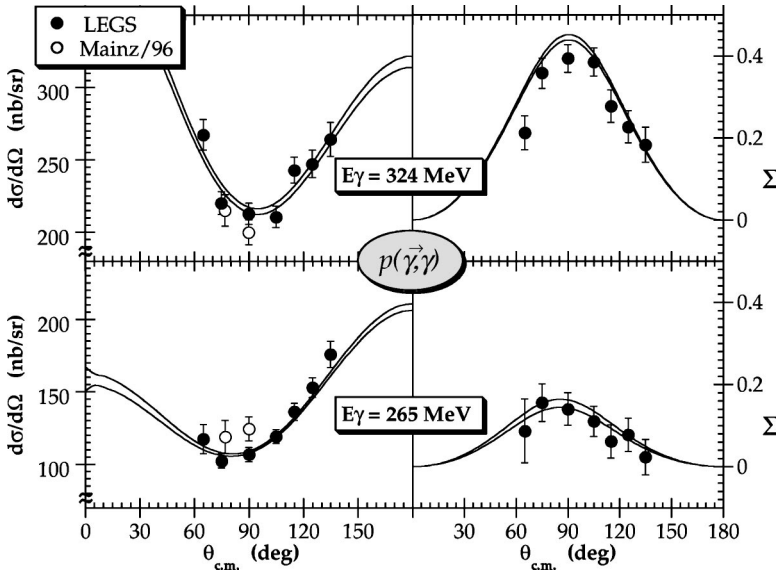

FIG. 50. Predictions from multipole fit $f3$ (Table X) shown as *unbiased estimate uncertainty* bands compared to a sample of the $p(\gamma,\gamma)$ data base of Table IX. For this comparison, the data have been scaled by the fitted normalization factors of Table IX (last column).

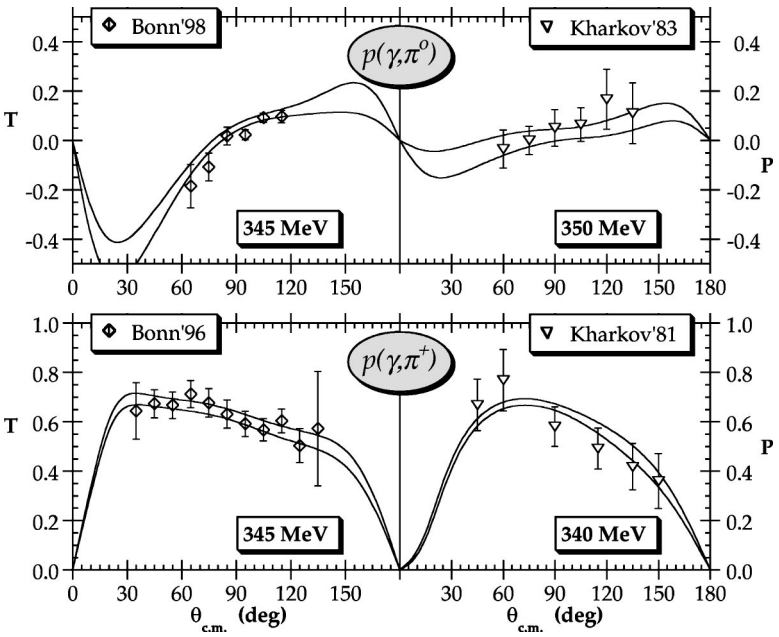

FIG. 51. Predictions from multipole fit $f3$ (Table X) shown as *unbiased estimate uncertainty* bands compared to a sample of the T (left panels) and P (right panels) data base (Table IX) for $p(\gamma,\pi^0)$, top graphs, and $p(\gamma,\pi^+)$, bottom graphs. For this comparison, the data have been scaled by the fitted normalization factor of Table IX (last column).

resonant component, $\beta[E_{1+}^{3/2}]$ in Eq. (12), by factors of two and zero, respectively. (It is important to scale only the resonant $E2$ component for this comparison. Larger apparent sensitivities can be generated, for example by zeroing the full $E_{1+}^{3/2}$ multipole, but such exercises are unrealistic since Born and other nonresonant backgrounds are significant.) Similar sensitivities occur in π^+ production, with $\sigma_{\parallel}^{\pi^+}(90°)$ changing by about 3.5% for each percent variation in the EMR while $\sigma_{\perp}^{\pi^+}$ remains essentially constant. These sensitivities in $\sigma_{\parallel}$ are significant, although their effectiveness is somewhat diminished by systematic uncertainties. However, this shortcoming is circumvented in the ratio of $\sigma_{\parallel}$ to the

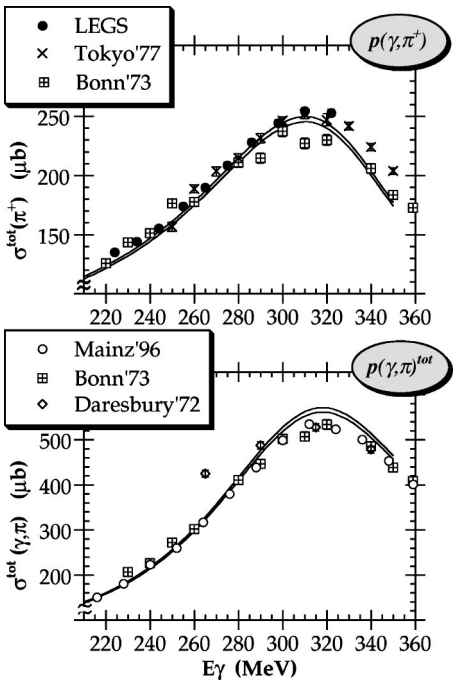

FIG. 52. Predictions from multipole fit $f3$ of Table X for total $p(\gamma,\pi^+)$ cross sections (top panel) and for the sum of π^0 and π^+ photoproduction channels (bottom panel), shown as *unbiased estimate uncertainty* bands. These are compared to the data of Table VIII for π^+, which for this comparison have been multiplied by the fitted scale factor from Table IX, and to previous $\sigma(\pi^+)$ results from [63,66]. The total photo-pion cross sections are compared to the results from [98,66,99].

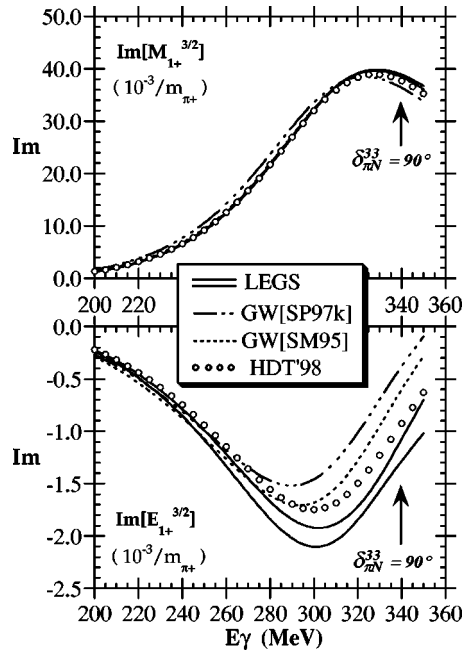

FIG. 53. Imaginary parts of the $M_{1+}^{3/2}$ and $E_{1+}^{3/2}$ photopion multipoles. The *unbiased estimate uncertainty* bands for multipole solution $f3$ (Table X) are plotted as pairs of solid lines. For comparison, the GW[SM95] and GW[SP97k] multipoles from [75] are shown as the dotted and dash-dotted curves, respectively, and the Mainz solution of [22] is indicated by the circles. The Δ resonance position where the P_{33} πN phase crosses 90° is indicated.

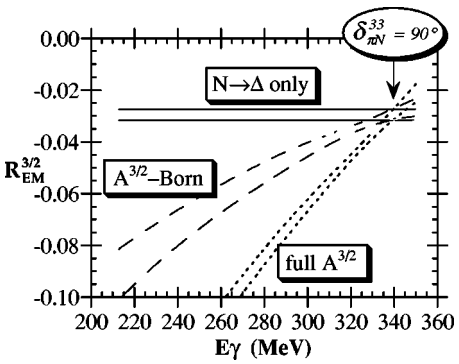

FIG. 54. Evolution of the quantity $R^{3/2}_{EM}$ from Eq. (22b) with energy, using multipoles from solution $f3$ (Table X). The dotted lines show the uncertainty band for the ratio constructed from the full fitted $E^{3/2}_{1+}$ and $M^{3/2}_{1+}$ multipoles, the dashed lines are constructed from their *non-Born* parts, and the solid lines from only their resonant parts. The energy at which the P_{33} πN phase crosses 90° is indicated.

EMR-independent $\sigma_\perp$, or equivalently in the beam asymmetry, Σ. This is plotted for both channels in Fig. 56. We have also plotted here the asymmetries recently reported from Mainz [43] as open circles. Both sets of data points include both statistical and polarization-dependent systematic uncertainties. While the two sets of π^0 data are in good agreement, the Mainz π^+ asymmetries appear shifted to more negative values, which would correspond to a smaller EMR. This is a likely source of their somewhat smaller reported EMR value [57].

Compton scattering has a positive beam asymmetry in the region of the Δ, while the Σ from π-production is negative. As a result, the sensitivity in the Compton channel is reversed with predictions for $\sigma_\perp^{\gamma\gamma}$ changing by about 3% for each percent variation in the EMR while $\sigma_\parallel^{\gamma\gamma}$ remains essentially constant, except at large angles [100]. As before, the asymmetry $\Sigma^{\gamma\gamma}$ cancels systematic uncertainties but, owing to the substantially smaller cross sections in this channel, the remaining statistical errors are significantly larger than those of $\Sigma^{\gamma\pi}$, with the result that Compton scattering provides only minor constraints on the $N\rightarrow\Delta$ EMR. The effect of the Compton data is shown in Fig. 57 where the three largest multipoles of the $f3$ solution are plotted as the solid curves with the indicated errors. Repeating the fit without inclusion of the Compton data results in the dash-dot curves. The largest change occurs in the $M^{3/2}_{1+}$ multipole near the peak of the Δ, and is quite significant. This is essentially because the $\gamma_{M1}N\Delta$ coupling appears squared in the Compton amplitude for scattering through the P_{33} Δ resonance. This confirms the sensitivity of Compton scattering to the $M^{3/2}_{1+}$ as asserted in [101], although we disagree with their conclusions, largely because of the very limited nature of their analysis in which only the $M^{3/2}_{1+}$ multipole was varied to fit a single observable at two angles. In contrast, there is essentially no discernible change in the $E^{3/2}_{1+}$ multipole. Since only the denominator of the EMR is changed with the inclusion of the Compton data, the net effect on the ratio is minor. The fit to the Compton data produces changes in a variety of other multipoles, like the $E^{3/2}_{0+}$ shown in Fig. 57, but the uncertainties are larger and the shifts are rarely more than twice the error bars.

In addition to the EMR, our multipole parametrization in Eq. (12) separates the $N\rightarrow\Delta$ resonance components and provides a direct determination of the transverse helicity amplitudes. These are given by

$$A_{1/2} = -\frac{1}{2}\{M1_{N\rightarrow\Delta} + 3E2_{N\rightarrow\Delta}\}K, \tag{23a}$$

$$A_{3/2} = -\frac{\sqrt{3}}{2}\{M1_{N\rightarrow\Delta} - E2_{N\rightarrow\Delta}\}K, \tag{23b}$$

with the $M1$ and $E2$ resonant amplitudes determined from (12) by $\beta[M^{3/2}_{1+}]$ and $\beta[E^{3/2}_{1+}]$, and the factor K is taken as [102]

$$K = \frac{1}{\hbar c}\sqrt{\frac{2}{3}}\left[\frac{4\pi q W\Gamma}{kM_p(\Gamma_\pi/\Gamma)}\right]^{1/2}. \tag{24}$$

Here, $q = 226.2$ MeV/c and $k = 258.9$ MeV/c are the c.m. π^+ and γ momenta at resonance, $W = 1232$ MeV the c.m. resonance energy, $\Gamma = 120$ MeV the resonance width, and $\Gamma_\pi/\Gamma = 0.994$ the πN branching fraction [103]. The ratio of these helicity amplitudes is simply related to the EMR of Eq. (22a), $A_{3/2}/A_{1/2} = \sqrt{3}(1-EMR)/(1+3EMR)$. For the $f3$ multipole solution, $A_{1/2} = -135.74 \pm 1.34 \times 10^{-3}$ GeV$^{-1/2}$ and $A_{3/2} = -266.90 \pm 1.62 \times 10^{-3}$ GeV$^{-1/2}$.

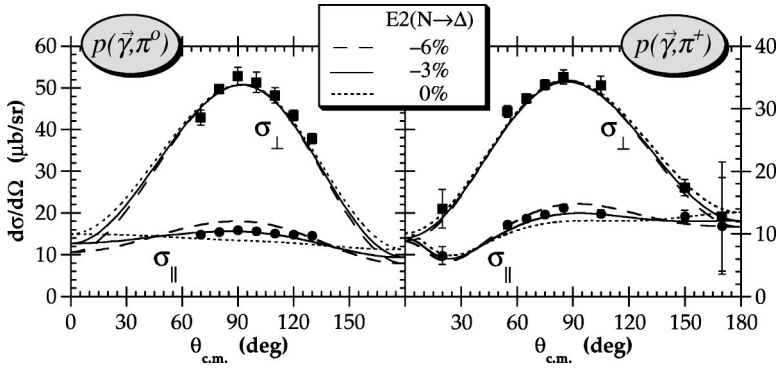

FIG. 55. Cross sections from the present work for π^0 (left panel) and π^+ production (right panel) at $E_\gamma = 322$ MeV. Data for linear photon polarizations parallel and perpendicular to the reaction plane are shown as solid circles and solid squares, respectively. Predictions of the $f3$ multipole solution (Table X) are shown as the solid curves. The dashed and dotted curves are obtained from $f3$ by scaling the E2 $N\rightarrow\Delta$ resonant component by factors of 2 and 0, respectively.

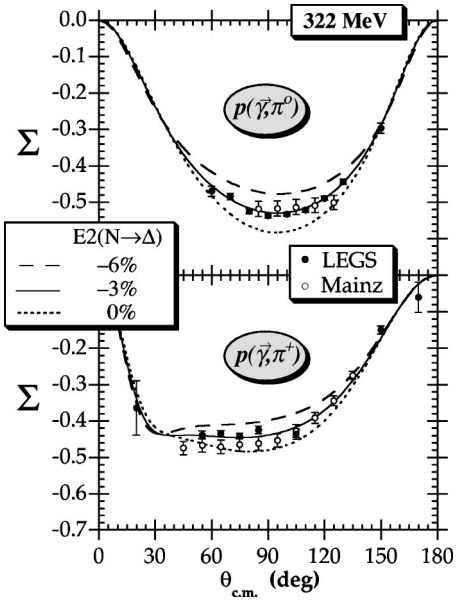

FIG. 56. Beam asymmetries near the peak of the Δ from the present work (solid circles) and from [43] (open circles) for π^0 (top) and π^+ production (bottom). Predictions of the $f3$ multipole solution (Table X) are shown as the solid curves. The dashed and dotted curves are obtained from $f3$ by scaling the $E2$ $N \rightarrow \Delta$ resonant component by 2 and 0, respectively.

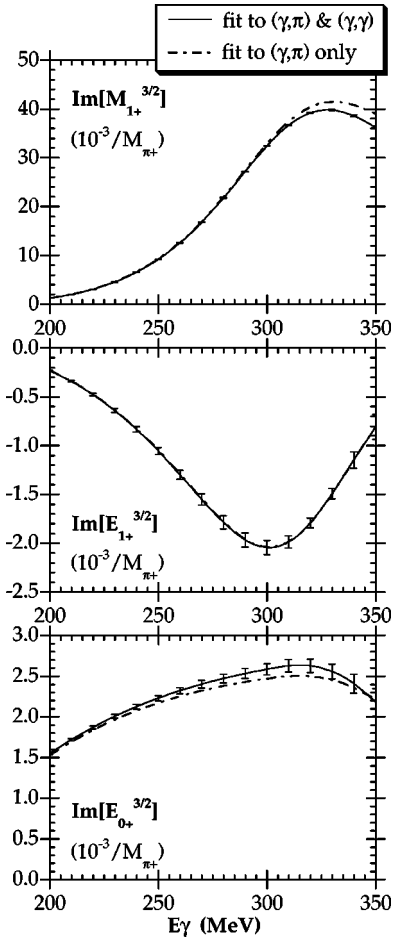

FIG. 57. The three largest multipoles of the $f3$ multipole fit to π production and Compton scattering (Table X) are shown as the solid curves, with their uncertainties indicated by the vertical bars. Repeating the fit without the Compton data results in the dash-dot curves.

A. Convergence of the multipole solution

Apart from resonance effects, cross sections for any reaction generally fall with increasing angular momentum, and this guarantees the eventual convergence of a multipole expansion of the amplitude. However, such expansions are always truncated to limit a maximum angular momentum (l_{max}) that is varied to fit the data, and ambiguities can arise when a data set lacks either sufficient statistical precision or breadth of kinematic coverage. Even when l_{max} is set at the practical limit where the uncertainties on the $l=l_{max}$ multipoles are as large as the multipoles themselves, it can still happen that some underlying physics requires a yet higher l component. In such a case, the fitting process necessarily shifts the higher l strength to lower l multipoles. This is the ambiguity pointed out by Donnachie in [26].

1. The $\hat{\Sigma}(\pi^0)/\sin^2\theta$ test for D waves

Several analyses of $p(\gamma,\pi)$ have minimized the number of fitted multipoles, limiting these essentially to S and P waves [43,22,76]. While this may yield a good representation of a data set, the solution may not be unique and others with larger values of l_{max} may be more physically meaningful. Fortunately, the linear polarization data can shed light on this question. In π production the polarization difference, $\hat{\Sigma}$ of Eq. (3e), takes the simple form

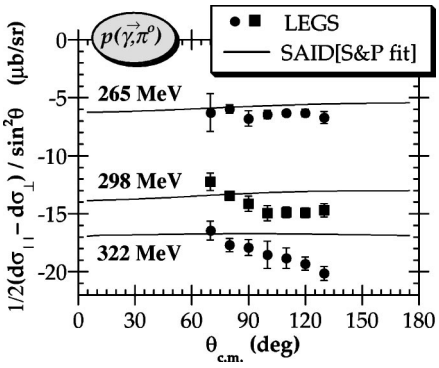

FIG. 58. The angular dependence of the polarization difference, $\hat{\Sigma}$, divided by $\sin^2(\theta)$, for the $p(\gamma,\pi^0)$ channel at three different energies. The solid curves are predictions of the GW[P500k] solution in which only S and P waves were fitted, with all other multipoles fixed at their Born values. Deviations from a constant indicate contributions from partial waves with $l \geqslant 2$.

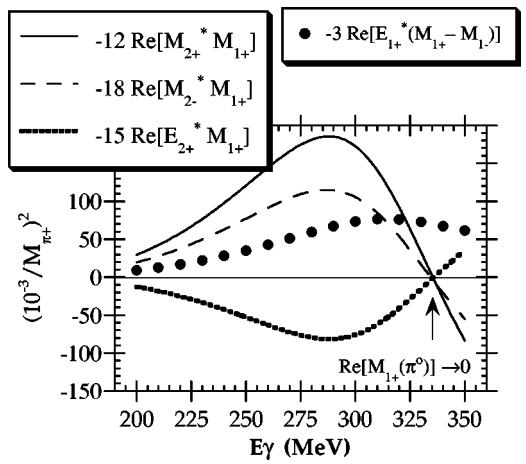

FIG. 59. The leading *D*-wave contributions from Eq. (25) to the ratio $\hat{\Sigma}(\pi^0)/\cos\theta\sin^2\theta$, computed using π^0 multipoles from the $f3$ solution (Table X), are shown as the solid, dashed, and small-dotted curves. For comparison, the leading *P*-wave $E_{1+}M_{1+}$ interference term is plotted as the series of solid circles.

$$\left(\frac{k_\gamma}{q_\pi}\right)\hat{\Sigma}=\left(\frac{k_\gamma}{q_\pi}\right)\frac{1}{2}(\sigma_\parallel-\sigma_\perp)$$
$$=-\sin^2\theta\{1.5|M_{1+}|^2+3\mathrm{Re}[E_{1+}^*(M_{1+}-M_{1-})]$$
$$+\text{other } l_\pi=0,1 \text{ terms}+\text{small } [l_\pi=0,1]$$
$$\times[l_\pi=2]\text{terms}\}_{S,P}$$
$$-\cos\theta\sin^2\theta\{12\,\mathrm{Re}[M_{2+}^*M_{1+}]$$
$$+18\,\mathrm{Re}[M_{2-}^*M_{1+}]+15\,\mathrm{Re}\,[E_{2+}^*M_{1+}]\}_D$$
$$+\text{smaller } [l_\pi=2]\text{ terms}_D+\cdots. \qquad (25)$$

Thus if only *S* and *P* waves contribute, $\hat{\Sigma}/\sin^2\theta$ must be independent of angle [104]. The *t*-channel pion-pole *Born* graph contains quite high angular momentum components, but this contributes only to the $p(\gamma,\pi^+)$ channel. In π^0 production the *Born* contributions are quite small and have very little high-*l* strength. As a result, $\hat{\Sigma}(\pi^0)/\sin^2\theta$ provides an effective test to determine if the data require extending the fitted multipoles to *D* waves. This quantity is plotted for the present LEGS data in Fig. 58. For comparison, the solid lines show the predictions of the GW/SAID[P500k] solution in which only *S* and *P* waves were varied, keeping all $l\geqslant 2$ multipoles fixed at their Born values. At all energies the curves are nearly flat, confirming the small high-*l* Born components in the π^0 channel. At sufficiently low energies the data is also nearly flat, but near the Δ resonance a definite asymmetry becomes obvious. These $\hat{\Sigma}(\pi^0)$ data can be fitted with $c_1\sin^2\theta(1+c_2\cos\theta)$ and the data require $c_2\neq 0$, indicating the presence of *D* waves beyond the mere Born levels. Two groups have recently pointed out that our asymmetry data can be fitted varying only *S* and *P* waves [105,106]. While that may be so, our $\hat{\Sigma}(\pi^0)/\sin^2\theta$ test clearly shows that non-*Born D* waves *must* contribute. To ignore them forces this *D* wave strength to artificially appear in *S* or *P* multipoles, and that can potentially alter the $N\rightarrow\Delta$ transition amplitudes of interest.

When applying the $\hat{\Sigma}(\pi^0)/\sin^2\theta$ test there is a practical limitation that must be kept clear. As indicated in Eq. (25), the leading contributions to $\hat{\Sigma}(\pi^0)$ from $l\geqslant 2$ multipoles enters through interference with the large M_{1+}. As an example, we have calculated the three $\cos\theta\sin^2\theta$ dependent terms of Eq. (25) using our π^0 multipoles, and these are plotted as the curves in Fig. 59. Away from the resonance energy these terms are as large or larger than the $E2$ contribution which is shown for comparison as the series of solid circles. However, the phase of the $l\geqslant 2$ multipoles is nearly zero so that their imaginary parts are always very small (Fig. 45 and Fig. 46) and the contributions of these imaginary parts to $\hat{\Sigma}(\pi^0)$ are essentially negligible. On the other hand, their real parts are significant. But these enter $\hat{\Sigma}(\pi^0)$ as products with the resonant M_{1+} whose real part crosses zero at the resonance energy. This forces all $[l\geqslant 2]\times[M_{1+}]$ products to zero at this point, even if the $l\geqslant 2$ strength is significant. As a result, the $\hat{\Sigma}(\pi^0)/\sin^2\theta$ test for $l\geqslant 2$ partial waves is not applicable for energies close to the resonance. But this is not really a serious limitation since by continuity, if there are *D* waves below the resonance, then there must be $l\geqslant 2$ strength under the Δ as well.

An analysis of the problems inherent to multipole expansions has shown that the highest fitted partial wave tends to accumulate uncertainties and is essentially guaranteed to be the least well determined [107], which is itself another good reason for carrying the fit beyond *P* waves. Since the $\hat{\Sigma}(\pi^0)/\sin^2\theta$ test shows that there is an underlying process requiring *D* waves, we have extended the fits of Table X up to *F* waves so as to make sure the fits to *D* wave multipoles are meaningful. Indeed, examination of the $f3$ multipoles of Fig. 45 and Fig. 46 show large uncertainties in many of the *F* waves but quite reasonable determinations of the *D* wave terms.

2. Overcoming Donnachie's ambiguity with polarization data

Donnachie's ambiguity of higher partial-wave strength appearing in lower partial waves, and vice versa, can be effectively mitigated by constraining the fitted amplitudes with many independent polarization observables. This is illustrated in Table XI which shows the evolution of the extracted EMR to its final value [57]. The number of partial waves with fitted non-Born contributions increases to the right in the columns while the number of observables is increased in successive rows. If only the LEGS (γ,π) cross sections and beam asymmetries from Tables IV–VII are used as constraints (row 1), the result is unstable and strongly depends on the number of partial waves included in the fit. But as soon as additional (γ,π) polarization observables are added (row 2), the extracted EMR value stabilizes. As expected from Fig. 57, the further addition of Compton observables has only small effects (row 3).

We have also tracked the evolution of a multipole solution starting with the Mainz (γ,π) cross sections and beam

TABLE XI. Evolution of the $N\rightarrow\Delta$ EMR, starting with fits to the (γ,π) cross sections and beam asymmetries from LEGS (present work), and expanding the data base (Table IX) in subsequent rows by adding data on other observables as indicated. The number of partial waves with fitted non-Born components is increased in successive columns to the right.

Data included in successive analyses	EMR (%) fit $l_\pi=S-P$	EMR (%) fit $l_\pi=S-D$	EMR (%) fit $l_\pi=S-F$
(γ,π): LEGS (Tables IV–VII) $\{\sigma,\Sigma\}$	$-(2.16\pm0.43)$	$-(4.22\pm1.08)$	$-(4.03\pm1.34)$
(γ,π): + Bonn '96 $\{T\}$ + Kharkov '81-86 $\{T,P,G,H\}$	$-(2.61\pm0.29)$	$-(2.74\pm0.28)$	$-(2.82\pm0.29)$
$(\gamma,\pi)+(\gamma,\gamma)$: + LEGS (Tables II, III) $\{\sigma,\Sigma\}$ + world data $\{\sigma\}$	$-(2.77\pm0.29)$	$-(2.90\pm0.28)$	$-(3.07\pm0.26)$

asymmetries from [43]. This is shown in Table 2 of Ref. [57]. When only the Mainz σ and Σ observables are fitted, the resulting EMR again varies with the number of fitted partial waves. But when additional polarization observables are included in the fit, the EMR value stabilizes to $-(2.7\pm0.2)\%$. This overlaps with the values in the third row of Table XI, so it appears that the final $N\rightarrow\Delta$ EMR is largely independent of the (γ,π) cross section scale, even though the individual transition amplitudes are affected by scale variations.

B. Final $N\rightarrow\Delta$ results and uncertainties

We have studied the variations in the extracted $N\rightarrow\Delta$ properties that result from changing assumptions used in our multipole analyses, and these are summarized in Table XII. In row one we investigate the sensitivity to different πN analyses by replacing the unitarization factors $(1+iT^l_{\pi N})$ and $\beta T^l_{\pi N}$ in Eq. (12) by $\cos(\delta_l)e^{i\delta_l}$ and $\beta\sin(\delta_l)e^{i\delta_l}$, respectively, and using the Höhler phase from [108]. Row two gives the result of truncating the multipole expansion at D waves, calculated from rows two and three in Table XI. [We do not consider fits truncated at P waves since these are ruled out by the $\hat{\Sigma}(\pi^0)/\sin^2\theta$ test.] In row three we show the effect of shifting the energies of the LEGS data (Sec. II) to allow for possible differences in calibration between the present measurement and the πN scattering experiments which are used to fix the phases of the photoproduction amplitudes. In row four we show the result of varying by $\pm25\%$ the $\geqslant2\pi$ contributions to the dispersion integrals of Eq. (13). Finally, we have varied the parameters used in Eqs. (14), (15), and (16) to model the asymptotic parts of the Compton amplitudes. These have a very small effect, row five, principally because they enter only the real part of the Compton amplitude which, as seen for example in Fig. 48, crosses zero near the resonance energy where the $N\rightarrow\Delta$ transitions dominate (Fig. 54). These *model-dependent* uncertainties are added in quadrature and listed in the last row of Table XII.

In summary, our final results for the EMR and the $N\rightarrow\Delta$ transverse helicity amplitudes are expressed with two sets of uncertainties, the first being the combined *statistical* and *systematic* experimental uncertainties from the multipole fit and the second being the *model-dependent* uncertainties from Table XII:

$$EMR=-3.07\pm0.26\pm0.24(\%),$$

$$A_{1/2}=-135.74\pm1.34\pm3.71(10^{-3}\ \mathrm{GeV}^{-1/2}),$$

$$A_{3/2}=-266.90\pm1.62\pm7.81(10^{-3}\ \mathrm{GeV}^{-1/2}). \quad (26)$$

These can be compared to the latest Particle Data Group averages [109] of $EMR(PDG)=-2.5\pm0.5(\%)$, $A_{1/2}(PDG)=-135\pm6(10^{-3}\ \mathrm{GeV}^{-1/2})$ and $A_{3/2}(PDG)=-255\pm8(10^{-3}\ \mathrm{GeV}^{-1/2})$, which include our EMR result from [21] in their averaging procedure. Although these

TABLE XII. Model uncertainties in $N\rightarrow\Delta$ transition properties.

Model assumption	EMR (%)	$A_{1/2}$ $(10^{-3}\ \mathrm{GeV}^{-1/2})$	$A_{3/2}$ $(10^{-3}\ \mathrm{GeV}^{-1/2})$
πN phase solution	±0.10	±2.47	±3.66
variations in l_{max}	±0.08	±0.45	±0.38
E_γ-to-E_π uncertainty	±0.20	±2.72	±6.89
2π component in Compton $\mathrm{Re}\,A_i$	±0.02	±0.13	±0.06
variations in Compton A_i^{as}		±0.11	±0.10
quadrature sum	±0.24	±3.71	±7.81

clearly overlap with our values, we believe the errors in Eq. (26) are a more meaningful representation of uncertainties.

Most theoretical treatments of π-production and nucleon structure guarantee Watson's connection of the (γ,π) and (π,π) channels with a unitarization procedure that is similar, if not identical, to the *K-matrix* prescription of Eq. (12). Predictions of these models can be directly compared to the results in Eq. (26). There are nonetheless other ways of unitarizing the (γ,π) amplitude, such as the *Olsson* or *Noelle* methods described in [16]. We have not investigated these in detail. However, we note that while fits of the model parameters of [16] to our polarization data result in EMR values that vary with unitarization by only $\pm 0.1\%$ [20], the corresponding variations in the helicity amplitudes can be considerably larger ($\pm 15\%$). (*Olsson* unitarization generally leads to smaller $A_{1/2}$ and $A_{3/2}$ values, while the *Noelle* method produces larger values.) Clearly a model's unitarization procedure must be considered when comparing predictions for the helicity amplitudes with the results of Eq. (26).

C. Quadrupole moments and deformation

The helicity amplitudes of Eq. (26) can be related to the $\gamma N\Delta$ vertex couplings and the $N\rightarrow\Delta$ transition moments. Following the convention of Giannini [110], at the $\Delta(1232)$ resonance energy (with a photon energy of $W=0.2588$ GeV in the γN c.m.) the electric coupling is

$$G_{E2}=\frac{M\sqrt{2}}{4\sqrt{\pi\alpha W}}[\sqrt{3}A_{1/2}-A_{3/2}] = +[0.137\pm 0.012\pm 0.043], \quad (27a)$$

and the transition quadrupole moment is

$$Q_{N\rightarrow\Delta}=\frac{-12}{MW\sqrt{6}}G_{E2} = -[0.108\pm 0.009\pm 0.034](\mathrm{fm}^2). \quad (27b)$$

Here, the first uncertainty is again the combined *statistical* and *systematic* uncertainty and the second reflects the propagation of *model* uncertainties. Similarly, the magnetic coupling is

$$G_{M1}=\frac{-3M\sqrt{2}}{4\sqrt{\pi\alpha W}}\left[\frac{1}{\sqrt{3}}A_{1/2}+A_{3/2}\right] = +[4.460\pm 0.023\pm 0.104], \quad (27c)$$

and the transition dipole moment is

$$\mu_{N\rightarrow\Delta}=\frac{2}{\sqrt{6}}G_{M1} = +[3.642\pm 0.019\pm 0.085]. \quad (27d)$$

There is a striking difference between these values and those of constituent quark models (CQM) which predict a very small $E2$ component, with $Q_{N\rightarrow\Delta}=+0.003\pm 0.001$ fm^2 and EMR $=+(0.12\pm 0.02)\%$ [111,11]. This has been understood in the framework of the dynamical meson-exchange model of Sato and Lee [12] who have fitted the parameters of their calculation to our data and found for the *bare* $\gamma N\Delta$ vertex, $Q_{N\rightarrow\Delta}=+0.001\pm 0.027$ fm^2 and $EMR=+(0.0\pm 1.3)\%$, while for the $\gamma N\Delta$ vertex *dressed* with pion loops, $Q_{N\rightarrow\Delta}=-0.051\pm 0.029$ fm^2 and EMR $=-(1.8\pm 0.9)\%$. The CQM lacks the physics of the pion cloud and is most appropriately compared to the *bare* vertex results. Evidently, the *spectroscopic* $Q_{N\rightarrow\Delta}$ is almost entirely a product of the nucleon's pion cloud. [Wilhelm, Wilbois and Arenhoevel [112] have pointed out a potential ambiguity that can occur in models that treat the πN decay channel dynamically in such a way that unitarity is automatically built in, as in the calculations of Sato and Lee. Such ambiguities do not arise when unitarity is imposed with a *K*-matrix-like procedure [112], such as we have adopted in Eq. (12). To demonstrate the consistency of their treatment, Sato and Lee have also shown how *K*-matrix unitarization can be rigorously derived from their dynamical model [12]. Evidently, the ambiguities suggested in [112] do not alter the conclusions above.]

Other baryon models that incorporate the physics of a pion cloud also compare favorably with our extracted $E2$ strength. The Skyrme model of Wirzba and Weise gives $Q_{N\rightarrow\Delta}=-0.121$ fm^2 [10], while Buchmann and collaborators augment the CQM with pion and gluon two-body exchange currents and find $Q_{N\rightarrow\Delta}=-0.097$ fm^2 [13,113].

In the work of Buchmann and collaborators the quadrupole moment of the Δ^+ is just $\sqrt{2}$ larger than the $N\rightarrow\Delta$ transition moment, $Q(\Delta^+)/Q_{N\rightarrow\Delta}=\sqrt{2}$ [13]. Dillon and Morpurgo have recently investigated possible higher order corrections allowed by QCD [114]. Using their general QCD parametrization for the quadrupole operator, evaluated with SU(4) spin-isospin wave functions [115], this relation becomes $Q(\Delta^+)/Q_{N\rightarrow\Delta}=\sqrt{2}(1+\frac{1}{2}C/B)/(1-C/B)$, where Dillon and Morpurgo have estimated $|C/B|$ at about 1/3. Unfortunately, the sign of C/B is at present unknown. Combining this relation with Eq. (27b), we infer the quadrupole moment of the Δ^+ as $Q(\Delta^+)=-[0.182\pm 0.015\pm 0.057\pm 0.086]$ fm^2, where the third uncertainty reflects the sign ambiguity in C/B. Combining the *model* uncertainty from our analysis with this QCD sign ambiguity gives a *net model* uncertainty of ± 0.103, so that

$$Q(\Delta^+)=-[0.182\pm 0.015\pm 0.103]\ \mathrm{fm}^2. \quad (27e)$$

This is the *spectroscopic* or *static* quadrupole moment (as measured in the lab frame) and the negative sign here indicates an oblate deformation for the Δ^+. For any spin system the *static* quadrupole moment is proportional to $j(2j-1)$ from Clebsch-Gordan coefficients, and as a result $Q(N)$ must vanish for the $j=1/2$ nucleon.

However, the quantities of greater theoretical interest are not the observed static moments but the moments of the *intrinsic* body-fixed system. Buchmann and Henley [116] have recently investigated the relation between the *intrinsic* and *static* moments in three different nucleon models: a quark model, a collective model and a pion cloud model. All

three lead to the same result, an intrinsic Δ^+ quadrupole moment with the same sign as $Q(\Delta^+)$ and an intrinsic proton quadrupole moment of the *opposite* sign. This is easiest to visualize in the collective model with the proton as a prolate spheroid in its body-fixed frame which, when excited by rotating perpendicular to its symmetry axis, becomes oblate. It is particularly intriguing that all three models give consistent signs for the proton and Δ^+ intrinsic quadrupole moments.

IX. PROTON POLARIZABILITIES

The transient dipole moments of the proton, induced by the electric and magnetic fields of the photon during scattering, can be expressed in the laboratory as [2,5]

$$\vec{D} = \overline{\alpha}\vec{E} + \tfrac{1}{2}\{\overline{\alpha}_1 \nabla(\vec{\sigma}\cdot\vec{B}) + \overline{\alpha}_2 \vec{\sigma}\times(\nabla\times\vec{B})\},$$

$$\vec{M} = \overline{\beta}\vec{B} + \tfrac{1}{2}\{\overline{\beta}_1 \nabla(\vec{\sigma}\cdot\vec{E}) + \overline{\beta}_2 \vec{\sigma}\times(\nabla\times\vec{E})\}. \quad (28)$$

The coefficients $\overline{\alpha}$ and $\overline{\beta}$ describe the dynamical rearrangements of charges and magnetic moments within the proton during scattering. They arise from purely dipole scattering and are traditionally referred to as the *dipole polarizabilities*. The other four coefficients $(\overline{\alpha}_1, \overline{\alpha}_2)$ and $(\overline{\beta}_1, \overline{\beta}_2)$ scale terms containing the proton spin $\vec{\sigma}$ and describe the dynamical rearrangement of spins during scattering. They are referred to as the *spin-polarizabilities*, and in terms of their multipole content, they contain contributions from dipole-quadrupole interference. Following the traditional notation, the *bar* over these coefficients indicates that these refer to the structure-dependent *non-Born* parts of the induced dipole moments evaluated in the low-energy limit.

The polarizabilities are determined by the *non-Born* parts of the fitted Compton amplitudes, evaluated in the low-energy limit, $A_i^{nB}(\nu = \{s-u\}/4M \rightarrow 0,\ t \rightarrow 0)$. In this limit the amplitudes are purely real and given by Eq. (13). The dipole polarizabilities are determined from

$$\overline{\alpha} - \overline{\beta} = -\frac{1}{2\pi}[A_1^{int}(0,0) + A_1^{as}(0)], \quad (29a)$$

$$\overline{\alpha} + \overline{\beta} = -\frac{1}{2\pi}[A_3^{int}(0,0) + A_6^{int}(0,0) + A_6^{as}(0)], \quad (29b)$$

where A_i^{int} refers to the integral parts of Eq. (13), which are determined by the fitted pion multipoles (Sec. VII B), and the asymptotic parts A_1^{as} and A_6^{as} are determined by the fitted parameters in Eqs. (15b) and (14), respectively. While A_6^{as} is small compared to the integral parts in Eq. (29b), Fig. 47, A_1^{as} is the dominant factor in Eq. (29a). For this reason it is best to constrain the parametrization of its t-dependence with fits to data over as wide a dynamic range as possible before taking the low-energy limit to obtain the polarizabilities.

The spin-polarizabilities were first introduced by Ragusa [2] who presented calculations for the four spin-dependent quantities $(\gamma_1, \gamma_2, \gamma_3, \gamma_4)$ in the Breit frame. There are now at least three other conventions in use, that of Babusci *et al.* [5] who work in the lab frame and introduced the parameters $(\overline{\alpha}_1, \overline{\beta}_1, \overline{\alpha}_2, \overline{\beta}_2)$ appearing in Eq. (28) above, that of Drechsel *et al.* [117] who work in the c.m. and used the combination of spin-polarizabilities denoted by $(\gamma_\pi, \gamma_0, \gamma_{13}, \gamma_{14})$, and that of L'vov and co-workers [118] who use the set $(\gamma_{E1}, \gamma_{M1}, \gamma_{E2}, \gamma_{M2})$ to emphasize their multipole content. The relation between these different definitions of the spin-polarizabilities is as follows:

$$\begin{aligned}
\overline{\alpha}_1 &= 4\gamma_3 = -\gamma_0 - \gamma_\pi + 2\gamma_{13} = 4\gamma_{M2}, \\
\overline{\beta}_1 &= -4(\gamma_2 + \gamma_4) = 3\gamma_0 - \gamma_\pi - 2\gamma_{14} = -4\gamma_{E2}, \\
\overline{\alpha}_2 &= 2\gamma_1 = \gamma_0 + \gamma_\pi = -2(\gamma_{E1} + \gamma_{M2}), \\
\overline{\beta}_2 &= 2(\gamma_2 + 2\gamma_4) = -\gamma_0 + \gamma_\pi = 2(\gamma_{M1} + \gamma_{E2}).
\end{aligned} \quad (30)$$

We refer to the parameters γ_0 and γ_π as the *forward* and *backward* spin-polarizabilities, respectively, taking these names from the angular regions which are most sensitive to them in Compton scattering [9]. From Eq. (30) it is obvious that $\gamma_\pi = \frac{1}{2}(\overline{\alpha}_2 + \overline{\beta}_2)$. Babusci *et al.* [5] had first introduced this combination as $\delta = -\frac{1}{2}(\overline{\alpha}_2 + \overline{\beta}_2)$, which we had used in [9]. This definition differs only by a minus sign, $\delta = -\gamma_\pi$. In this work we shall use γ_π for the backward spin polarizability since that seems to be more common lately. As evident in Fig. 47, only the A_2 helicity amplitude is poorly convergent. The c.m. set of polarizabilities $(\gamma_\pi, \gamma_0, \gamma_{13}, \gamma_{14})$ has the advantage of restricting the contributions of the A_2 amplitude to only γ_π, which then reduces the uncertainties in the other three. This combination of spin polarizabilities is determined by

$$\gamma_\pi = -\frac{1}{2\pi M}[A_5^{int}(0,0) + A_2^{int}(0,0) + A_2^{as}(0)], \quad (31a)$$

$$\gamma_0 = +\frac{1}{2\pi M}[A_4^{int}(0,0)], \quad (31b)$$

$$\gamma_{13} = -\frac{1}{4\pi M}[A_5^{int}(0,0) + A_6^{int}(0,0) + A_6^{as}(0)], \quad (31c)$$

$$\gamma_{14} = +\frac{1}{4\pi M}[2A_4^{int}(0,0) + A_5^{int}(0,0) - A_6^{int}(0,0) - A_6^{as}(0)]. \quad (31d)$$

Here the *integral* parts are determined by the fitted pion multipoles and the *asymptotic* parts by the fitted parameters of Eqs. (14) and (16).

There are three important differences between our analysis of nucleon polarizabilities [9] and those of other authors. In the first place, all other analyses have fixed the pion multipoles used to evaluate the dispersion integrals of Eq. (13) and then varied only the polarizabilities, via variations in the A_i^{as}, to fit Compton data. Instead, we have simultaneously varied the pion multipoles *and* the A_i^{as} to fit both π-production and Compton scattering. This is the only way

to maintain a consistent unitarization of the *S-matrix* and, as seen in Fig. 57, this has important consequences.

A second feature of our analysis is that the sum of the dipole polarizabilities is determined from the fit via Eq. (29b), while other analyses generally impose the Baldin sum rule [119] as a constraint,

$$\overline{\alpha}+\overline{\beta}=\frac{1}{2\pi^2}\int_{\omega_0}^{\infty}\frac{\sigma^{tot}}{\omega^2}d\omega. \tag{32}$$

The total nuclear reaction cross section, σ^{tot}, above threshold (ω_0) can be used to evaluate the right-hand side of Eq. (32) independent of Compton scattering. Since this integral converges fairly rapidly, and reaction cross sections are much larger than those of the Compton process, this should be the best way of fixing the sum of the dipole polarizabilities. However, there are now several distinct evaluations of Eq. (32). The original work of Damashek and Gilman [95] gave $\overline{\alpha}+\overline{\beta}=14.2\pm0.3(10^{-4}\ \mathrm{fm}^3)$ using data from the 1960s. A re-evaluation using fits to a recent and greatly expanded data base gives $\overline{\alpha}+\overline{\beta}=13.69\pm0.14$ [120]. However, another recent re-evaluation gives a result closer to the original value, $\overline{\alpha}+\overline{\beta}=14.0$ [121], although with a rather ill-defined uncertainty that is estimated at $\pm(0.3-0.5)$. Given this spread of values for the right-hand side of Eq. (32) we feel it more appropriate to fit A_6^{as} and determine $\overline{\alpha}+\overline{\beta}$ directly from Eq. (29b). This also provides independent evaluations of the spin polarizabilities γ_{13} and γ_{14} from Eqs. (31c) and (31d) above.

Since the A_4 amplitude is rapidly convergent, Eq. (31b) is free of asymptotic terms. This is essentially the signature of a rapidly convergent dispersion relation first derived by Gell-Mann, Goldberger and Thirring [94], and referred to as the *spin-polarizability* sum rule in [122,97],

$$\gamma_0=\frac{1}{4\pi^2}\int_{\omega_0}^{\infty}\frac{\sigma_{1/2}-\sigma_{3/2}}{\omega^3}d\omega. \tag{33}$$

Here, $\sigma_{3/2}$ and $\sigma_{1/2}$ are the photoabsorption cross sections for parallel and anti-parallel alignment of the photon and proton spins. Although experimental programs to measure these quantities are underway, there are as yet no data available to accurately evaluate the right-hand side of Eq. (33). We therefore let the fit determine the pion multipoles, and hence A_4^{int}, which then fixes γ_0 through Eq. (31b). [A dispersion sum rule has also been derived for γ_π that is similar in form to Eq. (33), except that the contributions to the integral are parity dependent [123]. But once again, the data needed to capitalize on such a constraint are not available.]

Finally, all other analyses have fixed the asymptotic part of the A_2 amplitude to the first term in Eq. (16c). The third and possibly most significant difference in our analysis is the additional degree of freedom gained by including the new A_2^δ term.

TABLE XIII. Values for $\overline{\alpha}-\overline{\beta}$ deduced from different Compton data sets assuming, for columns 3 and 4, that A_2^{as} is restricted to $A_2^{\pi^0}$ in Eq. (16c), or equivalently $\gamma_\pi=-36.6$. The last column shows the results when the A_2^δ term of Eq. (16b) is fitted, corresponding to $\gamma_\pi=-26.5$ [9]. Pion multipole solutions are listed in the top row. For the analyses of individual data sets in the ($\gamma_\pi=-36.6$) columns, cross sections were held at their published values, while in the last column normalization scales were fixed from the fit [9].

(γ,π) multipoles		SM95 [75]	LEGS [21]	fitted
γ_π (10^{-4}fm^4)		-36.6	-36.6	-26.5
$\overline{\alpha}+\overline{\beta}$ (10^{-4} fm^3)		14.2	13.7	13.7
Data set	E_γ^{Max} (MeV)	$\overline{\alpha}-\overline{\beta}$ (10^{-4} fm^3)		
LEGS (Tables II, III)	309	-0.6 ± 0.5	1.7 ± 0.5	9.3 ± 0.7
Mainz '96 [40,41]	309	-1.3 ± 3.4	-4.3 ± 3.0	8.4 ± 4.5
SAL '93 [59]	286	4.4 ± 0.6	3.8 ± 0.6	11.4 ± 0.8
SAL '95 [8]	145	10.3 ± 0.9	10.1 ± 0.9	11.5 ± 1.0
MPI '92 [83]	132	7.3 ± 2.7	6.9 ± 2.7	12.5 ± 3.1
Moscow '75 [84]	110	8.2 ± 2.7	8.5 ± 2.7	11.7 ± 2.8
Ill '91 [85]	70	11.1 ± 4.3	11.1 ± 4.3	12.1 ± 4.3

A. Extractions of $\overline{\alpha}$ and $\overline{\beta}$

A frequently quoted *global average* of low energy experiments for the difference of proton dipole polarizabilities comes from [8],

$$\overline{\alpha}-\overline{\beta}=10.0\pm1.5\pm0.9(10^{-4}\ \mathrm{fm}^3), \tag{34}$$

where the first error is the combined statistical and systematic uncertainty and the second is the model uncertainty. This is based on an analysis of Compton data below 145 MeV from [85,83,8], together with the sum rule constraint, Eq. (32), of $\overline{\alpha}+\overline{\beta}=14.2$ and the assumption that the second and third terms of Eq. (16c) are negligible so that $A_2^{as}=A_2^{\pi^0}$. We have repeated their analysis and found a similar result.

The motivation in [8] for the 145 MeV cut in the data base used in calculating Eq. (34) was to limit the model dependence in the evaluation of the dispersion integrals by keeping below π-production threshold, and with this rational all of the data from [59] were excluded from that analysis. However, when the data from [59], which extend up to 286 MeV, are included the resulting value of $\overline{\alpha}-\overline{\beta}$ drops significantly. As noted in [9], the trend to smaller values of $\overline{\alpha}-\overline{\beta}$ continues with the inclusion of higher energy data, even becoming negative when Compton scattering up to 2π threshold are added from LEGS and Mainz. This is shown in the third and fourth columns of Table XIII where we list the $\overline{\alpha}-\overline{\beta}$ values deduced from different data sets, under the assumption that $A_2^{as}=A_2^{\pi^0}$. As discussed in [9], these variations in $\overline{\alpha}-\overline{\beta}$ do *not* result from model dependent uncertainties in the evaluation of the dispersion integrals of Eq. (13). For energies below the 2π-production threshold ($E_\gamma=309$ MeV lab), unitarity provides an unambiguous connection be-

tween the imaginary parts of the Compton amplitudes, the photopion multipoles, and pion-nucleon phase shifts. As E_γ approaches 309 MeV, near the peak of the Δ, these well-defined single π-production contributions to $\mathrm{Im}A_i$ become very large, while the less certain multipion contributions are quite small below 400 MeV and at higher energies are suppressed by the energy denominator in the integrand of Eq. (13). As a result, there is in fact very little freedom in the computation of the scattering amplitude for energies below 309 MeV. Columns three and four in Table XIII were computed using different photopion multipole solutions and different values for the Baldin sum rule, but row for row the results are nonetheless very close.

The apparent variation in the deduced $\overline{\alpha}-\overline{\beta}$ values of columns three and four in Table XIII is an artifact of an ansatz that limited A_2^{as} to the first term in Eq. (16c). When we fit the additional term of Eq. (16b) we obtain a sizable correction to A_2^{as} [9]. Repeating the calculations with this new value for A_2^{as} gives the results listed in the last column of Table XIII where $\overline{\alpha}-\overline{\beta}$ is now independent of energy. The global results from the $f4$ fit of Table X, which include all of the pion data of Table IX and those Compton data below 309 MeV (i.e., the data of Table XIII), give $\overline{\alpha}-\overline{\beta}=10.39\pm1.77$ (stat+sys) in agreement with the low-energy result of Eq. (34), and $\overline{\alpha}+\overline{\beta}=13.25\pm0.86$ (stat+sys) in agreement with the recent sum-rule evaluation by Babusci *et al.* [120].

B. The backward spin polarizability, γ_π

While the additional freedom from the inclusion of the A_2^δ term of Eq. (16b) has removed the apparent inconsistencies in $\overline{\alpha}-\overline{\beta}$ values extracted from Compton data over π-production threshold, it has also changed the *backward spin-polarizability*, γ_π, considerably. Writing out Eq. (31a) explicitly we find for the $f4$ solution,

$$\begin{aligned}\gamma_\pi &= -\frac{1}{2\pi M}[A_5^{int}(0,0)+A_2^{int}(0,0)\\ &\quad +A_2^{\pi^0}(0)+A_2^{\eta^0}(0)+A_2^{\delta}(0)]\\ &= +4.6+4.1-44.9-0.7+9.7\\ &= -36.9+9.7, \end{aligned} \tag{35}$$

or $\gamma_\pi=-(27.2\pm2.27)10^{-4}$ fm^4. Thus, fitting the additional A_2^δ term results in a non-Born part of γ_π of $(4.6+4.1+9.7)=18.4$, or about twice what had been assumed in previous Compton analyses. The A_2^δ term from the $f3$ solution, which included Compton data up to 350 MeV, is slightly larger and results in $\gamma_\pi=-25.1\pm2.04$, although the values from the two multipole solutions clearly overlap within errors.

Sensitivity to γ_π is chiefly in the large angle Compton data. This is illustrated in Fig. 60 where we plot the predictions from the $f3$ fit (solid lines), and the $f4$ fit (long-dashed lines) which are nearly identical. The results of repeating the calculations with A_2^δ set to zero, $\gamma_\pi=-36.9$, are shown as plus-signs. The effect of the new A_2^δ term is to raise the predicted cross sections at large angles, particularly at the lower energies.

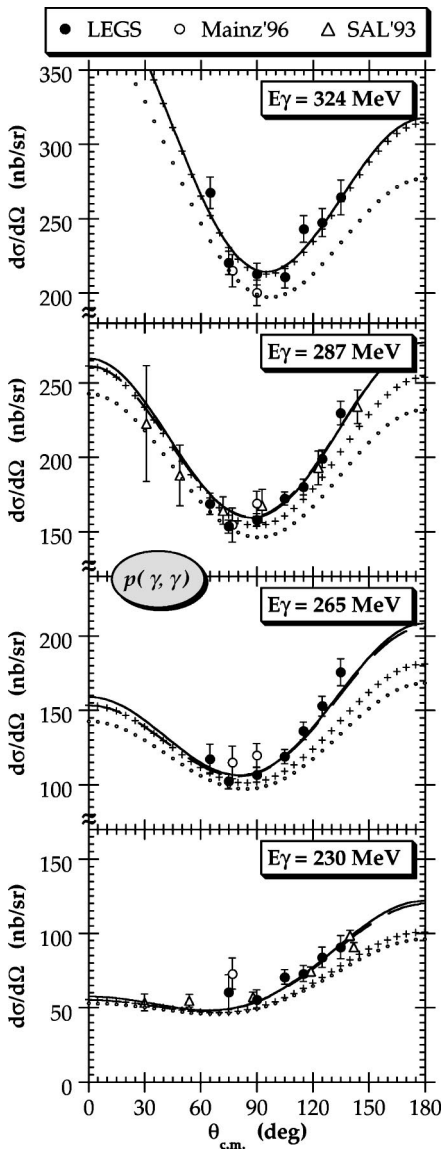

FIG. 60. Angular distributions of c.m. cross sections for $p(\gamma,\gamma)$ from this work (solid circles) and from [40,41,59] (open symbols), compared with predictions from the $f3$ fit (solid lines) and $f4$ fit (long-dashed lines) of Table X. For these comparisons the data have been multiplied by the fitted scale factors (Table IX) from the $f3$ solution (top panel) and $f4$ solution (other panels). For these two fits the resulting backward spin polarizability, γ_π, is -25.1 and -27.2 (in units of 10^{-4} fm^4), respectively. The result of repeating the $f3$ calculation in the top panel and the $f4$ calculations in the other panels with γ_π fixed to -37 is shown as plus-sign $(+++)$ curves. Calculations using the pion multipoles of [22] with γ_π fixed to -37 are indicated by the small-circle curves.

Near the peak of the Δ resonance the real part of the Compton amplitude, which contains all the polarizability dependence, crosses through zero (Fig. 48) so that at 324 MeV (top panel of Fig. 60) there is no sensitivity to γ_π or any of the polarizabilities. As a result, Compton data near the Δ

peak can only introduce noise in the extraction of polarizabilities and so in fixing these quantities for the proton we regard the $f4$ solution as somewhat more reliable.

Since the Compton amplitude is essentially purely imaginary at 324 MeV, these data are completely determined by the pion multipoles. For comparison, we have plotted as the small-circle curves in Fig. 60 calculations of Compton scattering using the *HDT* multipoles of [22]. The lower predicted Compton values at 324 MeV reflect the smaller $p(\gamma,\pi)$ cross sections from Mainz and Bonn that were used to determine this solution. In generating the circle curves we have set $\overline{\alpha}-\overline{\beta}=10.39$ (our $f4$ solution), $\overline{\alpha}+\overline{\beta}=13.69$ as in [120], and $A_2^\delta=0$ so that $\gamma_\pi=-36.9$. As a result, the circle and plus-sign curves are quite close at the lowest energies where the LEGS and Bonn $p(\gamma,\pi)$ data overlap (Fig. 39 and Fig. 41). If one uses the *HDT* multipoles to fit the Compton data below 2π threshold, a larger A_2^δ correction is needed to bring the predictions up to the data, resulting in $\gamma_\pi=-21.4\pm0.9$ [57,58]. Nonetheless, the discrepancies at 324 MeV remain since these are independent of polarizabilities.

There has been a recent speculation [118] of a possible way to fit the Compton data without the introduction of the additional A_2^δ correction, which would keep $\gamma_\pi=-36.9$. The asymptotic part of the A_1 amplitude is assumed to be dominated by t-channel σ-exchange, with σ being the correlated 2π object required in analyses of N-N scattering. Since the σ couplings in the numerator of Eq. (15a) are poorly known, they are simply treated as a free parameter in fitting A_1^{as}. In our fits we have set the σ mass to 600 MeV, an average of several N-N analyses. The authors of [118] have pointed out that reducing m_σ in Eq. (15) changes the t-dependence in such a way as to raise the back angle cross section, so that one might be able to reconcile predictions with data in this way while leaving γ_π fixed at -37. We have investigated this suggestion and found that good fits can indeed be obtained in this way, but with a fitted $m_\sigma=217\pm6$ MeV [57,58] which is substantially less than the mass of two pions. This does not seem a realistic alternative if one is to take seriously the association of A_1^{as} with the t-channel exchange of an S-wave pion pair. But regardless of the physical origins of A_1^{as}, the polarization data do not favor this solution. The spin-difference $\hat{\Sigma}=\frac{1}{2}(d\sigma_\parallel-d\sigma_\perp)$ is completely independent of the A_2 amplitude, and is thus independent of the A_2^δ correction and of γ_π. In Fig. 61 we plot the $f4$ predictions for this observable using the fitted value of $\gamma_\pi=-27.2$ (long-dashed curves), and using $\gamma_\pi=-36.9$ (plus-sign curves). The two predictions coincide. However, $\hat{\Sigma}$ does depend on A_1 and hence on the choice of m_σ in Eq. (15). The dotted curves show the result of fixing $m_\sigma=217$ MeV. Although the uncertainties in the data are far from negligible, the polarization data clearly favor a larger m_σ. (The $f4$ solution with $m_\sigma=600$ MeV has a $\chi^2/\hat{\Sigma}$-point of 1.25, while lowering m_σ to 217 MeV raises the $\chi^2/\hat{\Sigma}$-point to 1.45.)

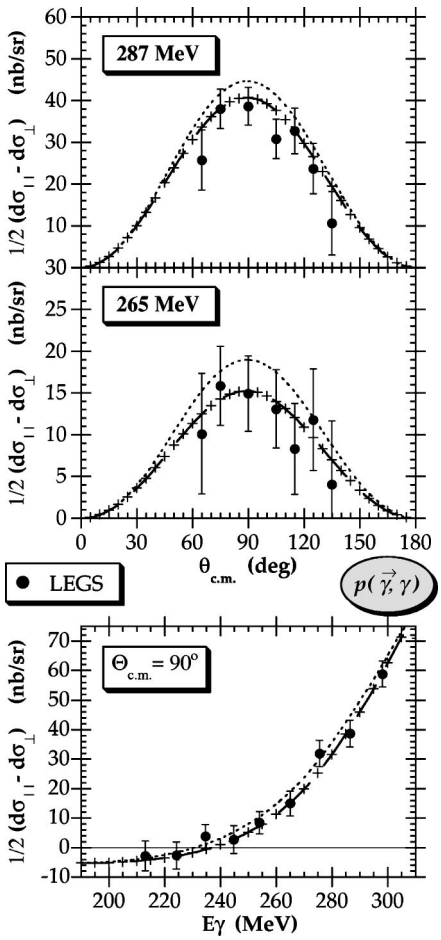

FIG. 61. Compton data from the present work for the spin difference, $\hat{\Sigma}=\frac{1}{2}(d\sigma_\parallel-d\sigma_\perp)$. The long-dashed curves are predictions from the $f4$ solution of Table X with $\gamma_\pi=-27.2$ (10^{-4} fm^4) and $m_\sigma=600$ MeV. The plus-sign curves are obtained by repeating the calculations using the $f4$ multipoles but with γ_π fixed to -37 and $m_\sigma=600$ MeV, while setting $\gamma_\pi=-37$ and $m_\sigma=217$ MeV gives the dotted curves.

C. The spin polarizabilities, γ_0, γ_{13}, γ_{14}

The *forward spin polarizability*, γ_0, is entirely determined by the fitted pion multipoles entering the A_4^{int} integral term of the Compton amplitude in Eq. (31b). Evaluating this with the $f3$ and $f4$ multipole solutions (Table X) gives $\gamma_0=-1.46\pm0.15$ and -1.55 ± 0.15 (10^{-4} fm^4), respectively. The two results are quite close in value since none of the fitted asymptotic terms enter the evaluation of γ_0.

The γ_{13} and γ_{14} polarizabilities of Eqs. (31c) and (31d) are determined by integral terms and the *asymptotic* part of the A_6 amplitude. Because the latter is so small (Fig. 47), the $f3$ and $f4$ solutions again yield very similar results: $\gamma_{13}=4.15\pm0.55$ and 3.94 ± 0.53 (10^{-4} fm^4) from $f3$ and $f4$, and $\gamma_{14}=-1.88\pm0.25$ and -2.20 ± 0.27 (10^{-4} fm^4) from $f3$ and $f4$, respectively. As discussed in the previous section, we regard the $f4$ evaluation of A_6^{as} as the more reliable.

D. Final proton polarizabilities and uncertainties

We have studied the variations in the extracted polarizabilities that result from changing assumptions used in our analysis, and these are summarized in Table XIV. The results in rows one through four were obtained with the same pro-

TABLE XIV. Model uncertainties in the extraction of proton polarizabilites; see Sec. IX D. (Entries less than 0.01 have been left blank.)

Model assumption	$\overline{\alpha}-\overline{\beta}$ (10^{-4} fm^3)	$\overline{\alpha}+\overline{\beta}$ (10^{-4} fm^3)	γ_π (10^{-4} fm^4)	γ_0 (10^{-4} fm^4)	γ_{13} (10^{-4} fm^4)	γ_{14} (10^{-4} fm^4)
πN phase solution	± 0.26		± 0.40			
variations in l_{max}	± 0.24	± 0.08	± 0.32	± 0.02	± 0.04	± 0.02
E_γ -to- E_π variation	$+0.05/-0.62$	$+0.10/-0.00$	$+0.09/-0.33$	$+0.00/-0.01$	$+0.12/-0.04$	$+0.02/-0.04$
(γ, multi-π) in A_i^{int}	± 0.26	± 0.13	± 0.21	± 0.02	± 0.16	± 0.03
B_p	± 0.02	$+0.01/-0.04$	± 0.02		$+0.00/-0.01$	
B_δ	$+0.26/-1.59$	$+0.08/-0.52$	$+0.00/-0.75$	$+0.00/-0.01$	$+0.01/-0.06$	$+0.01/-0.06$
m_σ	$+0.87/-0.62$	$+0.04/-0.16$	$+0.19/-0.42$		$+0.00/-0.01$	$+0.01/-0.02$
$g_{\pi NN}F_{\pi^0\gamma\gamma}$	$+0.05/-0.04$	$+0.09/-0.13$	± 1.54	± 0.01		$+0.02/-0.03$
Λ_π	$+0.04/-0.00$	$+0.05/-0.02$	$+1.18/-0.00$			$+0.01/-0.00$
$A_2^\delta(t)$ form	± 0.08		± 0.95		± 0.01	± 0.01
quadrature sum	$+1.02/-1.87$	$+0.23/-0.58$	$+2.24/-2.10$	$+0.03/-0.03$	$+0.20/-0.18$	$+0.05/-0.09$

cedures used to generate the first four rows of Table XII. (See Sec. VIII B.) In row one we show the effects of replacing the GW-SAID πN T-matrix elements in Eq. (12) with the Höhler phase-shifts from [108]. Row two gives the result of truncating the (γ,π) multipole expansion at D waves, and in row three we show the effect of shifting the energies of the LEGS data to allow for possible differences in calibration with the πN scattering experiments (Sec. II). In row four we show the result of varying by $\pm 25\%$ the contributions from multiple-pion production in the dispersion integrals of Eq. (13). The effects of varying the Regge slope parameters B_p of Eq. (14) and B_δ of Eq. (16b) in the range 4 GeV $\leqslant B \leqslant$ 10 GeV [24] are shown in rows five and six. There is an appreciable correlation in the fits between the A_1^{as} and A_2^{as} amplitudes, and as a result variations in B_δ give significant contributions to the uncertainty in $\overline{\alpha}-\overline{\beta}$. (This is the main source of the increase in the model-dependent uncertainty from [9].) In row seven we vary the σ-mass parameter of Eq. (15) in the range $500 \leqslant m_\sigma \leqslant 700$ MeV. The mass of the σ is model dependent. A recent analysis puts m_σ between 535 MeV and 650 MeV [124], and we have about doubled this range for our uncertainty estimate. (The *PDG* average including many old analyses gives a much larger range, $400 \leqslant m_\sigma \leqslant 1200$ MeV [103]. If m_σ is allowed to vary through that range, the main effects are to increase the row seven uncertainties in $\overline{\alpha}-\overline{\beta}$ to ± 2.05 and in γ_π to $+0.20/-1.43$.) The π^0-exchange coupling, $g_{\pi NN}F_{\pi^0\gamma\gamma} = -(0.331 \pm 0.012)$ GeV^{-1} [55], is varied through the range of its uncertainties in row eight, and in row nine we vary the cutoff mass Λ_π in the form factor of Eq. (16a) by ± 0.3 GeV. Finally, in row ten we investigate the effect of replacing the Regge parametrization for A_2^δ in Eq. (16b) with the functional form of Eq. (15b), corresponding to a t-channel exchange of a particle with a mass of 1 GeV. These *model-dependent* uncertainties are added in quadrature and listed in the last row of Table XIV.

In summary, our final results for the dipole and spin-polarizabilities of the proton are expressed with two sets of uncertainties, the first being the combined *statistical* and *systematic* experimental uncertainties from the simultaneous multipole fit and the second being the *model-dependent* uncertainties from Table XIV:

$$\begin{aligned}
\overline{\alpha}-\overline{\beta} &= +10.39 \pm 1.77^{+1.02}_{-1.87} (10^{-4}\ \text{fm}^3),\\
\overline{\alpha}+\overline{\beta} &= +13.25 \pm 0.86^{+0.23}_{-0.58} (10^{-4}\ \text{fm}^3),\\
\gamma_\pi &= -27.23 \pm 2.27^{+2.24}_{-2.10} (10^{-4}\ \text{fm}^4),\\
\gamma_0 &= -1.55 \pm 0.15^{+0.03}_{-0.03} (10^{-4}\ \text{fm}^4),\\
\gamma_{13} &= +3.94 \pm 0.53^{+0.20}_{-0.18} (10^{-4}\ \text{fm}^4),\\
\gamma_{14} &= -2.20 \pm 0.27^{+0.05}_{-0.09} (10^{-4}\ \text{fm}^4).
\end{aligned} \tag{36}$$

E. Comparisons with χPT

The proton polarizabilities of Eq. (36) can be compared to the expectations of QCD through chiral perturbation theory. The $O(p^4)$ predictions, $\overline{\alpha}-\overline{\beta} = 7.0 \pm 4.1$ and $\overline{\alpha}+\overline{\beta} = 14.0 \pm 4.1 (10^{-4}$ fm$^3)$, have been in reasonable agreement with experiment for several years [3], and predictions for the spin polarizabilities are now being pursued by several groups. When comparing with χPT, the t-channel π^0 and η^0 contributions should be removed from Eq. (35) since these appear at the tree level in χPT and are not normally included in the calculated spin polarizabilities. For this purpose we can define

$$\overline{\gamma_\pi} = -\frac{1}{2\pi M}[A_5^{int}(0,0) + A_2^{int}(0,0) + A_2^\delta(0)], \tag{37a}$$

which for the $f4$ solution is

$$\overline{\gamma_\pi} = +18.40 \pm 2.27^{+2.24}_{-2.10} (10^{-4}\ \text{fm}^4). \tag{37b}$$

In terms of the definitions of Ragusa [2] our $f4$ results (in units of 10^{-4} fm^4) are

TABLE XV. Predictions for the proton spin polarizabilities, in units of 10^{-4} fm^4, from HBχPT [7] and from the subtracted dispersion relations of [117], compared with the results from this work in the last column.

	HBχPT		Subt. Disp. Rel.	This analysis
	$O(p^3)$	$O(p^3)+O(p^4)$	HDT(π)+multi-π	
$\overline{\gamma_\pi}$	+4.6	+3.4	+9.5	$+18.40\pm2.27^{+2.24}_{-2.10}$
γ_0	+4.6	−1.0	−0.8	$-1.55\pm0.15^{+0.03}_{-0.03}$
γ_{13}	+6.8	+2.6	+4.3	$+3.94\pm0.53^{+0.20}_{-0.18}$
γ_{14}	+6.8	+0.4	−1.5	$-2.20\pm0.27^{+0.05}_{-0.09}$

$$\begin{aligned}
\overline{\gamma_1} &= \tfrac{1}{2}(\gamma_0+\overline{\gamma_\pi}) \\
&= +8.43\pm1.14^{+1.12}_{-1.05}, \\
\gamma_2 &= -\gamma_0+\gamma_{14} \\
&= -0.65\pm0.31^{+0.06}_{-0.09}, \\
\overline{\gamma_3} &= -\tfrac{1}{4}(\gamma_0+\overline{\gamma_\pi}-2\gamma_{13}) \\
&= -2.24\pm0.63^{+0.57}_{-0.53}, \\
\overline{\gamma_4} &= +\tfrac{1}{4}(\gamma_0+\overline{\gamma_\pi}-2\gamma_{14}) \\
&= +5.31\pm0.58^{+0.56}_{-0.53}
\end{aligned} \tag{38}$$

where the *bar* over the symbols again indicates that the *t*-channel π^0 and η^0 terms have been excluded. Compared with Eq. (36), the larger fractional errors in the Ragusa polarizabilities reflect the uncertainty in the poorly convergent A_2 amplitude which contributes to all but γ_2, which is itself small because of a near cancellation.

Our extracted spin polarizabilities are compared with a recent heavy baryon chiral calculation (HBχPT) from [7] in Table XV. The difference between the second and third columns clearly shows that the $O(p^4)$ terms are significant, indicating that the chiral expansion has not yet converged. In fact, large Δ contributions are expected to contribute at $O(p^5)$, particularly in $\overline{\gamma_\pi}$ and γ_0 [7], and such calculations are being pursued.

In the fourth column of Table XV we list the predictions of [117] using once-subtracted dispersion relations to calculate Compton scattering, in contrast to the subtraction-free L'vov relations used in the present work. Their predictions are similar to our results, particularly for γ_0, γ_{13}, and γ_{14}. While they have also confirmed that the data favor a larger value for the backward spin polarizability (less negative for γ_π and more positive for $\overline{\gamma_\pi}$), their result differs from ours because of their use of the *HDT* pion multipoles from [22] which lead to underpredictions of the Compton cross sections, similar to the circle curves in Fig. 60.

X. SUMMARY

The present experiment has achieved an as yet unequaled separation of proton Compton scattering from the very large competing process of π^0 photoproduction in the region of the P_{33} Δ resonance. As seen in Fig. 8 and Fig. 9, the valley between events from the two channels drops to nearly zero for all detector settings and energies. This has been achieved with a large over-determination of kinematic parameters, and is crucial to reducing the uncertainties in the subtraction of the tail of the π^0 component. (The shape of the latter is always difficult to determine accurately at levels that are comparable to Compton scattering.)

In addition to providing definitive Compton/π^0 separation, the large kinematic over-determination in this experiment has allowed us to *measure* the detector efficiencies directly from the data itself (Fig. 11, Fig. 13, and Fig. 15, Sec. IV B), and so remove much of the dependence upon Monte Carlo simulations that have characterized other experiments. This has greatly constrained the resulting cross sections and has led to the small systematic scale uncertainty of 2% (Sec. VI A).

As shown in Fig. 37 and Fig. 38, the Compton cross sections from this experiment are in excellent agreement with published data from SAL [59] and from Mainz [40–42], and are about 28% higher than older Compton data from Bonn [32] near the peak of the Δ resonance. However, while our $p(\gamma,\pi^0)$ angular distributions exhibit the same shape as data from Mainz [43] and Bonn [38], the cross section scales of the latter are about 10% lower (Fig. 44). This is particularly difficult to reconcile. For example, the 90° Compton and π^0 cross sections shown as solid circles in Fig. 38 and Fig. 40 were measured simultaneously in the same detector, for which all detection efficiencies were directly measured. There is no freedom to adjust the scale of the π^0 results without destroying agreement in the Compton channel.

Our $p(\gamma,\pi^+)$ angular distributions also overlap with recent data from Mainz [43] and Bonn [44] if the latter are scaled up by 10% (Fig. 44). However, the only available $p(\gamma,\pi^+)$ data that extend to extreme forward and backward angles are from [39], and these appear relatively higher when rescaled by 10% to match the central angles. The π^+ data from [39] were measured with untagged bremsstrahlung and we have speculated that their measurements at angles close to the beam could have been contaminated by electrons. Angle integrated $p(\gamma,\pi^+)$ cross sections are quite close to results from Tokyo [63], Sec. VI C. Because of the π^+ differences at extreme angles, our fitted total cross sections are about 6% higher (instead of 10%) compared with results from Bonn and Mainz near the peak of the Δ resonance, Fig. 52.

The Compton data near the peak of the Δ provide a consistency check with pion production. There the real part of

the Compton amplitude (which contains all the dependence upon polarizabilities) crosses through zero (Fig. 48), and as a result Compton scattering is determined completely by pion production. As seen in the top panel of Fig. 60, the LEGS pion multipole solution (solid curve) fits the Compton data at the Δ peak while the *HDT* solution (circle curve) which was fitted to the Mainz $p(\gamma,\pi)$ data is significantly lower.

The beam polarization asymmetries from this experiment have substantially smaller uncertainties than any other data set. They are in agreement with Mainz results [43] for π^0-production but disagree in the π^+ channel near the peak of the Δ resonance (Fig. 40, Fig. 42, and Fig. 56). In contrast to the complex process of coherent bremsstrahlung in a crystal lattice that is used to produce polarized photons in Mainz, LEGS γ rays are produced by the Klein-Nishina scattering of light from free electrons in vacuum, and as such their polarizations are very accurately known. The Compton asymmetries from this experiment are the first to span a wide range of energies and angles in the region of the Δ resonance and are in agreement with the only other published datum from Frascati (Fig. 37).

Combining our data from Tables II–VII with other Compton cross section data and other $p(\gamma,\pi)$ polarization ratios (Table IX), we have carried out the first simultaneous multipole analysis of Compton scattering and photo-pion production. This is the only way to consistently maintain unitarity and has important consequences for several multipoles, particularly the dominant $M_{1+}^{3/2}$ (Fig. 57). While the measured angular distributions can be fitted by varying only $l_{\pi N}=S$ and *P* waves, we have shown that the difference in $p(\gamma,\pi^0)$ polarized cross sections, $\hat{\Sigma}=1/2(d\sigma_{\parallel}-d\sigma_{\perp})$, demands contributions from at least *D* waves (Sec. VIII A 1 and Fig. 58). Since the highest partial wave varied in a multipole analysis is guaranteed to be the most uncertain [107], we have extended our fits to *F*-waves (Fig. 45 and Fig. 46). We have shown that *Donnachie's ambiguity* of higher partial-wave strength appearing in lower partial waves, which can occur when truncating a multipole expansion [26], is effectively mitigated by constraints from many independent polarization observables (Sec. VIII A 2 and Table XI).

The $M_{1+}^{3/2}$ and $E_{1+}^{3/2}$ pion amplitudes, together with their $N \rightarrow \Delta$ resonant components, have been determined to high accuracy by our simultaneous fit, Eq. (26). The new beam polarization data provide the greatest constraints on the $E_{1+}^{3/2}$ multipole (Fig. 56). Although the $M_{1+}^{3/2}$ is quite sensitive to the Compton data, the $E_{1+}^{3/2}$ is not (Fig. 57). As a result, while the Compton data have a significant effect on the $A_{1/2}$ and $A_{3/2}$ transverse helicity amplitudes, their effect on the $E2$ to $M1$ mixing EMR is only minor. The helicity amplitudes determine the $\gamma N\Delta$ vertex couplings and the $N \rightarrow \Delta$ transition moments, Eq. (27). The inferred *spectroscopic* quadrupole moment of the Δ^+ is negative, Eq. (27e), indicating an oblate shape.

We have extracted the two *dipole* and four *spin polarizabilities* of the proton, Eq. (36), determined from the low-energy limits of the fitted Compton helicity amplitudes. The resulting *backward spin polarizability*, γ_π, is significantly different from previous expectations, with a *non-Born* part that is larger by about a factor of 2. This difference is driven by the Compton cross sections at back angles (Fig. 60), and has resulted from *fitting* the asymptotic part of the one poorly-convergent helicity amplitude, A_2 in Fig. 47. (All previous analyses had simply held this contribution constant.) This new fitted A_2 has also removed an apparent energy dependence in the value of $\overline{\alpha}-\overline{\beta}$, the difference of the proton dipole polarizabilities (Table XIII). Our value for $\overline{\alpha}-\overline{\beta}$ extracted from data up to 2π threshold is in agreement with low energy results, while our fitted value for $\overline{\alpha}+\overline{\beta}$ is in agreement with the Baldin sum rule.

Our extracted value for γ_π differs significantly from $O(p^4)$ HBχPT predictions (Table XV), although potentially large corrections are expected at order $O(p^5)$ [7]. While these theoretical efforts are underway, it would be highly desirable to measure other observables with increased sensitivity to γ_π, and two double-polarization $\vec{p}(\vec{\gamma},\gamma)$ experiments are planned at LEGS [57,58]. Such double-polarized Compton experiments are sometimes referred to as providing *direct* access to the spin polarizabilities [125]. However, one must recall that 12 independent observables are needed to determine the Compton amplitude above pion threshold (and 6 below threshold). It is very unlikely that such a complete set of data will ever be available and future extractions will always involve *fits* to an incomplete set of observables. Although still not *direct*, such fits will hopefully have improved sensitivities.

ACKNOWLEDGMENTS

We would like to acknowledge fruitful discussions with Dr. Dick Arndt, Dr. Alfons Buchmann, Dr. Harry Lee, Dr. Nimai Mukhopadhyay, and Dr. Alan Nathan. We thank Dr. Anatoly L'vov and Dr. Shin-nan Yang for making their computer codes available. This work was supported by the U.S. Department of Energy under Contract No. DE-AC02-98CH10886, by the U.S. National Science Foundation, and by the Istituto Nazionale di Fisica Nucleare (Italy).

[1] V. A. Petrun'kin, Sov. J. Part. Nucl. **12**, 278 (1981).
[2] S. Ragusa, Phys. Rev. D **47**, 3757 (1993).
[3] V. Bernard, N. Kaiser, Ulf-G. Meissner, and A. Schmidt, Z. Phys. A **348**, 317 (1994).
[4] V. Bernard, N. Kaiser, and Ulf-G. Meissner, Int. J. Mod. Phys. E **4**, 193 (1995).
[5] D. Babusci, G. Giordano, and G. Matone, Phys. Rev. C **55**, R1645 (1997); D. Babusci (private communication).
[6] T. Hemmert, B. Holstein, J. Kambor, and G. Knöchlein, Phys. Rev. D **57**, 5746 (1998).
[7] G. C. Gellas, T. R. Hemmert, and Ulf-G. Meissner, Phys. Rev. Lett. **85**, 14 (2000).

[8] B. E. MacGibbon *et al.*, Phys. Rev. C **52**, 2097 (1995).
[9] J. Tonnison, A. M. Sandorfi, S. Hoblit, and A. M. Nathan, Phys. Rev. Lett. **80**, 4382 (1998).
[10] A. Wirzba and W. Weise, Phys. Lett. B **188**, 6 (1987).
[11] R. Bijker, F. Iachello, and A. Leviatan, Ann. Phys. (N.Y.) **236**, 69 (1994).
[12] T. Sato and T.-S. H. Lee, Phys. Rev. C **54**, 2660 (1996).
[13] A. J. Buchmann, E. Hernández, and A. Faessler, Phys. Rev. C **55**, 448 (1997).
[14] N. C. Mukhopadhyay, in *Topical Workshop on Excited Baryons 1988*, Troy, New York, edited by G. Adams, N. Mukhopadhyay, and P. Stoler (World Scientific, Singapore, 1989), p. 205.
[15] R. M. Davidson and N. C. Mukhopadhyay, Phys. Rev. D **42**, 20 (1990).
[16] R. M. Davidson, N. C. Mukhopadhyay, and R. Wittman, Phys. Rev. D **43**, 71 (1991).
[17] LEGS Collaboration, G. Blanpied *et al.*, Phys. Rev. Lett. **69**, 1880 (1992).
[18] R. L. Workman, R. A. Arndt, and Z. Li, Phys. Rev. C **46**, 1546 (1992).
[19] R. M. Davidson and N. C. Mukhopadhyay, Phys. Rev. Lett. **70**, 3834 (1993).
[20] M. Khandaker and A. M. Sandorfi, Phys. Rev. D **51**, 3966 (1995).
[21] LEGS Collaboration, G. Blanpied *et al.*, Phys. Rev. Lett. **79**, 4337 (1997).
[22] O. Hanstein, D. Drechsel, and L. Tiator, Nucl. Phys. **A632**, 561 (1998).
[23] K. Watson, Phys. Rev. **95**, 228 (1954).
[24] A. I. L'vov, Sov. J. Nucl. Phys. **34**, 597 (1981).
[25] W. Chiang and F. Tabakin, Phys. Rev. C **55**, 2054 (1997).
[26] A. Donnachie, Rep. Prog. Phys. **36**, 695 (1973).
[27] G. Bernadini *et al.*, Nuovo Cimento **18**, 1203 (1960).
[28] J. W. DeWire *et al.*, Phys. Rev. **124**, 909 (1961).
[29] Y. Nagashima, Inst. Nucl. Study, Tokyo, Report No. INSJ-**81** (1964).
[30] P. S. Baranov *et al.*, Sov. J. Nucl. Phys. **36**, 791 (1966).
[31] E. R. Gray and A. O. Hanson, Phys. Rev. **160**, 1212 (1967).
[32] H. Genzel *et al.*, Z. Phys. A **279**, 399 (1976).
[33] W. Pfeil, H. Rollnik, and S. Stankowski, Nucl. Phys. **B73**, 166 (1974).
[34] I. Guiasu, C. Pomponiu, and E. E. Radescu, Ann. Phys. (N.Y.) **114**, 296 (1978).
[35] I. Caprini, I. Guiasu, and E. E. Radescu, Phys. Rev. D **25**, 1808 (1982).
[36] M. Benmerrouche and N. C. Mukhopadhyay, Phys. Rev. D **46**, 101 (1992).
[37] LEGS Collaboration, G. Blanpied *et al.*, Phys. Rev. Lett. **76**, 1023 (1996).
[38] H. Genzel *et al.*, Z. Phys. **268**, 43 (1974).
[39] G. Fischer *et al.*, Z. Phys. **253**, 38 (1972).
[40] C. Molinari *et al.*, Phys. Lett. B **371**, 181 (1996).
[41] J. Peise *et al.*, Phys. Lett. B **384**, 37 (1996); Jürgen Ahrens (private communication).
[42] F. Wissmann *et al.*, Nucl. Phys. **A660**, 232 (1999).
[43] R. Beck *et al.*, Phys. Rev. Lett. **78**, 606 (1997); H.-P. Krahn, thesis, U. Mainz, 1996; R. Beck (private communication).
[44] K. Büchler *et al.*, Nucl. Phys. **A570**, 580 (1994).
[45] C. E. Thorn, G. Giordano, O. C. Kistner, G. Matone, A. M. Sandorfi, and C. S. Whisnant, Nucl. Instrum. Methods Phys. Res. A **285**, 447 (1989).
[46] D. Babusci, G. Giordano, and G. Matone, Phys. Lett. B **355**, 1 (1995).
[47] LEGS Collaboration, G. Blanpied *et al.*, Phys. Rev. C **52**, R455 (1995).
[48] V. Bellini *et al.*, Nucl. Phys. **A646**, 55 (1999).
[49] Manufactured by Bicron Corp., 12345 Kinsman Rd., Newbury, OH 44065.
[50] Hamamatsu Photonics K.K., 325-6, Sunayama-cho, Hamamatsu City, 430, Japan.
[51] GEANT 3.2.1, CERN Library W5013, CERN (1993).
[52] GCALOR, C. Zeitnitz, and T. A. Gabriel, Nucl. Instrum. Methods Phys. Res. A **349**, 106 (1994).
[53] C. A. Baker *et al.*, Nucl. Instrum. Methods **71**, 117 (1969).
[54] B. Preedom *et al.*, Nucl. Instrum. Methods **133**, 311 (1976).
[55] A. I. L'vov, V. A. Petrun'kin, and M. Schumacher, Phys. Rev. C **55**, 359 (1997).
[56] *Gheisha 6/7*, Z. Jakubowski, and M. Kobel, Nucl. Instrum. Methods Phys. Res. A **297**, 60 (1990).
[57] A. M. Sandorfi, S. Hoblit, and J. Tonnison, Few-Body Syst., Suppl. **11**, 144 (1999).
[58] S. Hoblit and A. M. Sandorfi, Prog. Part. Nucl. Phys. **44**, 149 (2000).
[59] E. L. Hallin *et al.*, Phys. Rev. C **48**, 1497 (1993).
[60] G. Barbiellini *et al.*, Phys. Rev. **174**, 1665 (1968).
[61] P. Dougan *et al.*, Z. Phys. A **276**, 155 (1976); **280**, 341 (1977).
[62] A. Belyaev *et al.*, Nucl. Phys. **B213**, 201 (1983).
[63] T. Fujii *et al.*, Nucl. Phys. **B120**, 395 (1977).
[64] V. A. Get'man *et al.*, Nucl. Phys. **B188**, 397 (1981).
[65] M. J. Moravcsik, Phys. Rev. **104**, 1451 (1956).
[66] H. Genzel, P. Joos, and W. Pfeil, in *Photoproduction of Elementary Particles*, edited by H. Schopper, Landolt-Börnstein, Group 1, Vol. 8 (Springer-Verlag, Berlin, 1973).
[67] The reinterpretation of the extreme angle π^+ data has led to the present conclusions regarding scale differences between the LEGS and Mainz/Bonn data sets, which differs from the point of view expressed in [57].
[68] D. Moricciani *et al.*, Few-Body Syst., Suppl. **9**, 349 (1995).
[69] O. Selke *et al.*, Phys. Lett. B **369**, 207 (1996).
[70] A. Kraus *et al.*, Phys. Lett. B **432**, 45 (1998).
[71] F. Rambo *et al.*, Nucl. Phys. **A660**, 69 (1999).
[72] R. L. Walker, Phys. Rev. **182**, 182 (1969).
[73] G. F. Chew, M. L. Goldberger, F. E. Low, and Y. Nambu, Phys. Rev. **106**, 1345 (1957).
[74] Shin-nan Yang, J. Phys. G **11**, L205 (1985); (private communication).
[75] SAID code, http://gwdac.phys.gwu.edu/; R. Arndt, I. Strakovsky, and R. Workman, Phys. Rev. C **53**, 430 (1996).
[76] R. M. Davidson, N. Mukhopadhyay, M. S. Pierce, R. A. Arndt, I. I. Strakovsky, and R. L. Workman, Phys. Rev. C **59**, 1059 (1999).
[77] R. Arndt, R. L. Workman, Z. Li, and L. D. Roper, Phys. Rev. C **42**, 1853 (1990).
[78] M. Lutz and W. Weise, Nucl. Phys. **A518**, 156 (1990).
[79] T. Feuster and U. Mosel, Phys. Rev. C **58**, 457 (1998).

[80] H. Dutz *et al.*, Nucl. Phys. **A601**, 319 (1996).
[81] A. Bock *et al.*, Phys. Rev. Lett. **81**, 534 (1998); Gisela Anton (private communication).
[82] A. A. Belyaev *et al.*, Sov. J. Nucl. Phys. **40**, 83 (1984); **43**, 947 (1986).
[83] A. Zieger *et al.*, Phys. Lett. **278**, 34 (1992).
[84] P. S. Baranov *et al.*, Sov. J. Nucl. Phys. **21**, 355 (1975); only $\sim 90°$ data are included.
[85] F. J. Federspiel *et al.*, Phys. Rev. Lett. **67**, 1511 (1991).
[86] F. A. Berends and A. Donnachie, Nucl. Phys. **B84**, 342 (1975).
[87] R. L. Crawford, Nucl. Phys. **B97**, 125 (1975).
[88] G. D'Agostini, Nucl. Instrum. Methods Phys. Res. A **346**, 306 (1994).
[89] MINUIT reference manual, CERN Program Library, Long Writeup D506.
[90] Numerical Algorithms Group Ltd., Wilkinson House, Jordon Hill Road, Oxford OX2-8DR, UK.
[91] W. J. Metcalf and R. L. Walker, Nucl. Phys. **B76**, 253 (1974).
[92] I. M. Barbour, R. L. Crawford, and N. H. Pawsons, Nucl. Phys. **B141**, 253 (1978).
[93] J. R. Wolberg, *Prediction Analysis* (Van Nostrand, New York, 1967), pp. 54–66.
[94] M. Gell-Mann, M. L. Goldberger, and W. E. Thirring, Phys. Rev. **95**, 1612 (1954).
[95] M. Damashek and F. J. Gilman, Phys. Rev. D **1**, 1319 (1970).
[96] H. Alvensleben *et al.*, Phys. Rev. Lett. **30**, 328 (1973).
[97] A. M. Sandorfi, C. S. Whisnant, and M. Khandaker, Phys. Rev. D **50**, R6681 (1994).
[98] M. MacCormick Phys. Rev. C **53**, 41 (1996).
[99] T. A. Armstrong *et al.*, Phys. Rev. D **5**, 1640 (1972).
[100] A.M. Sandorfi *et al.*, in *Topical Workshop on Excited Baryons 1988*, Troy, New York, edited by G. Adams, N, Mukhopadhyay, and P. Stoler (World Scientific, Singapore, 1989), p. 256.
[101] A. Hünger *et al.*, Nucl. Phys. **A620**, 385 (1997).
[102] R. Arndt, R. L. Workman, Z. Li, and L. D. Roper, Phys. Rev. C **42**, 1864 (1990).
[103] Particle Data Group, C. Caso *et al.*, Eur. Phys. J. C **3**, 653 (1998).
[104] LEGS Collaboration, G. Blanpied *et al.*, BNL-64382a, 1997, http://www.legs.bnl.gov/
[105] R.L. Workman, in *8th International Conference on the Structure of Baryons 1998*, Bonn, Germany, edited by D.W. Menze and B.Ch. Metsch (World Scientific, Singapore, 1999), p. 717.
[106] R. Beck *et al.*, Phys. Rev. C **61**, 035204 (2000).
[107] J. E. Bowcock and H. Burkhardt, Rep. Prog. Phys. **38**, 1099 (1975).
[108] G. Höhler *et al.*, *Handbook of Pion-Nucleon Scattering*, Phys. Data 12-1 (Fachinformationszentrum, Karlsruhe, 1979).
[109] Particle Data Group, C. Caso *et al.*, Eur. Phys. J. C **3**, 1 (1998).
[110] M. M. Giannini, Rep. Prog. Phys. **54**, 453 (1990).
[111] S. Capstick, Phys. Rev. D **46**, 2864 (1992).
[112] P. Wilhelm, Th. Wilbois, and H. Arenhövel, Phys. Rev. C **54**, 1423 (1996).
[113] A. J. Buchmann, E. Hernández, U. Meyer, and A. Faessler, Phys. Rev. C **58**, 2478 (1998).
[114] G. Dillon and G. Morpurgo, Phys. Lett. B **448**, 107 (1999).
[115] A. J. Buchmann and E. M. Henley (unpublished).
[116] A. J. Buchmann and E. M. Henley, Phys. Rev. C **63**, 015202 (2001).
[117] D. Drechsel, M. Gorchtein, B. Pasquini, and M. Vanderhaeghen, Phys. Rev. C **61**, 015204 (2000).
[118] D. Babusci, G. Giordano, A. L'vov, G. Matone, and A. M. Nathan, Phys. Rev. C **58**, 1013 (1998).
[119] A. M. Baldin, Nucl. Phys. **18**, 310 (1960).
[120] D. Babusci, G. Giordano, and G. Matone, Phys. Rev. C **57**, 291 (1998).
[121] M. I. Levchuk and A. I. L'vov, Nucl. Phys. **A674**, 449 (2000).
[122] V. Bernard, N. Kaiser, J. Kambor, and Ulf-G. Meissner, Nucl. Phys. **B388**, 315 (1992).
[123] A. I. L'vov and A. M. Nathan, Phys. Rev. C **59**, 1064 (1999).
[124] M. Ishida, Prog. Theor. Phys. **96**, 853 (1996). This paper revises the values for m_σ quoted in S. Ishida *et al.*, *ibid.* **95**, 745 (1996).
[125] B. R. Holstein, D. Drechsel, B. Pasquini, and M. Vanderhaeghen, Phys. Rev. C **61**, 034316 (2000).